Bond Behaviour of Deformed Steel Reinforcement in Lightweight Foamed Concrete

by

Johannes Petrus de Villiers

Thesis presented in partial fulfilment of the requirements for the degree of Master of Engineering in Civil Engineering in the Faculty of Engineering at Stellenbosch University

Supervisor:
Prof. Gideon Pieter Adriaan Greeff Van Zijl

Co-supervisor:
Mr. Algurnon Steve van Rooyen

December 2015

Declaration

By submitting this thesis electronically, I declare that the entirety of the work contained therein is my own, original work, that I am the sole author thereof (save to the extent explicitly otherwise stated), that reproduction and publication thereof by Stellenbosch University will not infringe any third party rights and that I have not previously in its entirety or in part submitted it for obtaining any qualification.

Signature: .....

Date: .....

Abstract

Lightweight foamed concrete is a low density concrete that utilizes the entrapment of air generated from a protein based foam mix constituent. It is produced with the base constituents: water, cement and fly-ash, whereafter stable foam is added to change the density.

Lightweight foamed concrete is a relatively new building material with many economic advantages, but it does not reach some of the typical engineering properties of normal weight concrete. The latter is thoroughly researched, characterized and documented in design standards used throughout engineering practice, whereas the paucity of literature on lightweight foamed concrete adds to the slow progress in its development.

Recent progress in mix design and density control of lightweight foamed concrete have led to the notion for its use in structural application i.e. steel reinforced lightweight foamed concrete.

This study characterizes the bond behaviour of deformed steel reinforcement in lightweight foamed concrete, quantifies several of its engineering properties and presents prediction models.

The concretes used for testing were a benchmark normal weight concrete and lightweight foamed concretes with casting densities of 1200, 1400 and 1600 $\mathrm{kg/m^3}$ and they were evaluated for compressive strength, Youngs modulus, indirect tensile splitting strength and wedge splitting fracture energy.

Pull-out and beam-end tests were used to quantify the characteristic bond behaviour. The design of these tests comprises of the loading arrangements, specimen preparation, slip measuring techniques, equipment configuration for accurate slip control and a method for determining a design bond stress correlated to a physical occurrence.

Even though compressive strengths suitable for structural application were achieved for some of the lightweight foamed concretes, its other strength properties and bond behaviour results did not reach the predicted or measured values of normal weight concrete.

Compared to normal weight concrete, the fracture energy of lightweight foamed concrete is at least an order of magnitude smaller. The intrinsic brittleness of lightweight foamed concrete becomes more with increased density and is shown to have a considerable effect on the bond behaviour. The beam-end tests on the 1600 $\mathrm{kg/m^3}$ concrete showed early onset of bond deterioration as a result of internal cracks, intensified by its brittle nature.

Evaluation of the bond-slip envelopes show the denser lightweight foamed concrete performing well when considering bond stress magnitude, but lacking ductility in failure. The least dense lightweight foamed concrete showed excellent ductility during failure, but lacked sufficient bonding stress.

A new concept, named the Bond Integrity (BI), was introduced to quantify early bond disturbances such as internal cracks. It was formulated from the measured rate of change in applied

moment and rate of change in the bar tensile force during the beam-end test.

Prediction models for the design bond stress of lightweight foamed concrete were derived from the stress conditions at the steel-concrete bond interface, taking into consideration two failure modes; pull-out and splitting failure.

The outcome of this study not only quantifies but also emphasizes the lack of sufficient bonding of deformed steel in lightweight foamed concrete. The inadequate crushing strength of the least dense concrete and the brittleness observed for the denser concrete, both diminishes bond integrity and permits significant bond development. It can be concluded that lightweight foamed concrete is not suitable for structural application and that further development of the material is required to increase strength, reduce brittleness and introduce innovative reinforcing systems that will lead to improved bond performance.

Apart from providing standardized and novel results, together with detailed guidelines for the experimental setup and quality control, this study may well become the future basis for further development of lightweight foamed concrete as a structural material.

Uittreksel

Liggewig-skuimbeton is 'n laedigtheid beton wat van lug-gegenereerde, proteïen-basis skuim gebruik maak om lug in die betonmensel vas te vang. Dit word vervaardig uit die samestellende bestanddele: water, sement en vlieg-as, sowel as 'n gekontroleerde byvoeging van skuim om 'n verlangde digtheid te verkry.

Liggewig-skuimbeton is 'n nuwe boumateriaal met baie voordele, maar dit skiet te kort in baie eienskappe wat eie is vir normale-gewig beton en wat geskik is vir strukturele elemente. Laasgenoemde beton is reeds goed gevestig in die ingenieursbedryf en word ondersteun en gestaaf deur omvattende navorsing, eksperimente vir die karakterisering van die materiaal en dokumentasie. Die gebrek aan literatuur betreffende liggewig-skuimbeton dra by tot die stadige vordering in die materiaal-ontwikkeling.

Onlangse vordering in die ontwerp van liggewig-skuimbeton mengsels en effektiewe beheer van die giet-digthede, het gelei tot die oorweging om hierdie beton as 'n strukturele boumateriaal te gebruik d.w.s as 'n gewapende liggewig-skuimbeton.

Hierdie studie klassifiseer die verbindingsgedrag van tipiese vervormde staalbewapening in liggewig-skuimbeton, deur sommige eienskappe met gespesialiseerde toetse te meet en kwantifiseer. Nuwe modelle vir die voorspelling van die verbindingsgedrag word aangebied.

Die tipes beton wat getoets is sluit in normale-gewig beton en liggewig-skuimbeton met giet-digthede van 1200, 1400 and 1600 $\mathrm{kg/m^3}$, waarvan eersgenoemde se resultate as referensie gebruik is. Hierdie materiale is getoets vir vergruisingssterkte, Young's modulus, indirekte trek-splytingsterkte en wig-splyting kraak-energie.

Uittrek- en balk-einde toetse is gebruik om die karakterisering van die verbindingsgedrag te doen. Die ontwerp van hierdie toetse sluit in die belastings, monstervoorbereiding, tegnieke vir glipmeting, kalibrasie van die toetsmasjien vir akurate glipbeheer en 'n metode om die ontwerpsbindingskragte te verkry, gebaseer op 'n fisiese gebeurtenis tydens die toetsing.

Genoegsame druksterktes vir beton, geskik vir strukturele toepassing, is verkry met sommige van die liggewig-skuimbeton toetse, maar alle ander toetse, insluitend die verbindingsgedragtoetse, het nie die voorspelde of gemete spesifikasies van die normale-gewig beton bereik nie.

Die energie benodig om liggewig-skuimbeton beton te kraak is ten minste 'n orde kleiner as dié van normale-gewig beton. Die intrinsieke brosheid van liggewig-skuimbeton word meer met toename in digtheid en die invloed daavan op die verbindingsgedrag is ekperimenteel bepaal. Die balk-einde toetse op die 1600 $\mathrm{kg/m^3}$ beton het 'n vroeë verlies van die verbinding a.g.v. interne krake aangedui, wat verder verswak met toename in digtheid/brosheid.

Die gemete verbindingsgedrag-glipgrafieke toon dat die digter liggewig-skuimbeton 'n relatiewe hoë verbindingspanning lewer, maar dat die styfheid gou verlore gaan a.g.v. splyting. Die min-

der digte liggewig-skuimbeton lewer daarenteen duktiele faling, maar teen 'n baie lae verbindingspanning.

'n Nuwe konsep, genaamd bindingsintegriteit (E: Bonding Integrity), BI, word geformuleer om vroeë versteurings in die bindingsgedrag, soos interne krake, te kwantifiseer. Dit word gedurende die balk-eind toetse gedoen met die meting van die tempo van verandering van die toegepaste moment en die tempo van verandering van trek-kragte in die staal staaf.

Voorspellingsmodelle vir die ontwerp-verbindingspannings word gerapporteer en is geformuleer uit die spanningstoestand by die beton en staal koppelvlak. Die model neem twee falingsmodes in ag, naamlik uittrek- en splytingsfaling.

Die resultate van hierdie studie kwantifiseer en beklemtoon die tekortkomings van liggewig-skuimbeton om strukturele aanvaarbare verbindingsgedrag te lewer. Die minder digte liggewig-skuimbeton het enersyds te min vergruisingsterkte en te veel brosheid aan die ander kant van die digtheidspektrum. Beide gevalle lei tot verlies van verbinding, maar veroorsaak deur verskillende meganismes. Gevolglik word dit aanbeveel dat liggewig-skuimbeton nie gebruik word in strukturele toepassings nie. Verdere ontwikkeling word benodig om die vergruisingsterkte te verhoog en die brosheid te verlaag. Nuwe innoverende bewapening-sisteme kan lei tot die verbeterde verbindingsgedrag vir gevolglike veilige aanwending van liggewig-skuimbeton.

Hierdie studie verskaf nie net resultate en riglyne om gewapende liggewig-skuimbeton te analiseer en karakteriseer nie, maar is ook 'n oorbrugging van die akkute tekort in die spesifikasies van die materiaal en vervaardigings- en toetstegnieke. Dit kan dus dien as die toekomstige basis vir die verdere ontwikkeling daarvan as 'n strukturele materiaal.

Acknowledgements

I would like to express my great appreciation to my supervisor, Professor Gideon Van Zijl, for his continual guidance, encouragement and support throughout this study.

Thank you to my co-supervisor, Mr. Algurnon Van Rooyen, for his contribution and general guidance.

I would like to thank:

The Wilhelm Frank scholarship and the associated trustees, for the funding of my continued studies at the University of Stellenbosch.

John Hulse, from Hulse reinforcing, for the sponsoring of reinforcing steel.

The structural engineering department and laboratory staff from the University of Stellenbosch for their support and guidance.

I would like to express my sincere appreciation to the following persons:

Johan van der Merwe for his meticulous help with constructing and planning of tests. His influence on my work is profound and I thank him for the lessons and skills he taught me.

My office colleges (friends), whom made the bad times good and the good times better.

I would like to highlight my sincere appreciation to my family, whom all supported me during this study:

to my mother for all her never-ending love and support,

to my father for his support, continuous interest in my study and proof reading of this document,

and to my sister for the support and help with photographs.

Above all, thanks to my God for my personal abilities and His abundant guidance.

Contents

List of Figures

List of Tables

Nomenclature

Latin letters:

A - Contact area in mm^2.

a - Steel rib width in mm.

A_{bar} - Cross sectional area of the test reinforcing bar in mm^2.

A_b - A representative rib contact area on which v_b acts at the bond interface in mm^2.

A_c - Area of crack plane in mm^2.

A_s - A representative shear contact area on which v_s acts at the bond interface in mm^2.

a/c - Ash to cement ratio.

b - Outer steel bar diameter in mm.

c - steel rib centre to centre spacing in mm.

c_m - The smaller of the bottom cover or half the clear spacing between bars, in mm.

c_M - The larger of the bottom cover or half the clear spacing between bars, in mm.

c_{clear} - The clear distance in between ribs of steel reinforcement, in mm.

d - Steel outer rib spacing in mm.

E_c - Young's modulus of concrete in GPa.

E_s - Young's modulus of steel reinforcement in GPa.

e - Rib spacing in mm.

F - Force in N.

F_h - Horizontal crack opening force in N.

F_v - Vertically applied force in N.

f - Rib inclination in degrees.

f_c - The characteristic concrete cube compressive strength of in MPa.

f_{cu} - The mean concrete cube compressive strength in MPa.

f_{cub} - Cube compressive strength of the base mix of LWFC, in MPa.

f_{ct} - Mean split cylinder tensile strength in MPa.

f_{ctd} - The characteristic design tensile strength in MPa.

f_{lctd} - The characteristic design tensile strength of LWAC, in MPa.

$f_{ctk,0.05}$ - The 5% fractile value of the characteristic design tensile strength in MPa.

$f_{lctk,0.05}$ - The 5% fractile value of the characteristic design tensile strength of LWAC in MPa.

f_r - The relative rib area.

f_t - Mean cube tensile splitting strength in MPa.

G_f - Specific fracture energy in N/m.

h - Rib height in mm.

I - Integrator operator.

jd - Lever arm of the embedded bar within a structural member in m.

k - Cementing efficiency factor used in LWFC mix design.

L - Debonded length up to the loaded-end slip measuring position in mm.

L_{be} - Length between lateral supports on the BE specimen in m.

L_c - Curvature influencing zone in mm.

l_c - Characteristic length in mm.

l_d - Development length in mm.

l_e - Embedded length in mm.

l_1 - Length of the tensile splitting specimen in mm.

l_2 - Cross sectional dimension of the tensile splitting specimen in mm.

M - Bending moment at a cross section in Nm.

P - Proportional factor or gain in dB.

R - Prefix to plain round mild steel bars of strength 250 MPa.

RD_a - Relative density of fly-ash.

RD_c - Relative density of cement.

RD_f - Relative density of foam.

S - Embedded reinforcement bar slip in mm.

S_d - Design free-end bar slip in mm (0.1 mm).

S_f - Free-end bar slip in mm.

S_l - Loaded-end bar slip in mm.

S_{PR} - The projected area of the ribs of a reinforcing steel bar in mm^2.

S_1 - First characteristic slip value in mm.

S_2 - Second characteristic slip value in mm.

S_3 - Third characteristic slip value in mm.

T - Tensile force in a reinforcing steel bar, in N.

T_b - Bond force in reinforcing steel bar, in N.

T_d - Bond force in reinforcing steel bar at the design point, in N.

t - Time (units indicated).

V - Shear force at a cross section in N.

V_f - Volume of foam in litres.

v_a - Adhesion stress of steel rebar and concrete in MPa.

v_b - Bearing stress caused by steel ribs at bond interface, in MPa.

v_s - Shear stress at bond interface, in MPa.

w_p - Pull-out failure weight factor.

w_s - Splitting failure weight factor.

W/C - Effective water to cement ratio.

w/c - Water to cement ratio.

w/a - Water to ash ratio.

x - Distance along the embedded bar in mm.

x_c - Cement content in LWFC in kg/m^3

Y - Prefix to high yield deformed steel reinforcing bars of strength 450 MPa.

Greek letters:

α - Regression constant of local bond-slip model.

α_b - Binder ratio used in LWFC mix design.

α_{ct} - Coefficient for the long term effects on tensile strength.

β - Bond stress ratio.

δ_b - Bar elongation/shortening in mm.

ϵ - Error originating from the difference between demand and feedback.

ϵ_s - The strain in reinforcement.

ϵ_{sy} - The yield strain of reinforcement.

ϵ_0 - Strain corresponding to 33% of the ultimate strength.

ϵ_1 - Strain corresponding to 40% of the ultimate strength.

ϕ - Steel reinforcing nominal bar diameter in mm.

γ_c - Partial safety factor of concrete.

η_1 - Bond condition factor.

η_2 - Bar size factor.

μ - Ratio of the design bond stresses of the beam-end test to that found from the pull-out tests, both normalized to the target density for equivalent comparison.

μ_{12} - Factor for simulating change in ratio μ observed for beam-end testing of Y12 bars.

μ_{20} - Factor for simulating change in ratio μ observed for beam-end testing of Y20 bars.

ρ - Plastic casting density of LWFC in kg/m^3.

ρ_b - Base mix density of LWFC in kg/m^3.

ρ_{dry} - Oven dry density in kg/m^3.

ρ_{LWAC} - Density of LWAC in kg/m^3.

ρ_t - Target density of LWFC in kg/m^3.

σ_b - Bond stress of embedded bar in MPa.

σ_{bavg} - Average uniform bond stress across the embedded length in MPa.

σ_{bmax} - The peak bond stress in MPa.

σ_d - Design bond stress in MPa.

σ_f - The residual bond capacity in MPa.

σ_s - Tensile stress in the embedded reinforcement in MPa.

σ_0 - Stress corresponding to 33% of the ultimate strength in MPa.

σ_1 - Stress corresponding to 40% of the ultimate strength in MPa.

Abbreviations

BE - Beam-end (referring to the test procedure or test specimens).

COD - Crack Opening Displacement.

COV - Coefficient of Variation.

GFR - Glass Fibre Reinforcement.

ILWC - Infra Lightweight Concrete.

LWAC - Lightweight Aggregate Concrete.

LWFC - Lightweight Foamed Concrete.

LVDT - Linear Variable Displacement Transducer.

NWC - Normal Weight Concrete.

PC - Portland Cement.

PF-LWC - Polystyrene Foam Lightweight Concrete.

PP - Polypropolene.

PO - Pull-out (referring to the test procedure or test specimens).

ROL - Rate of Loading.

RS - Reinforcing Steel.

SARCEA - South African Reinforced Concrete Engineers' Association.

Chapter 1

Prelude

Lightweight foamed concrete (LWFC) is a relatively new building material and is therefore not as well researched, documented and applied in the building industry, when compared to normal weight concrete (NWC) and masonry. Increased commercial utilization of LWFC will only come to fruition when its characteristic properties are better studied and understood. LWFC, which implies the incorporation of protein based foam entrainment to a mortar mix, has some advantages when compared to NWC, though also disadvantages. The entrainment implies reduced concrete density, consequently with many appealing characteristics, such as reduced material usage, self compaction, self-levelling and excellent thermal insulation. The disadvantages are linked to the new material properties, also associated with the reduced density of the material and this study aims to quantify many of these characteristics.

The primary constituents of LWFC are binder materials (usually cement and ash) and water, whereafter air is entrained by foam addition until the required plastic density is obtained. The use for LWFC up to date, extends to non-structural implementation including void filling, trench reinstatement and ground level concrete floors and abutments. Recently developed mix design specifications of LWFC has opened up the possibility of using LWFC as an in-situ structural material.

National standards for design of concrete structures are assembled with NWC as the default building material. The direct substitution of these specifications for LWFC is not recommended and will most likely lead to unsafe structures. This concern originates from the many engineering properties of LWFC, that have not yet been thoroughly investigated and characterized. One of these properties is the performance of bonding of embedded deformed steel reinforcement in LWFC, which should be better studied. This notion is emphasized when considering that the similar characterization of NWC stretches over a vast number of complex empirical evaluations, well documented from as early as 1955.

1.1 Introduction

Concrete is considered a brittle material with excellent compressive capacity, whereas steel is considered a ductile material, capable of handling tensile stresses. The combination of the steel and concrete leads to a hybrid material (reinforced concrete) capable of withstanding both compressive and tensile stress, providing structural engineers with a versatile material suitable

for safe structural systems. Structural members are governed by design to present ductile rather than brittle failure. For the preferred failure to occur, the bond capacity at the concrete-steel interface must be of such quality to ensure that the yield force of the embedded reinforcing bar can be transmitted from the concrete to the steel. This implies that the whole design perspective is based on the ability of concrete to transmit forces through the interface between the steel and the concrete; the bond interface.

The study pertaining to this document addresses the performance of reinforced LWFC and concludes on the characteristic properties observed with the bonding of deformed steel reinforcement in LWFC. In addition, some other engineering properties are also experimentally quantified and compared to those of normal weight concrete (NWC). This study is therefore focussed to further the development of LWFC as a structural material by providing a detailed guidance to the experimental setup and control, measurement and analysis of data to quantify guidelines.

1.2 Motivation

The development of new building materials, with added beneficial properties is always a high priority for further investigative studies, which may have a positive commercial and national economic impact in the near future. The development of LWFC as a reliable structural material is no exception, but, up until now, no studies have been launched or completed that investigate the bond properties of a reinforced LWFC structural system. The evaluation of these properties will permit industries like the pre-fabricated concrete production, together with factory mixing and curing control, to manufacture reliable reduced weight concrete members, which pose obvious economic advantages. The development of these materials might form part of the future solution to the infrastructure shortage in South Africa.

A study to investigate the performance of a reinforced LWFC system could assist in establishing the credibility of LWFC in practice.

1.3 Outline

The motivation and proposal for this study are compiled from information gathered from literature reports dealing with LWFC design and mixing, strength classification and experimental and analytical bond evaluation of concretes. The combined exposure of the existing literature with inputs from colleagues and peers at a public colloquium on this study topic, led to the formulation of an outline for the study, with an experimental structure that is focused on the bond behaviour of LWFC. It incorporates other strength classification tests in order to compare the LWFC mix to other concretes. Experiments are conducted according to standards from various sources and altered in some instances, since these tests are derived from the strengths and properties associated with NWC. Careful measurements and test control provides data suitable for interpretation and evaluation.

A prediction model for the design bond found in conventional pull-out tests is assembled from force equilibrium at the bond interface and modified to incorporate additional safety by ensuring a conservative prediction of design bond stress. The model is also modified to predict design bond stress for the more complicated, and more conservative, beam-end tests.

The study concludes on various characteristic properties of bond performance observed with LWFC and provides recommendations for future research on LWFC and the reinforcing of LWFC.

-o-O-o-

Chapter 2

Literature review

This study of the bond behaviour of deformed reinforcement in lightweight foamed concrete required a comprehensive literature review on sourced topics that cover aspects like the design and mixing of LWFC, the engineering properties of LWFC, theoretical, experimental and analytical bonding between steel and concrete, geometry and properties of deformed steel reinforcement and design considerations for dealing with the bonding between the materials.

Compared to other building materials, LWFC is still relatively new. Consequently it is not as well researched and documented as the others. Previous publications that have a direct or indirect bearing on the shaping and outcome of this study, are presented in the next sections.

2.1 Lightweight foamed concrete

2.1.1 General introduction

The design of lightweight foamed concrete (LWFC) incorporates stable foam particles as temporary air compartments inside a cement based mortar mix. The air entrainment causes a significantly reduced density, which makes LWFC the lighter design option by reducing the overall dead weight of a structure and consequently lowered inertia reaction during dynamic loading. LWFC also has other attractive properties such as high workability, self compaction, self-levelling and thermal insulation. The use of LWFC provides many cost saving solutions, which are useful in the building industries of developing countries and align favourably with the increasing demand for energy efficient systems. A LWFC mix is different to conventional normal weight concrete (NWC), mainly because of the exclusion of aggregates in the mix design. The base mix (cement, ash and water) of LWFC is therefore considered to be a mortar, after which foam is entrained to obtain a predefined required density (the casting density). Typical normal weight concrete (NWC) density is approximately 2400 $\mathrm{kg/m^3}$, whereas acceptable densities for LWFC is between 800 and 1600 $\mathrm{kg/m^3}$.

LWFC is not yet fully established as a structural material in civil engineering practice. One reason for this less favoured use of LWFC is unfamiliarity with the material due to the lack of design specifications and documentation, compared to what is known, documented and implemented for NWC (Jones and McCarthy, 2005). Designers prefer working with a material that is thoroughly standardised and familiar in practice. In order to utilize the benefits of LWFC and

further its development, a researched design guidance for structural use is required. Jones and McCarthy (2005) conducted a study to determine the feasibility of LWFC as a structural material with various strength characterizing laboratory tests. The study stated that 1400 kg/m^3 is the lowest density that yields LWFC suitable for structural use and concluded that factors such as high drying shrinkage, low tensile strength and stiffness, and lack of durability imply that a straight substitution of LWFC for NWC, using the design guidance for NWC, would be considered unsafe.

2.1.2 Mixing LWFC

The mixing of LWFC involves the entrainment of a large volume of air into a base mix, consisting primarily of cement and water, with or without the addition of sand. The mixture used to generate the foam consists of water, foaming agent and ferrous sulphate. One litre of foaming agent is added for every 40 litres of water (1:40). The sulphate is incorporated to ensure stable formation of air bubbles and is added as 4 g per 10 litre mixture. This mixture, together with a jet of air injected through baffles ensures a thick, stable foam. The foam generator is calibrated to produce the foam at a density of 75 g/m^3.

The mixing of NWC depends primarily on the water-cement ratio, which governs the strength classification. Workability is then altered by the addition of water and altering the mix. The NWC allows for a relatively large band within which to alter the mix design to suit workability needs, and still adhering to the required strength classification. The amount of water added into a LFWC mix is of critical importance. LWFC with too much water will result in segregation of the entrained foam and lead to variability of density within a mixture. Too little water will result in the cement extracting water from the entrained foam leading to degradation of the foam, also influencing the effective density and uniform mixing (Kearsley and Wainwright, 2001a). This band of allowed water demand has to be calculated and controlled effectively and the effect of any added filler has to be incorporated into the mix design.

LWFC is mixed in a specially designed mixer with ribbon blades, which moves circularly in the horizontal plane. This mixing action allows for uniform mixing and distribution of the added foam.

Fillers such as fly-ash, crushed dust, polystyrene particles and vermiculite aggregate can be incorporated into a LWFC mix. Kearsley, E.P. and Wainwright, P.J. (2002) conducted a study into the optimum ash replacement for LWFC mix designs and concluded that high additions of fly ash (up to 67%) have shown to be effectively used as a cement replacement without significantly influencing the engineering properties (Kearsley and Wainwright, 2001a). The strength of LWFC is primarily governed by the density and therefore the addition of fly-ash does not influence the strength if worked to the same density. It is known that the addition of fly-ash decreases the early age strength, but increases long term strength (Van Rooyen, 2013; Jones and McCarthy, 2005; Kearsley, E.P. and Wainwright, P.J., 2002). The use of fly-ash also ensures lower heat of hydration because of the reduction of the amount of cement per volume. Therefore fly-ash is almost considered as a standard constituent in a LWFC mix.

2.1.3 Compressive strength

Jones and McCarthy (2005) developed LWFC with the use of fly-ash to obtain material strengths suitable for structural application. For NWC a typical mix resulting in a compressive strength of 20 MPa, or higher, is considered a structural concrete. The mix of Jones and McCarthy (2005) consisted of Portland cement (PC/CEM I), fly-ash, surfactant (synthetic type foaming agent), superplasticiser and polypropylene fibres (19.2 mm length - 0.5% by volume mix). Jones and McCarthy (2005) had success with obtaining the target densities, with plastic densities ranging from 1563 to 1650 kg/m^3 when the target density was set at 1600 kg/m^3. Thus, their results were to within 50 kg/m^3 of the target density, which is considered an acceptable error margin for LWFC mixing.

Jones and McCarthy (2005) used standard 100 mm cube compression tests for determining the compressive strength of the LWFC. The cube strength developments for the LWFC mix are plotted in Figure 2.1. The 1400 kg/m^3, 1600 kg/m^3 and 1800 kg/m^3 target plastic densities of LWFC had ash-cement ratios of 1.154, 1.462 and 1.77 respectively. f_{cu} is the mean concrete cube compressive strength in MPa.

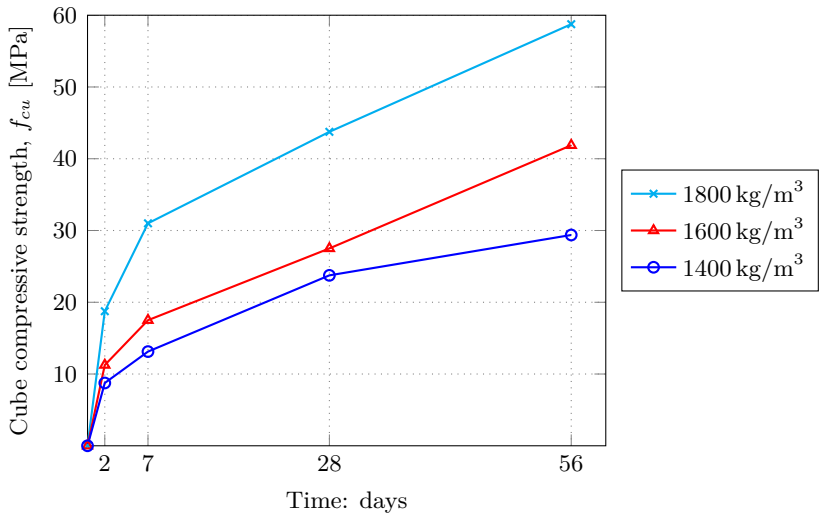

Figure 2.1: The compressive strength development of LWFC with fly-ash additions (Jones and McCarthy, 2005).

From Figure 2.1 it is seen that for a target density of 1600 kg/m^3 the resulting compressive strength surpasses 25 MPa within 28 days, while the 1400 kg/m^3 LWFC falls just below 25 MPa. This is closely corroborated by the results of other publications of typical strengths for LWFC (Addis and Owens, 2009; Byun et al., n.d.).

Table 2.1 indicates typical compressive strengths of LWFC for various target densities (Addis and Owens, 2009), with ρ_{dry} the oven dry density in kg/m^3.

ρ_{dry} [kg/m^3]	400	600	800	1000	1200	1400	1600
f_{cu} [MPa]	1	1.5	2	5	10	15	25

Table 2.1: Typical compressive strengths of LWFC for various oven dry densities (Addis and Owens, 2009).

Kearsley and Wainwright (2001b), together with other publications by these authors, set up models to predict the compressive strength of LWFC as a function of the water-cement ratio, ash-cement ratio, binder ratio and time. Equation (2.1) provides a means to obtain an effective water-cement ratio to be used in further equations, equations (2.2), (2.3) and (2.4).

$$W/C = (w/c)\left[\frac{1}{1+k.(a/c)}\right] \tag{2.1}$$

$$k = \left(0.457 + 0.00315\left(\frac{t}{a/c+1}\right)\right)^2 \tag{2.2}$$

W/C is the effective water-cement ratio, w/c the actual water-cement ratio, a/c the ash-cement ratio, k the cementing efficiency related by equation (2.2) and t the time since casting (days).

W/C is then substituted into equation (2.3).

$$f_{cub} = 88.04 + 6.569ln(t) - 130.5\,(W/C) \tag{2.3}$$

With f_{cub} the cube compressive strength, in MPa, of the base mix (without any foam entrainment).

LWFC compressive strength is not only a function of the water-cement ratio but also of the density ratio. This density ratio is defined as the actual ratio of the concrete to that when fully compacted and at this stage the compressive strength of the paste (no foam entrainment) can be predicted using equation (2.3). Therefore when trying to obtain a relation for compressive strength of LWFC, Kearsley and Wainwright (2001b) pointed out that the only factor that could influence the strength is the amount of air entrained in the paste. The effect of the volume of entrained air is simulated by using the theoretical volumes of binder material per volume, since the paste also contains small amounts of entrained air. The binder ratio, α_b, is introduced in equation (2.4), and is the ratio of the amount of binder materials in the foamed concrete mix to the amount of binder material in the base mix (without foam) as volumes. Therefore the more air is entrained, and consequently less dense the LWFC product, the smaller α_b becomes, which in turn lowers the predicted compressive strength.

$$f_{cu} = 1.172 f_{cub}\,(\alpha_b)^{3.7} \tag{2.4}$$

Figure 2.2 shows the relation of equation (2.4) plotted for various values for a/c and target densities at a constant w/c of 0.37. The figure also indicates the positive effect the ash replacement has on the long term strength development. The models predict a strength advantage after

around 90 days. The progressive increase in compressive strengths for a denser LWFC is also seen.

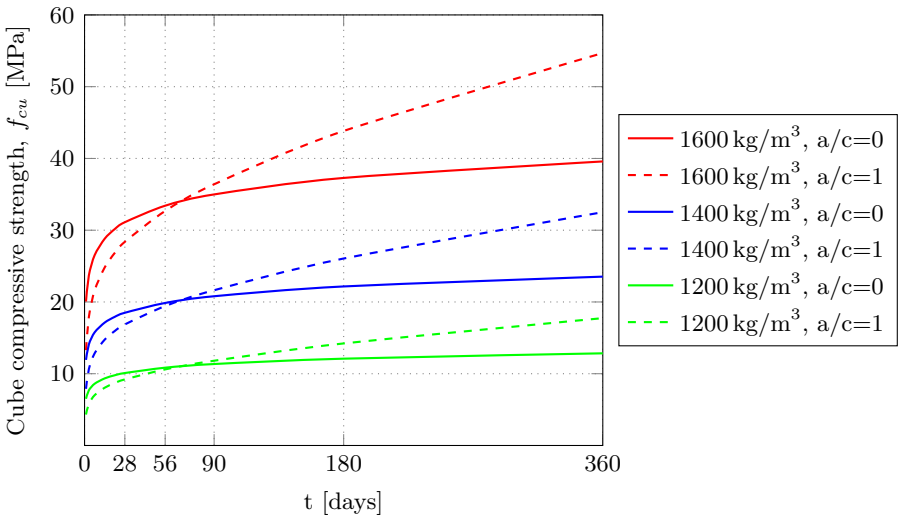

Figure 2.2: The predicted compressive strength development over time for various target densities of LWFC and ash content according to equations (2.1) *through* (2.4).

2.1.4 Tensile strength

Jones and McCarthy (2005) made use of the split cylinder tensile strength (f_{ct}) tests to characterize the tensile capacity of LWFC with ash replacement and these results were compared to the 28-day compressive strengths and also to typical NWC and lightweight aggregate concrete (LWAC) tensile-compressive strength relations found from equations in literature. This is depicted in Figure 2.3.

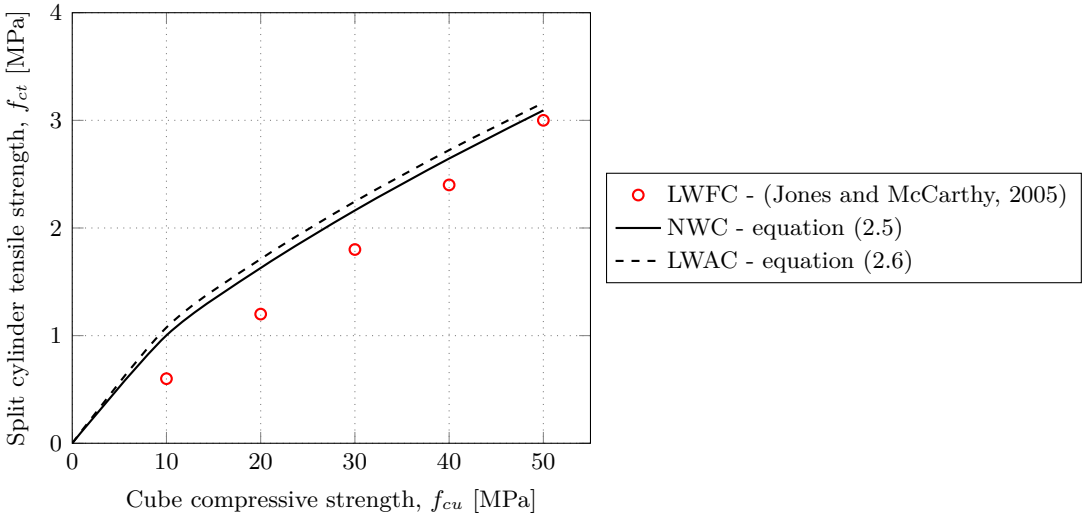

Figure 2.3: Relationships between the split cylinder tensile strength and the cube compressive strength of LWFC from Jones and McCarthy (2005), and published relations for NWC (Oluokun, 1991) and LWAC (Federation Internationale de la Precontraine, 1983).

The NWC relation is described by equation (2.5) (Oluokun, 1991) and the LWAC by equation (2.6) (Federation Internationale de la Precontraine, 1983).

$$f_{ct} = 0.2(f_{cu})^{0.70} \tag{2.5}$$

$$f_{ct} = 0.23(f_{cu})^{0.67} \tag{2.6}$$

where f_{ct} denotes the mean split cylinder tensile strength at 28 days.

The NWC and LWAC indicate larger tensile strengths than for the equivalent LWFC specimen as seen in Figure 2.3. This graph concludes that, although it is possible to acquire the equivalent compressive strengths for LWFC relative to NWC, the tensile splitting strengths are lower than those found for NWC.

2.1.5 Young's modulus

Jones and McCarthy (2005) obtained the LWFC Young's modulus and compared it to predicted values recommended by formulas in literature for NWC and LWAC. Published indicators of expected Young's modulus of LWFC, by Addis and Owens (2009), are also compared and shown in Figure 2.4. The formulas recommended for NWC and LWAC are given by equations (2.7) and (2.8), respectively (BS EN 1992-1-1, 2004).

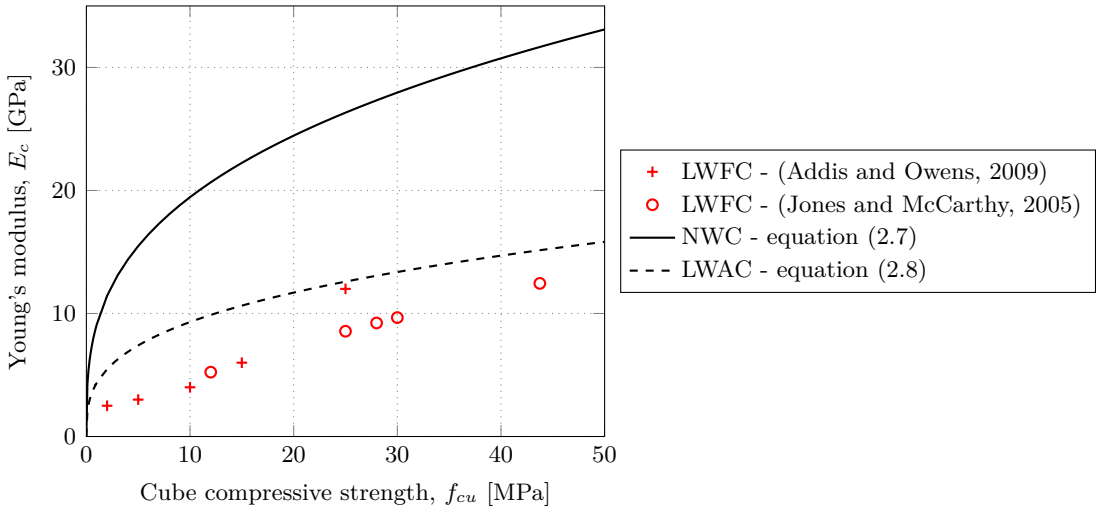

Figure 2.4: Relationships between the Young's modulus and the cube compressive strength of LWFC from Jones and McCarthy (2005) and Addis and Owens (2009), and published relations for NWC (equation (2.7)) and LWAC (equation (2.8)) from BS EN 1992-1-1 (2004).

$$E_c = 9.1(f_{cu})^{0.33} \tag{2.7}$$

$$E_c = 1.7 \times 10^{-6} (\rho_{dry})^2 (f_{cu})^{0.33} \tag{2.8}$$

where E_c denotes the Young's modulus in GPa.

The observation is made that the LWFC Young's modulus is lower than those of the equivalent NWC and LWAC. It is observed that the value for LWAC is also substantially lower than for NWC and this building material has been implemented in design codes; §11 of BS EN 1992-1-1 (2004). This implies that studies on a new material could result in design considerations used to allow effective and safe structural design. From Figure 2.4 the LWFC Young's modulus by Jones and McCarthy (2005) can be characterized by equation (2.9) as a function of cube compressive strength.

$$E_c = 0.99(f_{cu})^{0.67} \tag{2.9}$$

Taking the reduced Young's modulus into account together with the reduced tensile splitting strength, Jones and McCarthy (2005) state that substituting LWFC in the place of NWC with the same compressive strength classification will be unsafe for structural design.

2.1.6 Fibre reinforcement

In the study by Jones and McCarthy (2005) the addition of 19.2 mm long, flexible polypropolene (PP) fibres was investigated and concluded on its effect on the engineering properties of LWFC. The fibres increased both the compression, flexural and Young's modulus values. The compressive strengths at a 0.5% by volume fibre content and a density of 1400 kg/m^3 were up to 52% higher than the reference strength. It was noted that with addition of fibres the workability, which is a beneficial property of LWFC, reduces significantly. Consequently it is suggested that the fibre addition be kept at (or below) 0.5% of the mix volume. The addition of PP fibres does exhibit the possibility of increasing the splitting tensile strength in lightweight concrete (Jones and McCarthy, 2005; El Zareef and Schlaich, 2008; Addis and Owens, 2009).

El Zareef and Schlaich (2008) conducted a study to determine the bond behaviour of various reinforcement types in Infra-Lightweight Concrete (ILWC). The reinforcement tested was Glas-Fibre Reinforcement (GFR) and typical reinforcing steel (RS). The study investigated the effect of polypropolene (PP) fibres on engineering parameters. The addition of PP fibres (1 kg/m^3) had both positive and negative effects on ILWC. Fibres of mean lengths of 6, 12 and 20 mm were used during the investigation. The concrete tensile strength increased with 10%, 23% and 30% for the respective fibre lengths, relative to the control mixes without the addition of PP fibres. El Zareef and Schlaich (2008) claim that this is due to the fact that a great amount of energy is absorbed during the de-bonding and pull-out of the fibres in the concrete before the concrete reaches a complete failure stage. The addition of PP fibres showed a reduction in the cube compressive strength of 56%, 43% and 41% for the various increasing fibre lengths respectively. This is thought to be the result of the fact that the fibres trigger early micro cracks in the concrete matrix, especially with a low compressive strength material. Jones and McCarthy (2005) showed that for a material with larger strength this is not the case when PP fibres are added. It is concluded that the use of long PP fibres is more effective than using short fibres (El Zareef and Schlaich, 2008; Jones and McCarthy, 2005).

Similar to the study by El Zareef and Schlaich (2008) a study was conducted by Byun et al. (n.d.) to develop a structural lightweight concrete in which the effect of adding fibre reinforcement into the mix was observed. Vynylon fibres were mixed into the LWFC mix and the 28-day tensile tests and flexural tests were compared. The addition quantity of these fibres were not reported. It was found that the addition of fibres led to a 97% increase and 104% increase in concrete tensile strength for the use of 19 mm and 30 mm vynylon fibres, respectively. The concrete flexural strength increased by 30% with the addition of 30 mm vynylon fibres.

Kearsley and Mostert (2003) launched a study to determine the effect of synthetic fibre in LWFC on crack formation and impact resistance. They concluded that the use of chopped PP fibres does not enhance the compressive strength or the Young's modulus. The use of fibres in LWFC do however improve the post-crack strength and therefore reduces the handling damages of LWFC structural elements. The use of PP fibres does not affect the LWFC porosity or sorptivity.

2.2 Theoretical bond

Bonding is the ability of two materials to adhere and transmit forces from one to another. The bond capacity is greatly influenced by the two materials and the interaction at the bond interface. Figure 2.5 shows a steel bar embedded in a concrete specimen (left) with the distributions of bar slip ($S(x)$), tensile stresses in the bar ($\sigma_s(x)$) and the bond stress ($\sigma_b(x)$) being indicated to the right. This is a presentation of a typical pull-out test with the accompanying stresses present in the bar and at the bond interface.

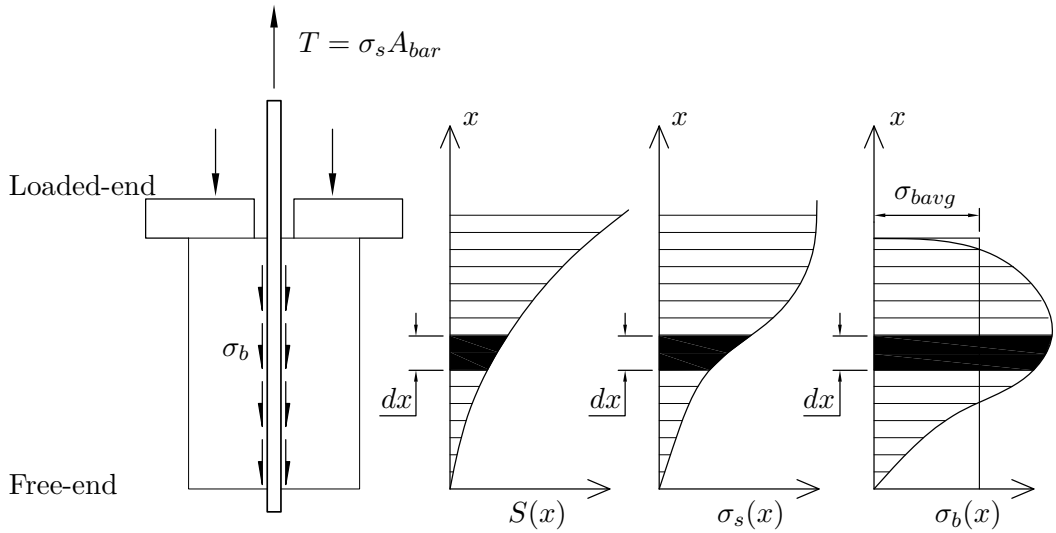

Figure 2.5: Loaded embedded steel bar in concrete (left) with distributions of bar slip, tensile bar stress and bond stress to the right. Adapted from Penelis and Penelis (2014).

Free-end slip is when the free-end of the bar (indicated in Figure 2.5) starts to slip. When viewing the slip distribution over distance x, it is seen that zero slip occurs at the free-end, and a maximum slip is found at the loaded-end. This is as a result of elongation of the bar due to tensile stresses and partial de-lamination starting at the loaded-end. The axial stress

distribution is also zero at the free-end whereafter it develops to a constant magnitude, which will equal the tensile force in the bar acting on the bar cross sectional area only. Since it is known that the bar force at the free-end of the bar is zero, no bond stress can exist. An exact bond stress distribution is unknown, but it is accepted to assume a constant uniform bond stress distribution of magnitude σ_{bavg} for small embedded lengths (Penelis and Penelis, 2014).

Figure 2.5 also indicates a differential element of length dx along the embedded length. This element is enlarged in Figure 2.6 with the indicated stresses and forces present. T is the tensile bar force, A_{bar} the bar cross sectional area and ϕ the bar diameter.

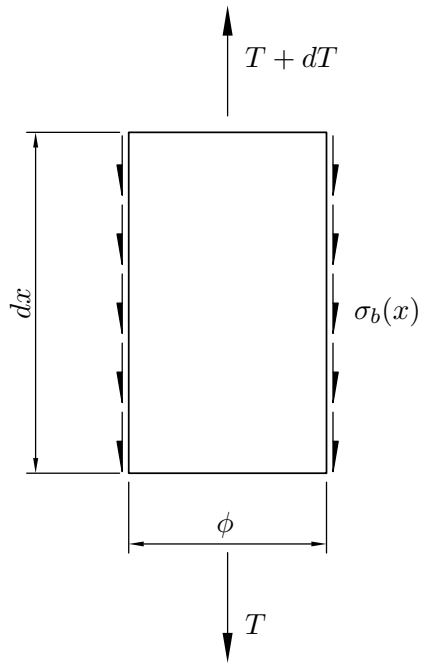

Figure 2.6: A differential element of length dx enlarged from Figure 2.5. Adapted from Penelis and Penelis (2014).

Equilibrium conditions on the differential element in Figure 2.6 yield equation (2.10).

$$\left(\frac{\pi.\phi^2}{4}\right) d\sigma_s = (\pi.\phi.\sigma_b)\, dx$$

simplified to

$$d\sigma_s = \left(\frac{4}{\phi}.\sigma_b\right) dx \tag{2.10}$$

where

σ_s is the axial (tensile) stress in the steel bar, in MPa,

ϕ is the nominal diameter of the embedded steel bar, in mm,

σ_b is the bond stress along the steel bar, in MPa, and

dx is the differential element length.

From equation (2.10) it can be concluded that any change in the axial stress along the bar will result in bond stress development at the interface between concrete and steel. It is therefore not possible for tensile stresses to develop without the bonding action between reinforcement and concrete. The bond stresses occur as a result of various force transfer mechanisms. These mechanisms are firstly the chemical adhesion of the cement paste on the steel reinforcement and ranges from around 0.5 to 1.0 MPa. The point at which this mechanism is exhausted, is accompanied by the onset of free-end slip of the reinforcement. After the adhesion breaks down, slip initiates and friction is developed by shear stresses. Confinement and transverse pressures increase this frictional shear bond. Mechanical interlock then follows as a result of the steel ribs crushing and wedging the concrete in between the ribs. This phase enhances the bond stress until the resulting circumferential stress becomes large enough for splitting failure at the free surface of the concrete to occur or the bar pulls free from the concrete. This mechanism for bond development is enhanced when adequate confinement is provided and also helps prevent splitting failure. The mechanical interlock comprise a complex failure mechanism accompanied by internal cracks. This mode is influenced by both the surrounding concrete properties and the steel geometry. In experimental studies the bond stress is measured as the result of all three bond mechanisms and is usually obtained in the form of the bond-slip relation with experiments such as the pull-out test.

Figure 2.7 shows a typical pull-out concrete specimen with the resulting bond-slip envelope. This figure shows that a design bond value is not the ultimate bond (peak), or even the mean bond, but rather the bond stress ,σ_d, corresponding to a certain free-end slip, the design slip, S_d. This approach originated from German lectures on concrete design (Leonhardt, 1977) and has been effectively incorporated in literature (Penelis and Penelis, 2014; Farghal Maree and Hilal Riad, 2014; Sung-Nam et al., 2008).

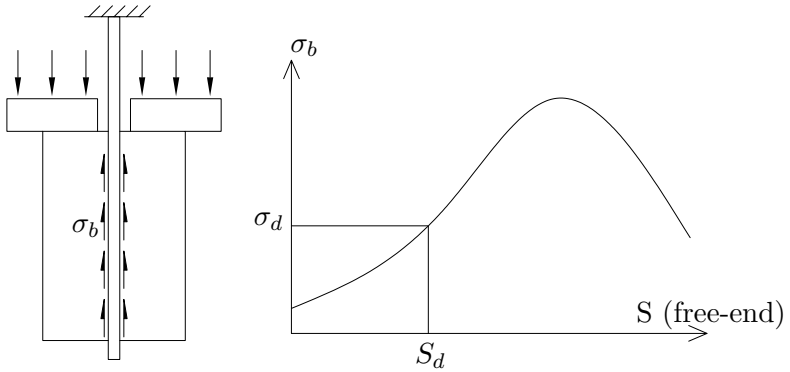

Figure 2.7: A typical pull-out test with the experimental setup (left) together with a typical measured bond versus free-slip envelope. This figure points out the design bond stress correlated to a specific slip measurement. Adapted from Penelis and Penelis (2014).

2.3 Experimental bond

2.3.1 Bond behaviour of lightweight concretes

In 2013 a study was conducted on the bond behaviour of a newly developed lightweight concrete, which partially replaces the normal weight aggregates with polystyrene foam particles (Farghal Maree and Hilal Riad, 2014). Polystyrene foam lightweight concrete (PF-LWC) has shown to incorporate a weight reduction of 15 to 20% relative to the NWC equivalent. The study investigated the bond behaviour on both an experimental level and analytically. The analytical phase comprised of the set up of a model that would be able to predict bond behaviour of PF-LWC flexural members (refer to Section 2.4.2) and the experimental phase comprised of standard pull-out (PO) and beam-end (BE) tests. The PF-LWC specimens were tested alongside a NWC equivalent, which enables a comparison to what is perceived as sufficient structural bond in NWC. This is done by various researchers in previous studies (Farghal Maree and Hilal Riad, 2014; Jones and McCarthy, 2005; Jumaat et al., 2009; Johnson Alengaram et al., 2010; Dae-Jin et al., 2014; Sancak et al., 2011).

The bond mechanism between steel reinforcing and concrete depends on many parameters which include; the strength of surrounding material with its properties, embedded length, the amount of confinement reinforcement, the concrete cover, the occurrence of splitting cracks, reinforcement steel stress, lateral pressure, direction of casting, reinforcement bar diameter and the spacing between reinforcing bars. The correct set up of an experimental structure is therefore of importance since all these factors can have a profound influence on the bond behaviour.

The PO test according to ASTM C234, provides the most efficient manner of determining bond strength. The PO test is similar to what is presented in Figure 2.7. This standard has been withdrawn from the ASTM database for unknown reasons. However it has been used in 2014 in a study (Dae-Jin et al., 2014), which renders the test method still useful as a comparative tool. Farghal Maree and Hilal Riad (2014) used the PO test with test variables: type of concrete (NWC and PF-LWC), nominal reinforcement bar diameters 12 mm, 16 mm and 22 mm and the embedded lengths of 2, 3 and 4 bar diameters.

The failure mode during the PO tests is considered to be either pull-out or splitting failure. In the study by Farghal Maree and Hilal Riad (2014), most of the specimens showed splitting failure. Pull-out failure is characterized by the test bar pulling out of the concrete specimen along a cylindrical shear face when the concrete keys between the ribs of the steel bar have sheared off. Splitting failure occurs when the tangential stress in the concrete, caused by the radial pressure from rib bearing, exceeds the splitting tensile strength of the concrete and splits the specimen; effectively breaking all bond resistance. The splitting failure mode yields lower bond stress values than the pull-out failure and is therefore considered more critical in design. This tendency of PF-LWC to fail in splitting mode is what is expected since the tensile splitting strength of PF-LWC is much lower than the NWC equivalent (refer to Figure 2.3), and is reported in many studies involved with lightweight concretes and associated bond stresses (Farghal Maree and Hilal Riad, 2014; Dae-Jin et al., 2014; Sancak et al., 2011). Active and passive confinement

are some of the measures to prevent splitting failure and will be addressed later in this section.

Since not all test specimens have the same compressive strength due to variability in mixes, Farghal Maree and Hilal Riad (2014) introduce a bond stress ratio β which is given by equation (2.11).

$$\beta = \frac{\sigma_b}{\sqrt{f_{cu}}} \tag{2.11}$$

This factor is introduced to be able to effectively compare test results of specimens with various compressive strengths and to simplify the comparisons between specimens, to a common base parameter. This factor was obtained by substituting the recorded bond stress, σ_b (in MPa), and compressive strength, f_{cu} (in MPa), into equation (2.11), yielding a bond stress ratio of unit $\text{MPa}^{\frac{1}{2}}$. The correct use of this normalizing factor has to be considered. The same relation between the bond stress and concrete compressive strengths may not be used for different types of concrete. For example the ratio might be representative of NWC, but not necessarily for PF-LWC, LWAC or LWFC. In this case the bond stress ratio may not be used to compare bond stresses and a simple comparison of only σ_b will suffice a more accurate correlation.

In the ACI code (ACI 318-11, 2011), the Eurocode 2 (BS EN 1992-1-1, 2004) and the South-African standard (SABS 0100-1, 2000) the allowable maximum crack width is specified in the order of 0.1 - 0.4 mm for reinforced concrete structures. It is therefore common in studies (Sung-Nam et al., 2008; Farghal Maree and Hilal Riad, 2014) to accept the design bond stress at a slip of 0.1 mm, as introduced in Section 2.2. Slip is a primary mechanism for crack growth (Leonhardt, 1977). Farghal Maree and Hilal Riad (2014) obtained the design bond stress, σ_d, at 0.1 mm and found that PF-LWC yields a significantly lower design bond stress than the NWC. The bond stress ratios, β, were then obtained by substituting σ_b with σ_d in equation (2.11), and compared in Figure 2.8 for NWC and PF-LWC.

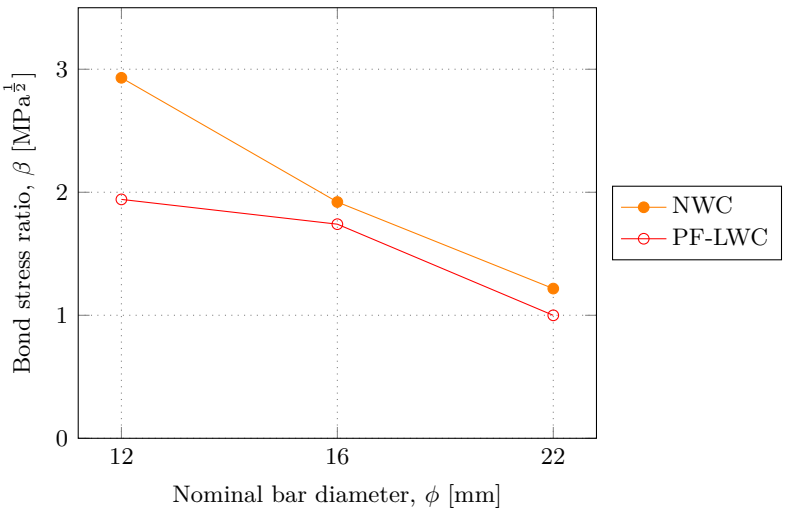

Figure 2.8: The bond stress ratios for various bar diameters of PF-LWC and NWC obtained from PO tests by Farghal Maree and Hilal Riad (2014).

When observing the design bond stress ratios it is concluded that the PF-LWC has a lower bond

stress ratio, especially at the smaller bar diameter (12 mm). At bar sizes 16 mm and 22 mm the difference is much less. However for both NWC and LWC there is a reduction in bond stress ratio observed for an increase in bar diameter. The increase in bar diameter effectively lessens the cover (passive confinement) and therefore increases the susceptibility of the concrete to fail in tensile splitting failure, which yields a more conservative design bond capacity.

The effect of the embedded length on the type of failure mode was also of concern with the study of Farghal Maree and Hilal Riad (2014). In their tests embedded lengths of $3\,\phi$ and $4\,\phi$ were used. The results for the average bond strength (σ_{bavg}) resulting from various embedded lengths (l_e) are summarized in Table 2.2 for PF-LWC.

Table 2.2: Average bond strengths (σ_{bavg}) obtained for PF-LWC specimens with varying embedded lengths (l_e) (Farghal Maree and Hilal Riad, 2014).

ϕ	l_e	σ_{bavg}	Failure
12	3ϕ	26.85 MPa	Pull-out
12	4ϕ	22.01 MPa	
16	3ϕ	19.31 MPa	Splitting
16	4ϕ	15.67 MPa	

In the table above it is observed that the longer embedded length yields the more conservative average bond stress. This occurs since a longer embedded length, together with a larger diameter bar, causes splitting failure more readily, which in turn results in a more conservative bond capacity.

Farghal Maree and Hilal Riad (2014) also investigated the effect of confinement stirrups on bond in PF-LWF and NWC. This was done with BE tests conducted according to specifications from ASTM A944-10 (2002). Table 2.3 summarizes the design bond stress ratios obtained for the NWC and PF-LWC for both confined and unconfined conditions. The design bond stress was taken at 0.1 mm slip. On all accounts the confined specimens ensured an average bond stress ratio increase of at least 4%. With increasing bar diameter the bond stress ratio decreases and NWC yields larger bond stress ratios for all bar diameters and confinement regimes.

Table 2.3: Design bond stress ratios for NWC and LWC, with and without confinement (Farghal Maree and Hilal Riad, 2014).

	Confined				Not confined			
	PF-LWC		NWC		PF-LWC		NWC	
ϕ	12	16	12	16	12	16	12	16
β	1.64	0.94	1.81	1.41	1.49	0.82	1.73	1.40

El Zareef and Schlaich (2008) studied the effect of confinement to explain the relation of confining steel to the bond development. For both reinforcing steel (RS) and glass-fibre reinforcing (GFR), two stirrups with 60, 90 and 120 mm side lengths were used as confining steel. It was found that the steel with side lengths of 90 and 120 mm showed no remarkable change in the bond behaviour of both RS and GFR. In the case of the 60 mm side length confining steel the maximum bond stress was increased with 3% and 37% and reduced the slip at maximum bond stress by 57% and 95% in the cases of GFR and RS, respectively. This reduction in slip at maximum bond is favourable for crack width control at serviceability limit states.

Confinement can be categorized into active and passive confinement. Active confinement is transverse pressure provided by secondary reinforcement and passive confinement is the concrete cover. A larger concrete cover provides a longer crack path for internal cracks, which ensures a larger bond stress development prior to splitting failure. Generally it is found that increase in either confinements results in an improved bond strength (Model Code, 2010; El Zareef and Schlaich, 2008). As seen in Figure 2.9, transverse pressure initially has a beneficial influence on bond strength when splitting failure mode governs. With increasing transverse pressure this failure mode shifts from splitting to pull-out failure. As soon as pull-out failure governs transverse pressure do not have as significant positive influence on the bond strength and eventually any increase in transverse pressure will yield the same bond stress. This suggest that enough confinement should be provided to ensure that pull-out failure occur, but also ensure to keep the design economical without adding too much transverse pressure.

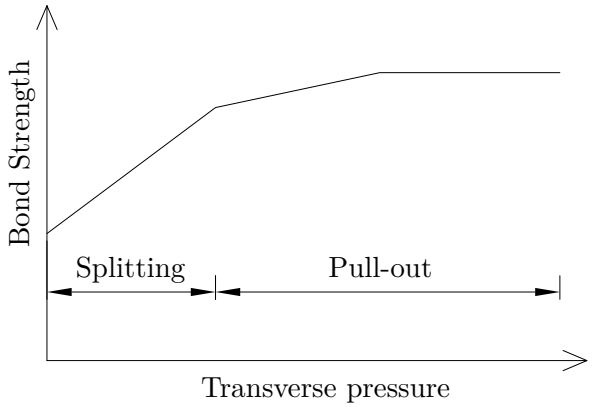

Figure 2.9: The influence of transverse pressure (confinement) on bond strength and failure mode (Model Code, 2010).

The study by El Zareef and Schlaich (2008) resulted in variation in bond stresses for various PP fibre mixes and the results are depicted in Table 2.4. It is noted that the 20 mm fibres increased the bond for RS by 25%. The bond stresses were obtained from typical PO tests. El Zareef and Schlaich (2008) state that the reduction in compressive strength with the use of PP fibres was balanced with an increase in tensile strength. The use of PP fibres in ILWC yielded a lowered slip at maximum bond stress, which is better for crack width control in the serviceability limit state.

Table 2.4: The relative change in maximum bond stresses for ILWC with PP fibres of various lengths compared to a ILWC mix without any fibre reinforcement (El Zareef and Schlaich, 2008).

Fibre length	**RS**	**GFR**
6 mm	↓ 2.4%	↓ 37%
20 mm	↑ 25.3%	↑ 4.6%

2.3.2 Bond behaviour of lightweight aggregate concrete

A study conducted by Dae-Jin et al. (2014) investigated the bond strength of deformed steel reinforcement in artificial lightweight aggregate concrete (LWAC). The results from PO tests led to data used to formulate an expression for predicting the bond strength through a regression analysis.

The variables in the tests were: four concrete types (3 LWAC and 1 NWC), three diameters of reinforcing steel bars (13 mm, 16 mm and 19 mm) and four embedded lengths (40 mm, 80 mm, 120 mm and 150 mm).

The PO tests were performed according to ASTM C 234, which has been withdrawn from the ASTM database since 2000. The author was unable to locate and reference the document. For the PO tests the bar slip was measured at both the loaded-end (the side of the specimen where the bar is being loaded) and free-end (the opposite side of the specimen, which does not experience any direct loading) of the reinforcing bar. The measurement at the loaded-end measures the elongation of the bar in addition to the free-slip. Equation (2.12) shows the relation between the free-end (S_f) and loaded-end slip (S_l).

$$S_f = S_l - \delta_b \tag{2.12}$$

The elongation of the bar is given by

$$\delta_b = \frac{T.L}{E_s.A_{bar}}$$

, with T the bar load in Newtons, L the length of debonded part of the bar in mm, E_s the Young's modulus of the bar in MPa and A_{bar} the cross-sectional area in mm^2.

The identified failure mode of the specimens were either yielding of the steel bars, tensile splitting failure or pull-out failure. It was found that pull-out failure occurs more frequently in NWC than LWAC, as well as with reduction in embedded length or the rebar diameter. Dae-Jin et al. (2014) state that the main difference between failure in the NWC and LWC is that more splitting failures occur for the LWC specimens. This is a result of reduced tensile strength of LWC specimens to a NWC equivalent. This conclusion is depicted in Figures 2.10 and 2.11.

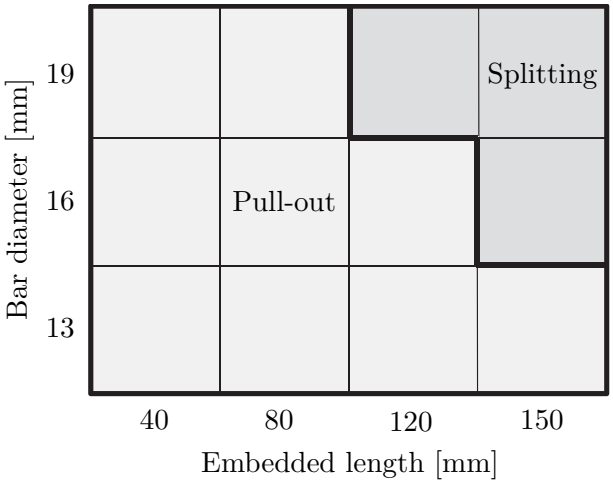

Figure 2.10: NWC specimens failure modes (Dae-Jin et al., 2014).

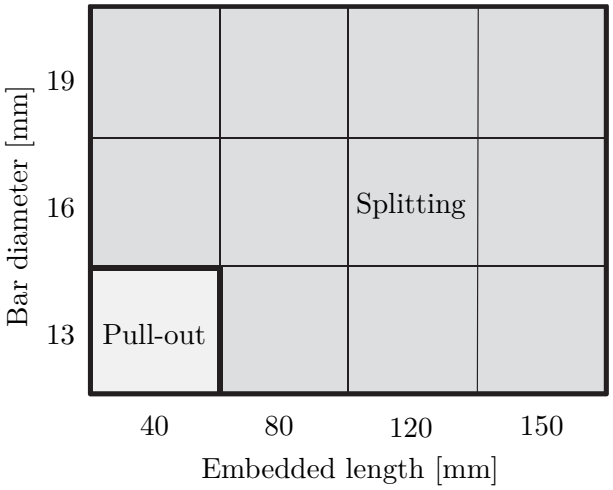

Figure 2.11: LWAC specimens failure modes (Dae-Jin et al., 2014).

The various failure modes are easily identified when viewing the acquired load-slip curves from pull-out tests. Pull-out failure is represented by an ascending bond strength with increase in slip, up to a peak bond stress. After the peak the bond stress diminishes and attains a constant residual bond stress at substantial slip measurements. This failure is categorized into five stages: microslip, internal cracking, pull-out, descending and residual. Microslip is characterized by small loads and therefore almost no slip is recorded at the free end of the steel bar. When internal cracking stage is reached, slip begins to occur and the load increases to a critical value, which is where the adhesion between the two materials is surpassed. After this the test enters into the pull-out phase until an ultimate load is reached. A residual bond is maintained after the peak load of about 10 to 20% of the ultimate load.

The splitting failure load-slip curve is identified by a similar increase in bond stress as seen for pull-out failure, but with a sudden and premature failure indicated by a sudden drop in bond stress. Once the resistance is lost the bar force drops and zero bond is attained. This happens when the local tensile stresses at the material interface surpass the concrete tensile strength, leading to internal cracks which propagate to the concrete surface.

Dae-Jin et al. (2014) concluded that the bar size has minor influence on the bond strength and that the bond strength is inversely proportional to the embedded length and directly proportional to the concrete compressive strength.

Dae-Jin et al. (2014) compared the acquired bond strengths with bond strengths published for NWC to see whether these equations can be applied directly to LWAC concrete. The equations used for comparison are summarized in equations (2.13) to (2.15) with the references indicated.

From ACI Committee 408 (1992):

$$\sigma_b = 20.23\frac{\sqrt{f_{cu}}}{\phi} \tag{2.13}$$

From Orangun et al. (1977):

$$\frac{\sigma_b}{\sqrt{f_{cu}}} = 0.1 + 0.25\left(\frac{c_m}{\phi}\right) + 4.15\left(\frac{\phi}{l_e}\right) \tag{2.14}$$

From Zuo and Darwin (2000):

$$\frac{T_b}{f_{cu}{}^{\frac{1}{4}}} = \left[1.44l_e\left(c_m + 0.5\phi\right) + 56.3A_{bar}\right]\left(0.1\frac{c_M}{c_m} + 0.9\right) \tag{2.15}$$

where

σ_b is the bond strength in MPa,

ϕ is the diameter of the reinforcing bar in mm,

f_{cu} is the compressive strength of concrete in MPa

l_e is the embedded length of the reinforcing bar in mm,

c_m is the smaller of clear bottom cover or half of the clear spacing between bars in mm,

c_M is the largest of clear bottom cover or half of the clear spacing between bars in mm,

T_b is the ultimate bond force in N and

A_{bar} is the cross-sectional area of the reinforcing bar in mm^2.

The comparisons between the experimental results for the LWAC did not correlate with the equations taken from literature for NWC and concluded that for these relations the LWAC cannot simply be substituted in place of NWC. Therefore it is necessary for new building materials to be characterized by an empirical or analytical study.

Dae-Jin et al. (2014) therefore performed a regression analysis in order to obtain an equation suitable for determining the bond strength for LWAC. The main parameters used in the regression analysis were $(\phi + l_e)^{\frac{1}{4}}$ and $\frac{\sigma_b}{\sqrt{f_{cu}}}$ which lead to equation (2.16) with a coefficient of determination of 0.8.

$$\frac{\sigma_b}{\sqrt{f_{cu}}} = \frac{37.5}{(\phi + l_e)^{\frac{1}{4}}} - 9.4 \tag{2.16}$$

2.4 Bond behaviour: Analytical models

2.4.1 Model Code

Model Code (2010) states that under well-defined conditions it is possible to statistically accept a bond-slip relationship when short anchorage lengths are considered. The Model code provides an analytical model to represent the bond-slip relation according to the standardized reinforcement specified in §5.2. Therefore this analytical model describes the bond between the concrete and the reinforcing steel in terms of the relative displacement (S), parallel to the bar axis at the material interface. Figure 2.12 represents this analytical model and is subject to the piecewise equation (2.17) introduced below, that provide a stepwise algorithm to derive a predicted bond-slip envelope. The variables in the equations correlate to the variables in Figure 2.12 with σ_b the bond stress in MPa, σ_{bmax} the peak bond stress in MPa, σ_f the residual bond stress in MPa, S slip in mm, S_1, S_2 and S_3 characteristic slip values in mm.

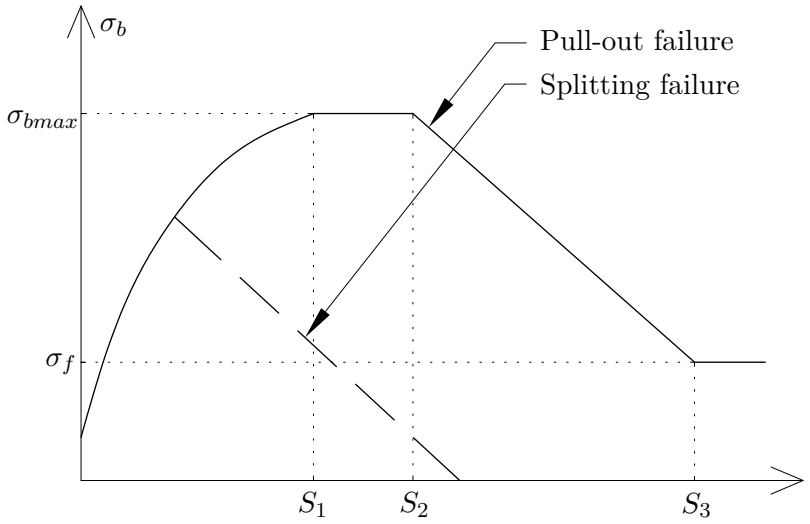

Figure 2.12: Analytical model of the bond-slip relation (Model Code, 2010).

$$\sigma_b = \begin{cases} \sigma_{bmax}\left(\dfrac{S}{S_1}\right)^{\alpha} & \text{for } 0 \leq S \leq S_1 \\ \sigma_{bmax} & \text{for } S_1 \leq S \leq S_2 \\ \sigma_{bmax} - (\sigma_{bmax} - \sigma_f)\dfrac{(S - S_2)}{(S_3 - S_2)} & \text{for } S_2 \leq S \leq S_3 \\ \sigma_f & \text{for } S_3 \leq S \end{cases} \tag{2.17}$$

The variable values for various conditions are given in Table 2.5. These variables are primarily governed by the failure mode and secondly by the bond conditions which exist within each failure mode. The Model Code correlates the casting position with the acquired bond condition.

Table 2.5: The bond-slip model parameters for different failure modes, bond conditions and confinement regimes (Model Code, 2010).

	Pull-out failure		**Splitting failure**			
	$\varepsilon_s < \varepsilon_{s,y}$		$\varepsilon_s < \varepsilon_{s,y}$			
	Good bond cond.	**other bond cond.**	**Good bond cond.**		**other bond cond.**	
			Unconfined	**Confined**	**Unconfined**	**Confined**
σ_b	$2.5\sqrt{f_{cu}}$	$1.25\sqrt{f_{cu}}$	$7(f_{cu}/25)^{0.25}$	$8(f_{cu}/25)^{0.25}$	$5(f_{cu}/25)^{0.25}$	$5.5(f_{cu}/25)^{0.25}$
S_1	1.0	1.8	$S\left(\sigma_{bmax}\right)$	$S\left(\sigma_{bmax}\right)$	$S\left(\sigma_{bmax}\right)$	$S\left(\sigma_{bmax}\right)$
S_2	2.0	3.6	S_1	S_1	S_1	S_1
S_3	c_{clear}	c_{clear}	$1.2S_1$	$0.5c_{clear}$	$1.2S_1$	$0.5c_{clear}$
α	0.4	0.4	0.4	0.4	0.4	0.4
σ_f	$0.4\sigma_{bmax}$	$0.4\sigma_{bmax}$	0	$0.4\sigma_{bmax}$	0	$0.4\sigma_{bmax}$
with c_{clear} the clear distance between ribs of steel reinforcement.						
with ε_s and $\varepsilon_{s,y}$ being the reinforcement strain and yield strain respectively.						
with α the regression constant used for empirical data fit.						
with σ_f the residual bond capacity as a result of confinement steel.						

2.4.2 Proposed models by previous studies

Farghal Maree and Hilal Riad (2014) continued their study, as introduced in section 2.3.1, with an analytical representation for the bond-slip relationship. The study made use of equations describing the slip-bond relation according to CEB-FIP 1990 model code, which is the same as the equations represented from the Model Code 2010, introduced earlier in this section.

Farghal Maree and Hilal Riad (2014) stated that the model proposed by CEB-FIB neglects the fact that for bars with relatively large rib area, the bond strength increases and the slip value decreases. Therefore in order to account for the effect of bar diameter and concrete type the

parameters as stated in CEB-FIB had to be modified for NWC and LWC. The test results were fitted to a curve and the parameters for the use of equations were obtained as represented in Table 2.6.

Table 2.6: Modified parameters for the bond-slip model of Model Code (2010) from experimental results for both NWC and PF-LWC (Farghal Maree and Hilal Riad, 2014).

Parameter	**NWC**	**PF-LWC**
S_1	$0.11e^{0.054\phi}$	$0.11\times1.1e^{0.054\phi}$
S_2	$0.11e^{0.054\phi}$	$0.11\times1.1e^{0.054\phi}$
S_3	1	1
α	0.4	0.55
σ_{bmax}	$10.4\phi^{-0.35}\sqrt{f_{cu}}$	$10.4\times1.1\phi^{-0.35}\sqrt{f_{cu}}$
σ_f	$0.15\sigma_{bmax}$	$0.15\sigma_{bmax}$

2.5 Bond in design documents

2.5.1 NWC and LWAC (BS 8110-1, 1997)

BS 8110-1 (1997) introduce a method for determining the design bond stress for various concrete strengths of NWC. The bond stress, σ_b, is obtained with equation (2.18), and is shown to be dependant on the concrete cube compressive strength, which correlates to the method adopted for comparison between concretes using the bond stress ratio in Section 2.3.1.

$$\sigma_b = \beta\sqrt{f_c} \tag{2.18}$$

with

β the bond stress ratio dependant on the bar type (refer to Table 2.7) , and

f_c the characteristic cube compressive strength of concrete.

Table 2.7: Bond stress ratios (β) for various bar types and loading states.

Bar type	Bars in Tension	Bars in Compression
Type 1: deformed	0.40	0.50
Type 2: deformed	0.50	0.63

It is suggested that the deformed bar used in South-Africa conforms to the type 2 deformed bar (Robberts and Marshall, 2010). Therefore if a 30 MPa mean compressive strength (±22 MPa characteristic strength) NWC, and a type 2 deformed embedded bar are considered, a design bond stress of 2.35 MPa is expected.

A supplementary clause is given in BS 8110-2 (1985) for the use of LWAC. It specifies that an initial design bond stress be obtained as is done above for NWC, where after it is multiplied with a factor of 0.8 to obtain the design bond in LWAC. This is identical to the method provided in the South African standards (SABS 0100-1, 2000), §4.12. Therefore the LWAC equivalent will be 80% of 2.35 MPa which yields 1.88 MPa.

2.5.2 NWC and LWAC (BS EN 1992-1-1, 2004)

In BS EN 1992-1-1 (2004) the design bond stress is determined by equation (2.19), which indicates that the design bond value is directly proportional to and dependant on the characteristic tensile strength of the concrete, which is in turn dependant on the compressive strength as before.

$$\sigma_b = 2.25 \cdot \eta_1 . \eta_2 . f_{ctd} \tag{2.19}$$

with

η_1 the bond condition factor equal to 1.0 for good bond conditions and 0.7 otherwise,

η_2 the bar size factor equal to 1.0 for $\phi \leq 32$ mm and $\left(\frac{132 - \phi}{100}\right)$ for $\phi \geq 32$ mm and

f_{ctd} the design tensile strength obtained with equation (2.20), in MPa.

$$f_{ctd} = \alpha_{ct} \left(\frac{f_{ctk,0.05}}{\gamma_c}\right) \tag{2.20}$$

with

$f_{ctk,0.05}$ the 5% fractile value of the characteristic tensile strength*,

α_{ct} a coefficient taking account of long term effects on the tensile strength*,

(recommended $\alpha_{ct} = 1.0$) and

γ_c the partial safety factor for concrete = 1.5.

$*$ values provided in tables or National Annex.

For these equations an equivalent 30 MPa cube compressive strength (28 days), NWC specimen, with good bond conditions and a reinforcing bar smaller than 32 mm, would acclaim to a design bond stress (equation(2.19)) of 1.95 MPa, which proves to be more conservative than the design bond stress of 2.35 MPa from section 2.5.1.

BS EN 1992-1-1 (2004) incorporates a supplementary clause to accommodate design criteria to suit lightweight aggregate concrete (LWAC), which is much more extensive than the one provided in BS 8110-1 (1997). In order to obtain the design bond stress equation (2.19) may be used with the substitution of f_{ctd} with f_{lctd}, given by equation (2.21).

$$f_{lctd} = \frac{f_{lctk,0.05}}{\gamma_c} \tag{2.21}$$

with $f_{lctk,0.05}$ values provided in the supplementary clause on LWAC and obtained with equation (2.22).

$$f_{lctk,0.05} = f_{ctk,0.05}\left(0.4 + \frac{0.6\rho_{LWAC}}{2200}\right) \tag{2.22}$$

where ρ_{LWAC} is the density provided in Table 11.1 in BS EN 1992-1-1 (2004) for LWAC density classes.

Therefore, an equivalent 30 MPa cube compressive (28 days), LWAC specimen, with good bond conditions and a reinforcing bar smaller than 32 mm, a density class of 1.4 ($\rho_{LWAC} = 1450\,\mathrm{kg/m^3}$), will yield a design bond stress of 1.55 MPa, which is also more conservative than the design bond obtained for LWAC in section 2.5.1 of 1.88 MPa.

Therefore, for this case of a single concrete sample, the difference in NWC and LWAC design bond stress is 0.4 MPa which amounts to a 20% decrease in design bond stress when using LWAC.

2.6 Deformed reinforcement

The bond properties depend on a number of influencing factors which include the geometry of the steel bars and particularly the ribs of the deformed bars. Typically the steel geometry is measured by hand since geometry differs between manufacturers (Sistonen et al., 2001; El Zareef and Schlaich, 2008; Desnerck and De Schutter, 2010; Farghal Maree and Hilal Riad, 2014).

In the study of El Zareef and Schlaich (2008) it was found that at the same concrete compressive strength the depth of the ribs, as well as the distance between ribs on the reinforcing material play an important role in the relation between bond stress and slip. In this study the number of ribs per unit length of reinforcing bar was 25% higher for the normal steel than for the GFR, which amounts to a bond stress increase of 20%.

A study on hot dip galvanised steel in concrete introduced a term called the relative rib area, f_r (Sistonen et al., 2001). This term is used to correlate the bond properties and various bars with varying rib geometries. The relative rib area is obtained by equation (2.23).

$$f_r = \frac{\sum S_{PR}}{\pi \cdot \phi \cdot c} \tag{2.23}$$

with

ϕ the nominal bar diameter,

c the rib spacing and

S_{PR} the projective area of ribs (refer to Figure 2.13).

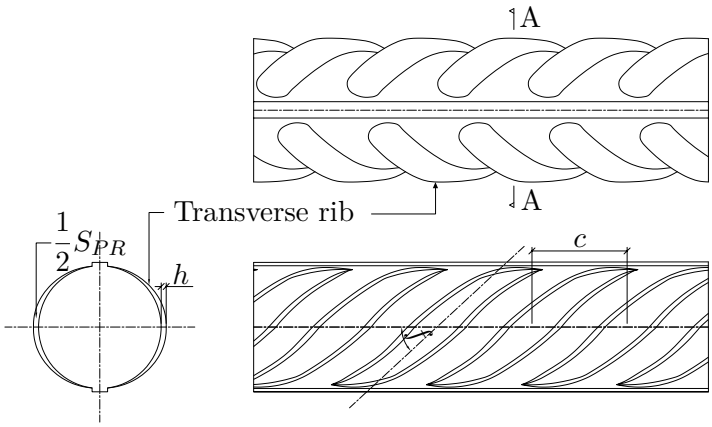

Figure 2.13: Schematic presentation of a deformed steel bar for the parameter definition for the relative rib area according to equation (2.23) *(Sistonen et al., 2001).*

This relative rib area takes account of the height and frequency of the steel reinforcement ribs. The relative rib area increases if either or both the rib height (h) and number of ribs per unit length increases. The study concluded, amongst many findings regarding galvanised steel-concrete bond, that generally with an increase in relative rib area an increase in bond is observed. This is similar to other studies in the field of bond behaviour (Farghal Maree and Hilal Riad, 2014; El Zareef and Schlaich, 2008).

EN 10080 (2005) provides acceptable dimensions for rib height, rib spacing and rib inclination. Table 2.8 lists these acceptable ranges with the rib height and spacing as a function of the nominal bar diameter (ϕ). These parameters are indicated in Figure 2.13.

Table 2.8: Acceptable range for properties of rib geometry (EN 10080, 2005).

h	c	f
0.03 ϕ - 0.15 ϕ	0.4 ϕ - 1.2 ϕ	35° - 75°

-o-O-o-

Chapter 3

Experimental design

The experimental phase is the process of repeating standardized and non-standardised methods and measuring all the required data in order to derive and identify the characteristic bond properties of deformed steel reinforcing in LWFC. Previous studies that compared LWFC and NWC reported differences in strength. In order to quantify the reduced strength of LWFC compared to NWC, various additional strength tests, were done for both concrete types. A notation for all specimens tested, the mixing of the concretes, the determination of a design bond stress and the deformed steel rebar geometry are all reported in this chapter, as well as test and equipment specifications for the determination of the compressive strength, the Young's modulus, the tensile strength, the fracture properties and bond properties with the conventional pull-out and the beam-end test.

3.1 General experimental structure

The bulk experimental work consists of tests that pull deformed steel reinforcement (rebar) from a concrete specimen. The bond properties are derived by the recording of force and slip measurements throughout the test. These tests are standardized for testing normal weight concrete (NWC) and will be used directly or in an adapted form to suit the testing of LWFC. These modifications are required in order to overcome the hitherto lacking engineering properties of LWFC as opposed to NWC. Alongside the LWFC specimens NWC specimens will be tested in order to obtain typical results, which correlate to what is accepted in structural design for bond.

Jones and McCarthy (2005) concluded their study with 1400 kg/m^3 to be the optimum density for structural implementation of LWFC. Casting densities of 1200 kg/m^3, 1400 kg/m^3 and 1600 kg/m^3 were used for all the LWFC tests in this study. A LWFC with a density higher than 1600 kg/m^3 is not considered a lightweight concrete since the foam entrainment percentage is as low as 15% and resembles a mortar. Prediction models show that a LWFC of less than 1200 kg/m^3 will not attain the typically required compressive strength. For these reasons 1200 kg/m^3 and 1600 kg/m^3 were regarded as the casting density boundaries for the mixing of LWFC in this study. Mixing LWFC requires the use of a special mixer. The volume capacity (70 litres) of the mixer for LWFC at the University of Stellenbosch, together with the constraints for preparing and testing of the beam-end (BE) specimens within the restricted laboratory operating hours, were challenging. The BE specimens were approximately 52 litres (including the

3 compression test cubes), which implied that a new mix was required for every specimen.

Batching difficulties were overcome by casting and testing 100 mm concrete cubes for compression strength tests. These tests formed the baseline for comparing mixes, concrete types and bond strengths. The conventional 28-day curing is used as a comparative strength development period. This strength gaining time frame was used to evaluate the various strength and bond characteristics. Kearsley and Wainwright (2001a) stated that the porosity and permeability of concrete is strongly affected by its moisture content and their results have shown changes in permeability of saturated and oven dried specimens. This emphasizes that a specific testing moisture regime be specified when laboratory experiments are done and for this study all tests were conducted at near saturation level, with the exception of the specimens of the BE and the PO tests. All the bond tests were executed at a dryer condition, due to more preparation time that was needed for the larger specimens. Consequently all tests associated with bond characterization were conducted to within 15 hours after removing the specimens from optimal curing conditions and all other test specimens were tested within one hour after removal from the curing tanks. In the tanks, the water temperature is controlled to 22 $\pm$2 Centigrade.

All specimen moulds were designed and constructed from 20 mm thick locally supplied shutterply wood and the contact surfaces were finished with a moisture barrier paint to ensure repetitive use. The moulds were assembled with 8x40 mm screws at a maximum spacing length of 100 mm.

3.2 Specimen notation

All concrete specimens and groups are identified throughout this study with a novel code according to the concrete type, test procedure, bar size (ϕ) and embedded length (l_e). These variables are listed in Table 3.1 with the corresponding code representative.

These codes are then assembled in a specific notation format. For example, the specimen code 12F-B-12-5 indicates a 1200 kg/m^3 LWFC, beam-end specimen with a Y12 bar cast at an embedded length of 5 diameters (in this case 60 mm). At the stage where the average embedded lengths are used, the embedded length code is omitted from the notation. The results of the group of pull-out tests for the 1400 kg/m^3 LWFC, namely for 14F-P-10-3, 14F-P-10-4 and 14F-P-10-5 will be averaged to yield a group result indicated by 14F-P-10.

If a specimen is tested for any of the tensile strength, compressive strength or Young's modulus, the bar type and embedded length will not be included for the obvious absence of rebars during testing. For example, N-T indicates the three NWC specimens tested in the tensile splitting test.

Table 3.1: Notation used to identify specimens and groups of specimens used during this study.

	Description	Code
Concrete type	NWC	N
	1200 kg/m^3 LWFC	12F
	1400 kg/m^3 LWFC	14F
	1600 kg/m^3 LWFC	16F
Test	Modulus of Elasticity	E
	Tensile splitting	T
	Wedge splitting	W
	Pull-out	P
	Beam-end	B
ϕ	Y10	10
	Y12	12
	Y20	20
l_e	3ϕ	3
	4ϕ	4
	5ϕ	5

3.3 Concrete mix design

3.3.1 Cement: PPC CEM II 52.5 N

The cement used throughout the study is Pretoria Portland Cement (Jones, 2015) OPC, CEM II, 52.5N, which is a South African product. The CEM II is a blend of cement clinker with gypsum and limestone as extenders. It contains a very small amount of strength enhancing chemical additive within the mix. Bogue analyses are done on every batch produced by PPC and the average percentage values for this cement production in 2015 is given in Table 3.2.

Table 3.2: PPC's OPC CEM II 52.5N Bogue analysis average results for 2015 production.

C_3S	C_2S	C_3A	C_4AF	Strength enhancing chemical additive
59.4%	19.8%	5.5%	10.6%	4.7%

During production, the cement clinker, gypsum and limestone are inter-ground to create the CEM II composition as given in Table 3.3. The combination of these constituents yields an effective and economic cement with a relative density of 3.14.

Table 3.3: PPC's OPC CEM II 52.5N blend composition by weight.

Clinker	Gypsum	Limestone
88.7%	3.5%	7.8%

3.3.2 Fly-ash

Fly-ash is commonly used as a replacement in concrete mixtures and in LWFC mix designs it is considered a standard mix constituent. It has been shown to have a positive effect on the long term strength of LWFC as well as ensuring a more economic concrete (Kearsley, EP and Mostert, HF, 2005). The fly-ash used during this study is Durapozz, which is distributed by AshResources and procured from Products (2015), which is a category S fly-ash that complies with the physical and chemical requirements as set out by SANS 50450-1 (2011). DuraPozz also has a fine spherical particle shape, which ensures improved workability when blended with cement particles and its pozzolanic reactivity aids the strength gaining process over extended periods of time. The pozzolanic activity in DuraPozz is a result of the SiO_2 that reacts with the calcium hydroxide during the hydration of cement to form cementious compounds. This pozzolanic reaction continues for extended periods and results in higher long-term strength. Incorporating Durapozz as an extender or replacement includes benefits such as improved pumpability, reduced heat of hydration, higher sulphate resistance, reduced risk of alkali-silika reaction, better concrete finish, reduced shrinkage and reduced CO_2 footprint (AshResources, 2011).

The use of fly-ash in LWFC mixes has shown great advantages. LWFC mixes do not have aggregate constituents to fill large volumes and therefore have to make use of the binder material to create volume. Using fly-ash as a replacement, and consequently not using cement as the bulk material, provides a more economic product. Making LWFC without any ash replacement is wasteful and generates other problems such as heat of hydration. During the early stages of this study, a LWFC with zero ash replacement was tested, which resulted in wooden moulds being destroyed by the heat of hydration. Kearsley, EP and Mostert, HF (2005) have shown that the ash content, even so for the cement content as well, does not have a great effect on the strengths obtained, and that it is mainly governed by the porosity. Previous research has shown optimum ash replacement of up to 75% (Kearsley, E.P. and Wainwright, P.J., 2002). For these reasons it was decided to test only with an ash to cement ratio of 1:1, which provided a good ratio for a foamed concrete that can eventually be used in structural applications.

3.3.3 Water demand for fly-ash and cement

Similar to the work done by Kearsley, EP and Mostert, HF (2005), the cement and ash used was tested to determine the water demand for optimum workability, using a flowtable test. The procedure was adapted from the ASTM flowtable test for Hydraulic cement (ASTM C230, 2001). The test comprises of filling a mini-slump cone with the water and solid mix. The cone has a bottom diameter of 100 mm, a top diameter 70 mm and a height of 50 mm. The cone is placed

on the flowtable whereafter the cone is removed to leave a mound of paste. The flowtable is then repeatedly dropped 15 times from a height of 12.7 mm. This action is induced by the turning of a handle, which is an integral part of the mechanical design of the standardized flowtable. The drops induce a spreading of the mixture over the flow table, yielding a relative flow/workability index. By carefully assessing what the water demand is with visual trial and error, Kearsley, EP and Mostert, HF (2005) established that a flow diameter of between 220 mm and 250 mm proved to give the best workability and the correct water demand for use in a LWFC mix. Kearsley, EP and Mostert, HF (2005) used a CEM I cement that yielded a different water demand to the CEM II used in this study. This difference can be attributed to the additions in the CEM II blend, which is not found in the more pure CEM I cement. Figure 3.1 shows the graph with the flow table results as a function of the water to solids ratio. Each data point represents the average result of 3 tests. The intercept of the horizontal line at 220 mm diameter with the two graphs yield the ideal water demand for the cement and ash.

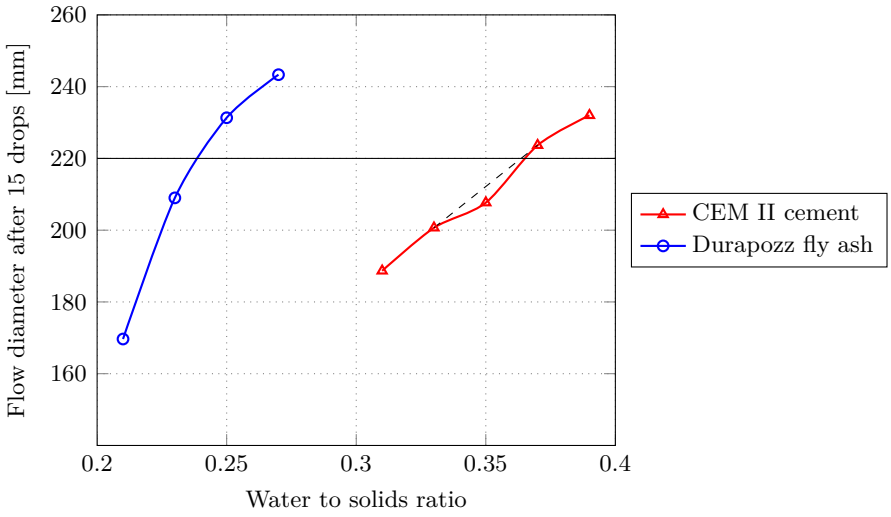

Figure 3.1: Flow table test results for the determination of the cement and ash water demand used in the mix design of LWFC for this study.

Through interpolation the water to solids ratio for the cement is 0.367 and the fly-ash is 0.245, which are in good agreement with the results of Kearsley, EP and Mostert, HF (2005) for CEM I, respectively 0.35 and 0.25. The main exception is that CEM II needs more water to achieve the required workability. This is attributed to the CEM I having a maximum lime replacement criteria of 5%, whereas the CEM II, used in the study, has a limestone composition of 7.8% and gypsum of 3.5%. These fine material additives cause a higher water demand for sufficient workability. The water-cement ratio was rounded up to 0.37 and the water-ash ratio to 0.25.

3.3.4 Lightweight foamed concrete

The design of the LWFC mix is primarily based on previous work by Kearsley, EP and Mostert, HF (2005) and is presented here. Compressive strengths dictates NWC mix designs and can be directly correlated to the ratio between water and cement. The procedure developed for LWFC

includes both strength and density requirements in order to produce an effective lightweight concrete. LWFC is more sensitive to the water demand of constituent materials than typical NWC. For LWFC too much water can cause segregation and hence a variation in density. On the other hand too little water will impede the initial reaction of the cement whereafter the cement starts to withdraw water from the entrained foam, which leads to deterioration of the LWFC in its plastic state.

The process of making a LWFC mix is started by choosing a required target density. Previous studies provide useful mathematical models to predict the compressive strengths for various casting densities of LWFC. Kearsley, EP and Mostert, HF (2005) promote the use of large volumes of fly-ash, but careful attention must be paid to the replacement of fly-ash, its associated water demand and its combined effect on the entire mix development. For this reason the water demand of the fly-ash was obtained as explained in Section 3.3.3.

The mix design contains two variables, namely the cement content and the foam content. Kearsley, EP and Mostert, HF (2005) constructed two equations that form the basis for LWFC mix design and they are given by equations (3.1) and (3.2).

$$\rho_t = x_c + x_c\left(\frac{w}{c}\right) + x_c\left(\frac{a}{c}\right) + x_c\left(\frac{a}{c}\right)\left(\frac{w}{a}\right) + RD_f.V_f \tag{3.1}$$

$$1000 = \frac{x_c}{RD_c} + x_c\left(\frac{w}{c}\right) + \frac{x_c\left(\frac{a}{c}\right)}{RD_a} + x_c\left(\frac{a}{c}\right)\left(\frac{w}{a}\right) + V_f \tag{3.2}$$

with

ρ_t the design target casting density [kg/m^3],

x_c the cement content [kg/m^3],

$\frac{w}{c}$ the water/cement ratio,

$\frac{a}{c}$ the ash/cement ratio,

$\frac{w}{a}$ the water/ash ratio,

V_f the volume of the foam in litres,

RD_f the relative density of the foam,

RD_c the relative density of the cement,

RD_a the relative density of the ash and

The simultaneous solution of equations (3.1) and (3.2) is the recipe for a stable and effective foamed concrete mix with proven accurate implementation and the LWFC mixes designed for the purpose of this study were done accordingly and summarized in Table 3.4. The base mix density, ρ_b, refers to the density of the mixture before the addition of foam.

Table 3.4: LWFC mix compositions used during this study for the various casting densities tested.

Target casting density,ρ_t [kg/m^3]	1200	1400	1600
Base mix density, ρ_b [kg/m^3]	1881	1881	1881
Cement [kg]	447.2	526.7	606.2
Fly-ash [kg]	447.2	526.7	606.2
Water [l]	277.3	326.6	375.9
Foam [l]	377.0	266.3	155.5
a/c	1	1	1
Effective w/c ratio	0.62	0.62	0.62
w/binder	0.31	0.31	0.31

The empirical relation between casting and dry density by oven drying specimens, as obtained by Kearsley, EP and Mostert, HF (2005), which is given by equation (3.3), may not be implemented in this study, because they used other materials. Though it still assisted to estimate and predict typical differences between casting and dry densities.

$$\rho_t = 1.034\rho_{dry} + 101.96 \tag{3.3}$$

with

ρ_{dry} the dry density [kg/m^3].

Table 3.5 indicates the casting densities and the expected dry densities according to the relation provided in equation (3.3).

Table 3.5: Casting densities with the corresponding expected dry densities used during this study.

ρ_t [kg/m^3]	ρ_{dry} [kg/m^3]
1200	1062
1400	1255
1600	1449

3.3.5 Normal weight concrete

Normal weight concrete (NWC) was tested alongside the LWFC specimens as a benchmark to compare the performance of the LWFC. A typical NWC mix, with a target strength of 40 MPa and consequently a water-cement ratio of 0.58, was used. The same cement (as introduced in Section 3.3.1) was used for the NWC and LWFC. Other constituents include 13 mm Greywacke aggregate and fine Malmesbury sand.

Table 3.6 lists the constituent make up of the NWC used during this study.

Table 3.6: Mix constituents of NWC mixed during this study.

Constituents	Mass [kg]	Relative density	Volume [l]
Water	195	1	195
Cement	336.2	3.140	107.1
Aggregate	1000	2.700	370.4
Sand	835.0	2.549	327.6
Total	2366.2		1000

The Malmesbury sand was evaluated by SANAS Soillab who specializes in the testing of road and foundation materials. The screen analysis provided the percentage of material which passes through various sieve sizes. Table 3.7 lists the breakdown of the sieve analysis.

Table 3.7: Sieve analysis results as obtained by SANAS Soillab for fine Malmesbury sand used for the NWC mixes.

Sieve size [mm]	% sand passing
4.75	100
2	99
0.425	31
0.075	5

3.4 General information for bond tests

This section describes a typical specimen loaded in a bond characterizing test, like the pull-out (PO) and beam-end (BE) tests introduced in Section 3.11 and 3.12 respectively, in order to familiarize the reader with terms used during the following sections. Figure 3.2 shows a schematic representation of a bond test specimen with an embedded test bar.

The threaded rebar fixed at the top with a washer and nut connection to the loading frame of the testing machine used. This side of the specimen is termed the loaded-end. The opposite term is referred to as the free-end. The blue arrow indicates the relative downwards movement of the specimen as a result of an applied force and eventual bond loss. The bar is bonded over a certain length with debonding methods used to force the bonded region to a controllable length. This is done to vary the embedded length.

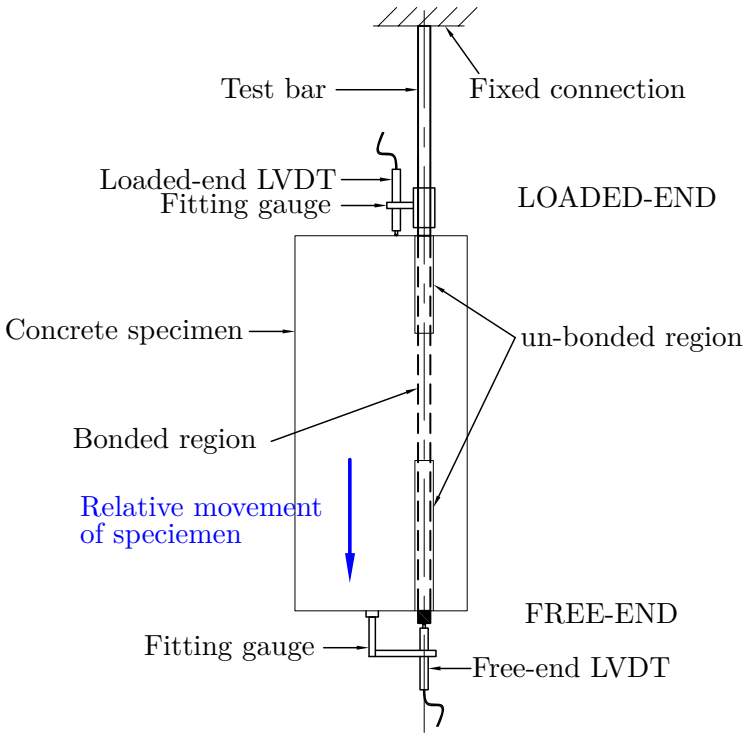

Figure 3.2: A schematic representation of a concrete specimen during a bond test procedure indicating the terms used throughout this study. The blue arrow indicate the absolute displacement of the specimen during testing.

A Linear Variable Displacement Transducer (LVDT) is a measuring device that relies on electromagnetic coupling to convey a physical recorded displacement to an induced voltage. This voltage potential is calibrated to a displacement, which is used with test machinery to accurately record displacements. Two LVDT's are used to measure the slip of the bar at the loaded-end and free-end. The free-end LVDT is fitted to the concrete underside with a specially manufactured gauge and measures the free-slip, which is used in this study to obtain a design bond stress value reading. The loaded-end LVDT is also fitted with a special gauge to the test bar, measuring the loaded-end slip, which is a summation of the elongation of the bar and the free-slip. The loaded-end slip always precedes the free-end slip, because of the elongation of the test bar.

These terms and definitions will be used for both tests introduced later in this chapter.

3.5 Design bond stress and design point

The use of a design bond stress is found throughout engineering standards (SABS 0100-1, 2000; BS EN 1992-1-1, 2004), though, the manner in which these design bond values were obtained, could not be traced in literature studies. Table 3.8 summarises the design bond stresses specified in both SABS 0100-1 (2000) and BS EN 1992-1-1 (2004). These values correlate to a bond stress ratio of 0.5, which provides the relative proportionality between the design bond stress, σ_d, and the square root of f_{cu}. Using this inherent proportionality of NWC in the evaluation of LWFC is not recommended, and a unique proportionality must be established when considering a new

building material.

The use of this normalizing, $\frac{\sigma_d}{\sqrt{f_{cu}}}$, as a comparative tool is found in multiple reports on the bond behaviour of NWC compared to a lightweight, reduced strength concrete. The relation as provided by BS 8110-1 (1997) is used for the design bond stress of NWC and it may not be assumed that a reduced strength concrete will yield the same expression. For this study the measured design bond stresses are not normalized by any function of f_{cu} and the design stresses are compared directly.

Table 3.8: Design bond stresses (σ_d) specified in design standards, classified according to the mean cube compressive strength (f_{cu}). The method for obtaining the empirical data corresponding to the relation between σ_d and f_{cu} is not known.

	f_{cu} [MPa]	σ_d [MPa]
SABS*	20	2.20
	25	2.50
	30	2.90
	40	3.40
BSEN**	20	1.95
	25	2.25
	30	2.70
	45	3.30
*SABS 0100-1 (2000) §4.11.6.2		
**BS EN 1992-1-1 (2004) §8.4.2		

Leonhardt (1977) suggests to read off σ_d at a certain slip value; in this case 0.1 mm. This implies that σ_d is derived as the force in the bar divided by the bond contact area when the free-end of the bar has displaced (slipped) 0.1 mm during a bond test. This design slip value is correlated to allowable crack widths in reinforced concrete structures, because the relative movement of rebar in concrete induces cracks. It has been reported that these cracks have shown to be proportional to the absolute slip of an embedded bar. Throughout this study the design bond stress, σ_d, will be taken at the free-end slip value of 0.1 mm. It has to be noted that the method used in this study might be different from the methods used to develop relations such as those found in SABS 0100-1 (2000) and BS EN 1992-1-1 (2004). It does however provide a sound solution to obtain a design point within a bonding test, correlated to a physical occurrence, which can effectively be used in comparisons and prediction models.

3.6 Steel Reinforcing

Visits to various steel producers and distributors nearby Stellenbosch showed that the geometry of steel rebar in South Africa varies considerably. In spite of the variation, every batch was in line with what is specified in SABS 920 (2011), §3.9 (a) & (b). The steel reinforcing used throughout this study were from the same batch delivered from a single supplier, and sponsored by John Hulse from Hulse Reinforcing (Hulse, J., 2015). Hulse Reinforcing is registered as a supplier at SARCEA, the South African Reinforced Concrete Engineers' Association (Thomas, Jeffery J., 2015). In correspondence with Jeffery Thomas, the CEO of SARCEA, the author was ensured that all registered suppliers supply rebar manufactured according to SABS 920 (2011).

The steel used in this study was carefully selected from a batch produced by SA Metal in Cape town. The SA Metal rebar ribs are clearly identified by its round shape, as opposed to defined edges. The rebar used in this study are Y10, Y12 and Y20, where the Y prefix indicates a high yield characteristic tensile strength of 450 MPa and the number indicates the nominal bar diameter (ϕ). Additional secondary steel was used for stirrups, which are plain mild steel bars of diameter 8 mm (R8) with average yield strength of 250 MPa. The R prefix indicates a mild steel.

The Y10 and Y12 rebar are distributed in rolls rather than straight stock lengths. These rolls are then stacked into a machine that unwinds the rolls and cuts and bends required shapes automatically. Upon close scrutiny of this process and the finished product, it was found that the ribs on these rebar are somewhat damaged during the process. Accounting for these minor deformations for the purpose of the bond investigation, seemed not only impractical but also unnecessary, because these diameter sizes of steel are all rolled in similar manner throughout the country and installed with the mentioned minor damages. Whether these damages have a measurable effect on the bond behaviour could be the basis of another study, but will not be investigated during this study. However, careful inspection and selection were done to ensure the exclusion of parts with out of the ordinary damage to the steel surface and ribs. No bars were rejected according to these conditions.

The deformations on deformed steel rebar are obtained by passing steel rods through a series of rollers which then press the rib geometry into the steel. These rollers (moulds) differ between manufacturers. The photo in Figure 3.3 shows 3 different Y20 bars obtained from 3 different suppliers, with the differences in the rebar geometries clearly visible. The bar at the bottom is a Scaw Metal product, easily identified by the very clear and angular ribs. The middle bar is a SA Metal product and is identified by a more rounded rib shape. The top bar could not be identified, but it is believed to be an imported bar. This emphasizes the importance of using the same manufacturer and, if possible, the same batch since these rollers might wear off and produce varying rebar geometries.

Figure 3.3: Three Y20 bars from 3 different manufacturers supplied in South Africa. The one at the bottom is a product from Scaw Metal, the middle one from SA Metal en the supplier of the top one could not be determined.

Measurements were done on the rebar used, in order to identify the rib geometry and produced the averaged values for the parameters in Figure 3.4, which are listed in Table 3.9. The measurements are based on an average of 6 readings on various positions along the rebar. The maximum coefficient of variation seen for these readings were 0.021.

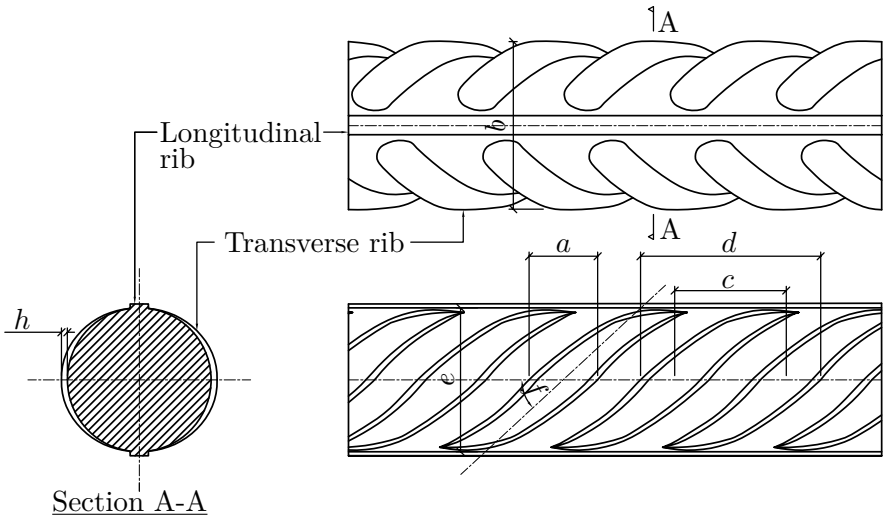

Figure 3.4: A drawing of a generic rebar with dimensions typically used to identify the rib and rebar geometry, which is provided for the various diameter bars used in this study, in Table 3.9.

Table 3.9: Rebar dimensions from measurements corresponding to Figure 3.4

Property	Y20	Y12	Y10
a - rib width [mm]	6.14	3.29	2.38
b - outside bar diameter [mm]	22.48	12.63	10.24
c - center rib spacing [mm]	15.87	6.77	6.42
d - outer rib spacing [mm]	22.01	10.07	8.80
e - inside bar diameter [mm]	18.28	11.61	9.60
f - rib angle [degrees]	42.13	56.49	58.52
h - rib height [mm]	2.10	0.51	0.32
Ribs per meter length	63	148	156
f_r - Relative rib area	7.600×10^{-3}	1.654×10^{-3}	0.831×10^{-3}

In addition the rebars were photographed and drawn into a computer aided drawing programme (Autocad, 2014) in order to obtain scales for accurate geometric dimensioning and to check the accuracy of the measurements done by hand. This method concluded that the accuracy of physical measurements are sufficient for the geometry classification of rebar.

3.7 Compressive strength tests

The concrete compressive strength was measured with 3 specimens for every mix made and is used to overcome batching difficulties and compare various other properties of the concretes tested. Usually the compressive strength plays an important comparative role in studies of cement based materials. The ability of concrete to handle great compressive stresses is what makes it such a useful and widely used structural material. The compressive strength classification and time dependant gain of strength is therefore of importance when classifying a new material. Compressive strength models for LWFC have been published, which accurately predict the compressive strength at varying ages, with the density and material mass ratios being the variables.

The compressive tests were done according to the specifications set out by SABS 5863 (2000). The test was performed using a 350 ton Contest material testing machine. Concrete 100 mm cubes were crushed between the actuator and the frame at a constant load rate of 0.3 $\pm$ 0.1 MPa/s. These tests were conducted at 180 kN/min. A total of 3 specimens per group are sequentially loaded until failure and the peak values are recorded. The average peak value is then accepted as the mean concrete compressive force. This force is then converted to a mean concrete compressive strength, f_{cu}, by dividing the peak average force by the contact area of the loaded specimen face, given by equation (3.4).

$$f_{cu} = \frac{F}{A} \tag{3.4}$$

With f_{cu} in MPa, F the peak force in Newtons and A the contact area in mm^2.

3.8 Young's modulus tests

The Young's modulus tests is conducted under the specifications prescribed in the American Standard, ASTM C469 (2002). The test method provides the means to obtain a stress-strain gradient for hardened concrete at a specific age. The modulus of elasticity obtained from these tests apply when the material is subjected to within a selected customary working stress range. In this case it is specified to be up to 40% of the ultimate concrete cube compressive stress.

The 350 ton Contest material testing machine was used for testing cylindrical shaped specimens of length 200 mm and diameter 100 mm. Such a loaded specimen is shown in Figure 3.5. Typical Young's modulus testing frames are fitted to the cylindrical specimen which hold 3 LVDT's and provide a platform at 70 mm gauge length to take displacement readings. When the specimen is loaded the cylinder is shortened and the LVDT measurement, divided by the gauge length, provides an indication of the strain as the test progresses. A 250 kN external load cell was used to obtain an accurate compressive force reading during the test.

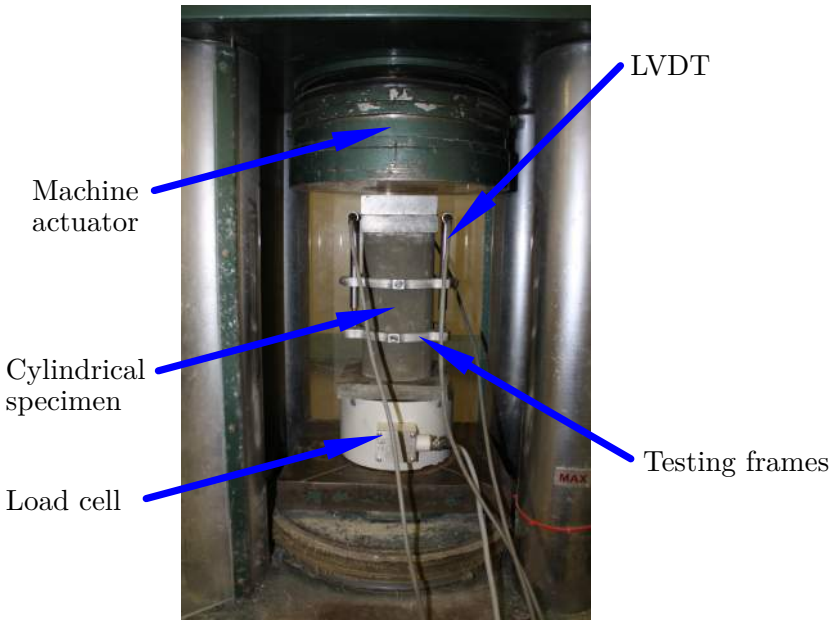

Figure 3.5: The Young's modulus test setup with a loaded specimen, fitted with the testing frame that hold 3 LVDT's to measure the shortening of the specimen over a 70 mm gauge length.

The specimen has to be loaded up to the 40% stress limit and unloaded at least 3 times and no data recording is done during the first loading sequence. The first loading allows the gauges to seat properly onto the specimen and, if any shifting or loosening of the gauges occurred, it can be rectified before applying the loading used for evaluation. The loading commences up to 40% of

the ultimate cube compressive strength, where after the load is removed. This cycle is repeated for a second round and the average of 3 LVDT's is taken for both loadings and averaged. The readings at 33% and 40% of the ultimate strength is used to obtain the stress-strain gradient providing the Young's modulus, E_c. Equation (3.5) is used to obtain the Young's modulus.

$$E_c = \frac{\sigma_1 - \sigma_0}{\epsilon_1 - \epsilon_0} \tag{3.5}$$

with

E_c the elastic modulus [GPa],

σ_1 the stress corresponding to 40% of the ultimate strength, in MPa,

σ_0 the stress corresponding to 33% of the ultimate strength, in MPa,

ϵ_1 the strain corresponding to 40% of the ultimate strength and

ϵ_0 the strain corresponding to 33% of the ultimate strength.

The loading was applied continuously and without any shock, with a controlled loading rate of 200 kPa/s which, for a 100 mm diameter cylinder, yields a rate of 94 kN/min.

3.9 Indirect tensile splitting strength tests

Previous studies have shown that the tensile strength of LWFC is much less than the NWC equivalent. This reduction in tensile resistance will induce cracking at an earlier stage and at greater intensity and frequency. For this reason the tensile splitting strength of the concrete range was obtained according to SABS 6253 (2000). This method is known as an indirect tensile test since the tension is not applied directly, but rather a direct compression force which induces a tension force. The direct tests usually yield conservative strength values compared to the indirect tests. For the purpose of this study the indirect tensile test provided a quick method for relative tensile strengths.

The tensile splitting test is done using a Zwick Z250 material testing machine with a capacity of 250 kN. Figure 3.6 shows a concrete specimen assembled in the tensile splitting strength test setup, with the appropriate loading plates and wooden loading strips.

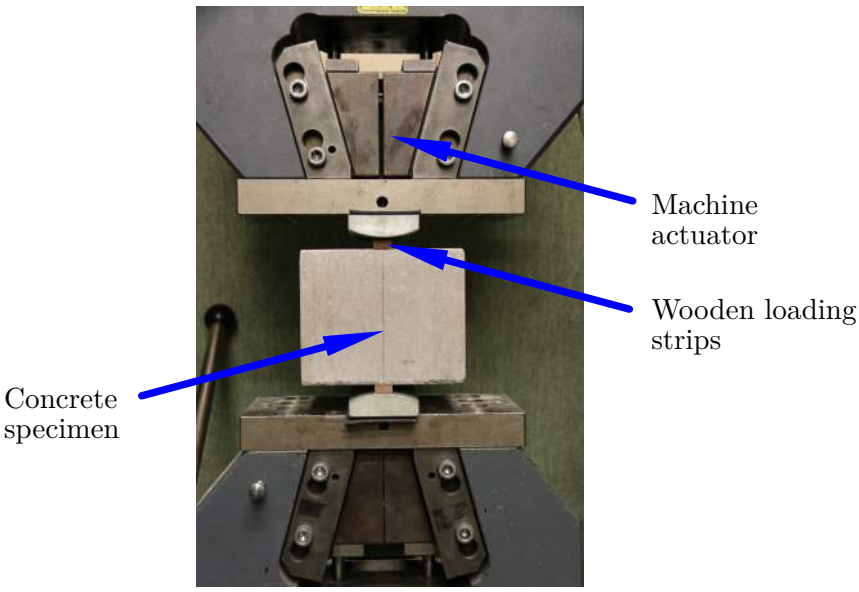

Figure 3.6: The indirect tensile splitting test.

The average ultimate force of 3 specimens per group is used to determine the mean splitting stress at failure with equation (3.6).

$$f_t = \frac{2F}{\pi . A_c} \tag{3.6}$$

With f_t the mean tensile splitting strength in MPa, F the maximum load at failure in Newtons, A_c the crack plane area in mm^2.

The machine applies the compressive force to the top op the cube specimen and indirectly forces the cube to split open. A LWFC specimen with a tensile split is shown in Figure 3.7.

Figure 3.7: Indirect tensile splitting test specimen after failure.

SABS 6253 (2000) makes provision for various prismatic shaped concrete specimens. 100 mm cube specimens were used to conduct the tensile test. A constant pressure rate of 0.3 ± 0.1 MPa/s is prescribed during testing until a peak failure force is reached. The standard provides a formula for calculating the rate of loading. This equation is given by equation (3.7), with ROL being the rate of loading in Newtons per second, l_1 the length of the specimen in mm and l_2 the cross sectional dimension in mm.

$$ROL = \frac{0.03 \cdot \pi}{2 \cdot l_1 \cdot l_2} \tag{3.7}$$

However the author was not comfortable to use this equation to obtain the required loading rate, because of an indiscrepancy of units. It was decided to rather control the test with a displacement of 1 mm/min which allows the tensile force to gradually increase at a steady rate.

3.10 Wedge splitting fracture tests

Brühwiler and Wittmann (1990) introduced a new method for determining the fracture energy of concrete materials with the use of a displacement controlled, stable, fracture test. This procedure is incorporated into this study to address the cracking susceptibility of the LWFC and provide an indication of the required energy to split a specimen along a predetermined crack surface.

The test comprises of subjecting a cube specimen to a bending moment and splitting the cube vertically. This splitting state is obtained with a setup of wedges bearing onto rollers, which in turn forces a crack to open.

The 100x100x100 mm specimen is notched at the top (30 mm wide and 20 mm deep) as indicated in Figure 3.8. A saw-cut is then made, 30 mm deep along the notched face, which suits as a crack initiator and to force a specific fracture area through which the crack has to develop.

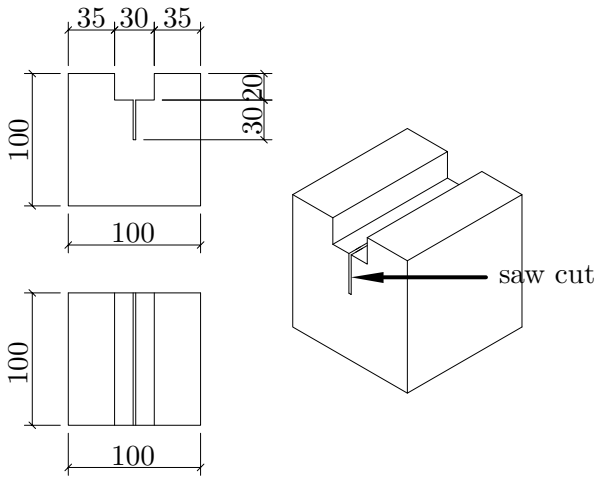

Figure 3.8: Wedge splitting test specimen with indicated dimensions and saw-cut length to force a crack path and a predetermined crack area.

The test is assembled as depicted in the schematic drawings in Figure 3.9 and the actual setup used is shown in Figures 3.10 and 3.11.

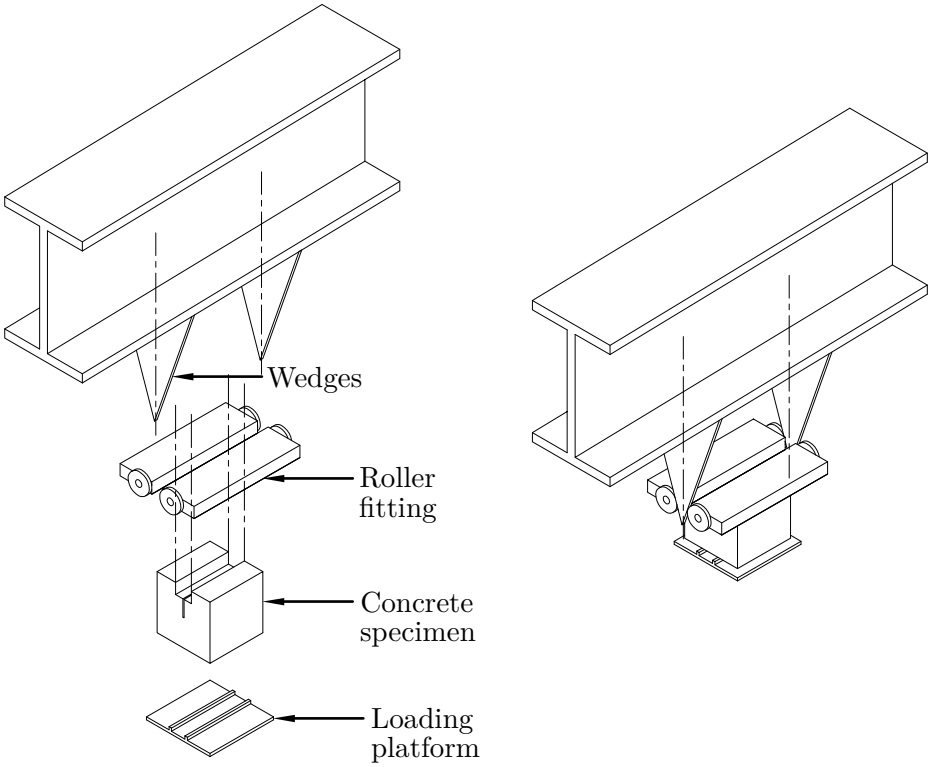

Figure 3.9: Schematic presentation of the wedge splitting fracture test setup. On the left side the exploded setup and on the right the assembled setup.

Figure 3.10: The wedge splitting setup with the specimen and wedges.

Figure 3.11: The wedge splitting setup with the added roller fitting.

The specimen is carefully aligned onto a loading platform, which has two linear supports, 50 mm apart. A roller fitting fits onto the notched edge, which then, once the wedge bears onto the two rollers, provides a lateral force leading to a crack opening. The wedges are fitted to a testing machine capable of applying the force, but also the desired crack opening control displacement.

Once the wedges start to bear on the rollers, the forces represented in Figure 3.12 occur during the test procedure. F_v is the vertical force applied by the machine actuator, F_h is the horizontal crack opening force and α_w is the wedge angle. A wedge angle of 14° was used.

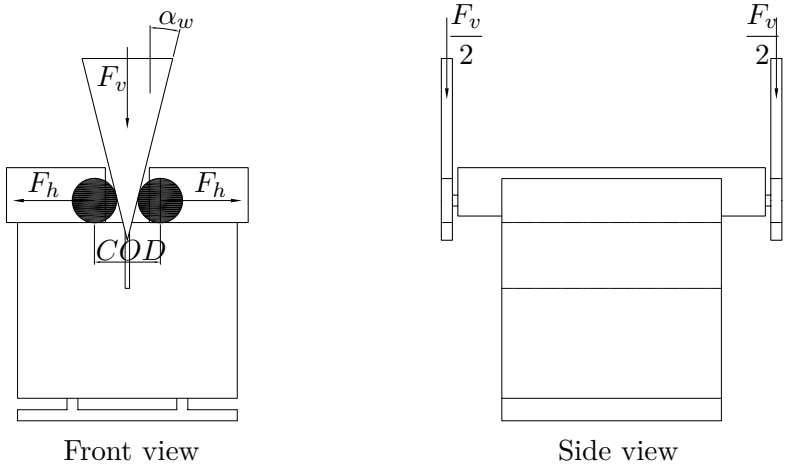

Figure 3.12: Front and side view of the wedge splitting setup with indicated forces present and crack opening displacement (COD).

The crack opening displacement (COD) is the indicator of crack opening at the saw-cut and serves as a controlling displacement for the test procedure. The COD, and therefore the actuator control, is measured and controlled with two LVDT's fitted on either side of the specimen. The LVDT placement is chosen to ensure that a COD reading occurs at a very early stage during the test procedure, even before a crack starts to develop at the bottom of the saw-cut. Figure 3.13 shows the LVDT's fitted at the start of the saw-cut.

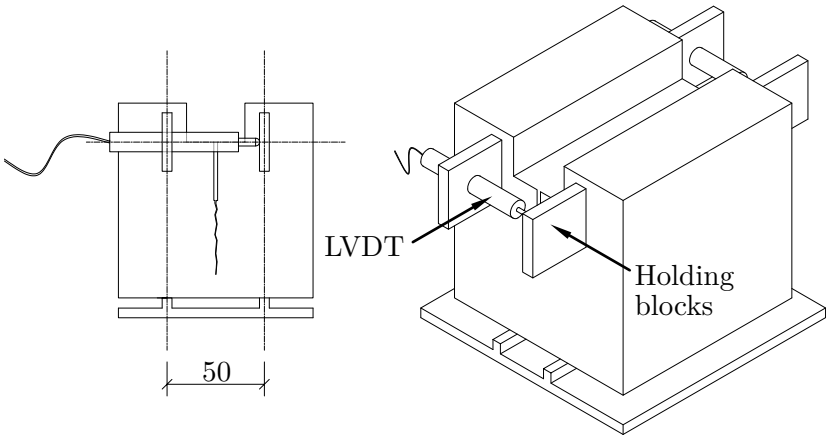

Figure 3.13: Wedge splitting test specimen with indication of LVDT positioning at the start of the saw cut.

The horizontal forces trigger the opening of the crack, where after the machine control the test at a crack opening rate of 0.003 mm/s, leading to stable fracture. This rate was found through trial and error. The control of the machine was fine tuned with specific software yielding a proportional factor of 50 dB, a derivative operator and lag term of zero and an integrator factor of 1. For an explanation of these factors and the setup of displacement control tests refer to Appendix A in which the procedure for the setup of the control is explained for the beam-end tests of Section 3.12.

The horizontal splitting force is obtained with equation (3.8).

$$F_h = \frac{F_v}{2.tan(\alpha_w)} \tag{3.8}$$

The energy associated with the splitting of the cube is given by the area under the F_h-COD graph. The specific fracture energy, G_f, is then found by dividing this integral by the projected fracture area, which is the plane through which the specimen cracks. The characteristic length, l_c, is a factor derived from other material properties (including G_f) and provide a value that indicates the brittleness of the material. The characteristic length is found with equation (3.9).

$$l_c = \frac{E_c.G_f}{f_t^2} \tag{3.9}$$

with E_c the Young's modulus in MPa, G_f the specific fracture energy in N/mm and f_t the cube tensile splitting stress in MPa.

The test is considered a stable fracture if no sudden load drop is recorded. The stable fracture yields a load-deformation reaching a peak followed by a descending part without sudden loss of stiffness. With proper control, even brittle materials can exhibit stable fracture, however Brühwiler and Wittmann (1990) warned that completely brittle materials cannot yield stable fracture. The aim of this test is to quantify the difference in crack formation of LWFC with the proportional gain of brittleness with increased density.

A LWFC wedge splitting specimen is shown in Figure 3.14 to show the vertical crack path after testing.

Figure 3.14: A LWFC specimen with a vertical crack after a wedge splitting test.

3.11 Pull-out test

3.11.1 Introduction

The pull-out (PO) test comprises of a cube specimen with an embedded steel bar, loaded in such a manner to pull the bar from the concrete by applying a compressive load on the concrete face where the bar protrudes. Careful measurements during this test provide data used for evaluation of the bond performance of concrete specimens.

The PO test is done according to specifications set out by ASTM C234, however, the standard has, for reasons unknown, been withdrawn from the ASTM database in 2000. The author consulted a member of the ASTM committee responsible for these test specifications, but no clear reason was provided as to why this standard has been removed. Usually, once a standard is withdrawn or altered, a description is left on the document itself. Scott Orthey (2015) stated that ASTM C234 had no comment pointing to the removal and he speculated that it had been withdrawn due to inactivity. Even with this in mind, this test still suffices as a suitable measure for comparing bond properties between concrete types. For this reason ASTM C234 is applied in this study and the specifications and procedure are obtained from what is found and reported in previous studies.

The PO test variables include concrete type, bar diameter and embedded length. The concrete types are the NWC, introduced in Section 3.3.5, and the three LWFC, introduced in section 3.3.4. The rebars tested are Y10, Y12 and Y20. The rebar properties are provided in Section 3.6. The embedded lengths were taken as 3ϕ, 4ϕ and 5ϕ, with ϕ the nominal bar diameter.

Refer to Section 3.4 for information and terms used for bonding tests, like the PO test.

3.11.2 Pull-out specimens

The PO specimens are 150 mm concrete cubes with an embedded bar protruding out each end, as shown in Figure 3.15. Note that the loaded-end is indicated at the side which the bar is threaded and fixed to the testing machine (where it is effectively loaded). The free-end is the opposite side where the bar only protrudes 20 mm in order to provide a face on which a slip measurement can be recorded. A specific length from the loaded-end of the bar is de-bonded, using rubber and tape bound around the bar. This is done to ensure the compression from the actuator on the top concrete face does not influence the bond stresses and also enables accurate testing of a specific embedded length.

The position at which the LVDT measures the bar slip is termed the free-end of the embedded bar. At this position the slip is not influenced by elongation of the rebar. The loaded-end slip measurement yields the sum of the elongation of the bar and the free-end slip.

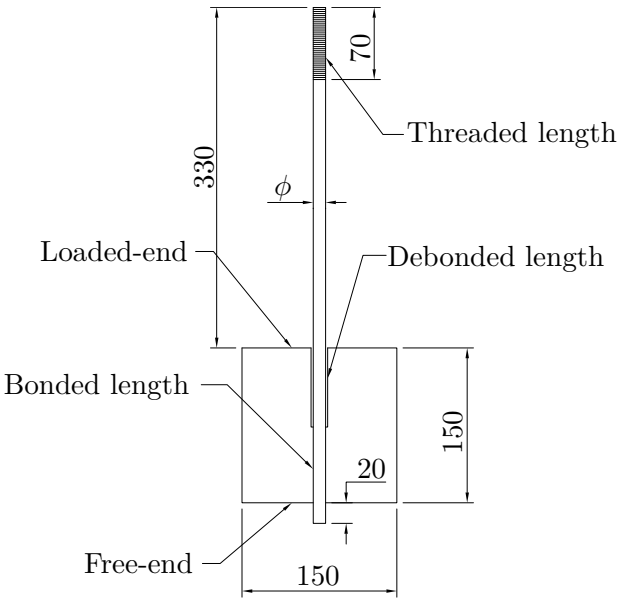

Figure 3.15: Pull-out specimen dimensions and specifications for embedded rebar.

The study by Farghal Maree and Hilal Riad (2014) suggests that ASTM C234 indicated that a bonded length of 5ϕ be used, although it is common in studies to test various embedded lengths. For this study 3 embedded lengths are tested. It is common knowledge that a shorter embedded length yields pull-out failure more readily, whilst a longer embedded length allows for greater build up of concrete stresses and growth of secondary cracks which eventually lead to splitting failure in most cases. It was therefore decided that a range of embedded lengths would yield a better indication of the bond properties and failure modes, especially with a relatively new material such as LWFC. In order to determine these bonded lengths one has to consider the load capacity of the bars and their connections. For a too long embedded length the pull-out/splitting force might overcome the actual capacity of the rebar, or in this case, the connection to the testing machine. The embedded length boundary was therefore determined through published lightweight concrete bond strengths, which resulted in an upper boundary of 5ϕ. Consequently the embedded lengths were chosen as 5ϕ, 3ϕ and 4ϕ.

The specimens were cast in constructed wooden moulds, shown in Figure 3.16, with the de-moulded specimen shown in Figure 3.17.

Figure 3.16: Wooden moulds manufactured for the PO tests.

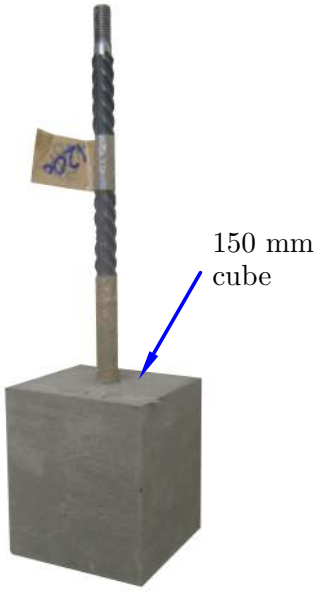

Figure 3.17: PO specimen with Y20 bar.

3.11.3 Testing machine and setup

Figure 3.18 and Figure 3.19 show two different views of the test setup, using a Zwick Z250 material testing machine with a capacity of 250 kN. The bottom clamp of the testing machine is removed to leave a 65 mm diameter hole for the steel bar to pass through. The top end of the rebar is threaded to ensure a secure connection which allows for minimal slippage. The Y20 rebar was threaded to accommodate a M18 nut, the Y12 a M12 nut and the Y10 a M10 nut. This has to be taken into account when designing these tests since this is the part of the bar which has the least amount of cross sectional area to handle the tensile stresses and therefore the most probable failure point. For example the ultimate force for the Y20 bars is estimated by using a diameter of 16 mm (the nominal diameter minus the threaded reduction and the thread depth) rather than 20 mm. The bar is fixed to the top clamp passing through a 30 mm diameter hole and a 20 mm plate with washers and a nut. This connection is seen in Figure 3.20, assembled with a Y10 bar.

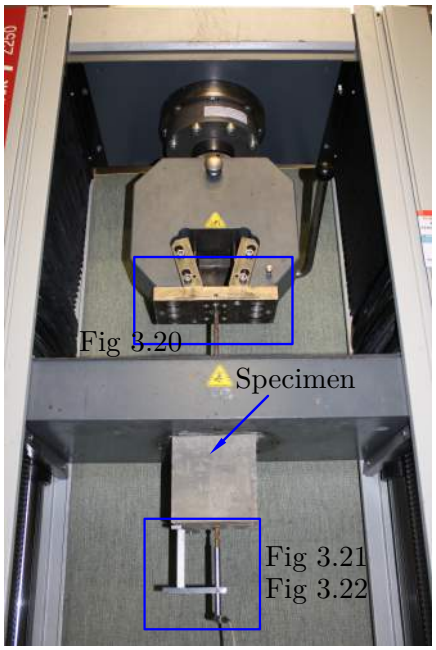

Figure 3.18: A view of the PO test setup showing the testing machine bearing on the top concrete face and indirectly applying a load to the fixed rebar.

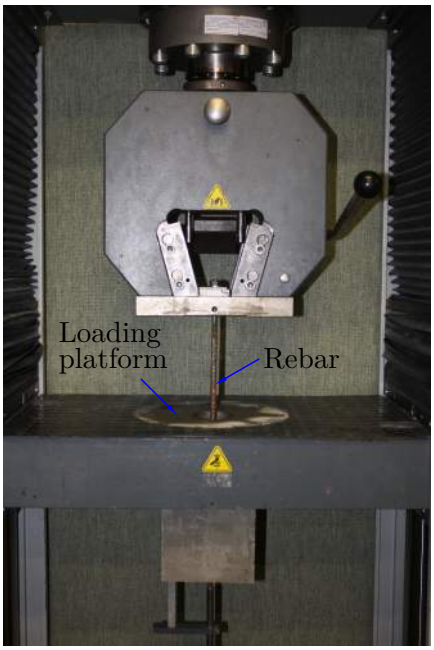

Figure 3.19: Another view of the PO test setup which shows the bar passing through the loading platform and fixed to the machine frame.

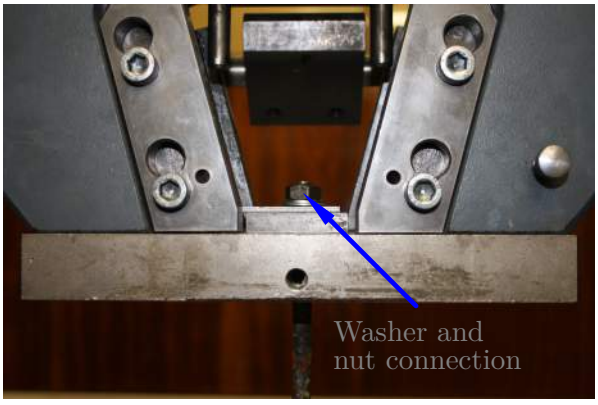

Figure 3.20: The fixed rebar connection in the PO test setup for a Y10 bar. This no-slip connection was obtained by threading the rebar and fixing through the machine frame with a washer and nut.

A specially designed LVDT gauge is fitted to the underside of the PO specimen; positioning the LVDT over the free-end of the rebar. Figure 3.21 indicates the fixing and positioning of the LVDT to the concrete. The gauge connection is done by drilling a 8 mm hole in the concrete, inserting a wall-plug and securing the device with a 8x40 mm screw. Care was taken to drill the hole in a corner to not disrupt any paths of least resistance, should splitting cracks form. The LVDT has a stroke length of 10 mm and is positioned to take a reading in a slot which is drilled on the free-end of the rebar during preparation. This ensures that the LDVT will not slip off the rebar during testing. Figure 3.22 shows straps used to catch the specimen

should splitting failure occur. Two straps (orange and blue) are taken around the actuator platform to move with the specimen during testing and prevent the specimen from falling to the ground. An additional strap (black) was fixed around the specimen to keep the specimen together after splitting failure occurs. It was ensured that all the straps were not taught and therefore preventing any indirect confinement to the concrete. These straps only come into effect once the specimen was completely split and all test resistance was dissipated. This system of straps proved to be very useful on multiple occasions and prevented damage to the LVDT and machine.

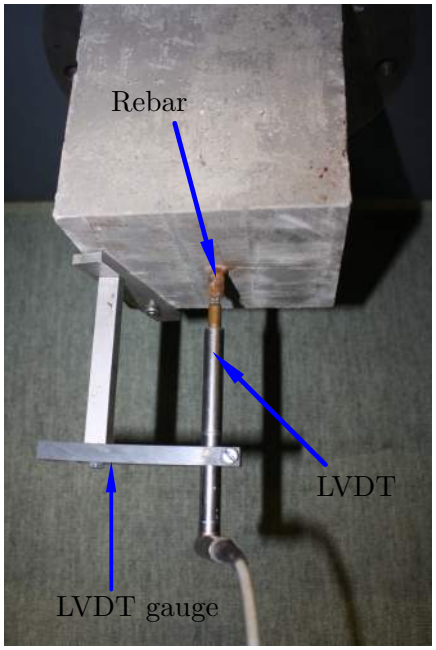

Figure 3.21: Free-end LVDT positioning gauge.

Figure 3.22: Straps used to secure the specimen after splitting failure without disrupting the bond as a result of indirect confinement.

3.11.4 Loading rate

Previous studies that incorporated the PO test, reported using different loading rates, but many did not report on the loading rate used. Also, no study documented on where, or what displacement was used as the controlling displacement. El Zareef and Schlaich (2008) completed the PO tests using a displacement controlled action at 0.1 mm/s. This loading rate is used for this study and proved to be sufficient to obtain the desired force envelope for both NWC and LWFC. The displacement control used in this setup is the loaded-end slip displacement (machine actuator platform displacement reading), taken at the loaded-end of the specimen (refer to Figure 3.15). The machine used for this test forced this loaded-end slip control since the actuator of the machine presses against this face. This controlling regime is repeated for the beam-end tests introduced, and explained, in Section 3.12.

3.12 Beam-end tests

3.12.1 Introduction

The beam-end (BE) test is also used in this study as another procedure to obtain the bond behaviour of a deformed steel bar in LWFC and NWC. The BE tests are conducted according to the specifications set out by ASTM A944-10 (2002) and it comprises of a typical structural beam-sized concrete specimen into which a steel reinforcing bar is cast and loaded at an eccentricity to break the bond interface and pull the bar free. An advantage of the BE test is better simulation of the concrete-steel bond in a structural member i.e. a member subjected to bending moments and shear forces. The disadvantages of the BE test include laborious preparation work and large, heavy specimens.

Only one case was found in literature that reported the successful implementation of the BE test (Farghal Maree and Hilal Riad, 2014) although it comes highly recommended by ACI 318-11 (2011) since it more accurately simulates the steel-concrete stresses present during loading of a structural element, as opposed to what is tested in the PO tests. The loading arrangement of the BE test ensures tensile stress within the concrete adjacent to the embedded bar. The complete loading scheme is considered in Section 3.12.4.

The BE test variables include the type of concrete (NWC and LWFC mixed at 1200 kg/m^3, 1400 kg/m^3 and 1600 kg/m^3) and the rebars (Y12 and Y20). The embedded length is not varied as is done for the PO tests in Section 3.11. The size of the BE specimens dictated that an embedded length less than 5ϕ would render the specimen highly susceptible to damage during the preparation and installation. Similar to what is explained in Section 3.11.2, the design embedded length is limited to 5ϕ, to ensure a safe test.

Refer to Section 3.4 for information and terms used for bonding tests, like the BE test.

3.12.2 Beam-end specimen

The BE specimens are beam ends with the test bar in the tensile region of the flexural element. The specimen is loaded and supported in such a manner to simulate the stresses present within the end section of a beam. Figure 3.23 shows the BE specimen design used for this study. The positioning of the secondary stirrups (R8 bars) is required to ensure the beam does not fail in shear and enable the concrete to transmit the force from the compression area (the machine compression action discussed later) through the concrete matrix to the bonded region at the steel-concrete interface. This has to be done without supplying the test bar with any additional confinement and therefore the stirrups are placed perpendicular to the test bar. Additional Y10 bars, which are entirely embedded, are placed alongside the test bar to ensure the effective distribution of the bending moments through the specimen and to the section at which the embedded length on the test bar occurs. These test bars are threaded to create a fixed washer and nut connection to the loading frame of the testing machine, which will be introduced later.

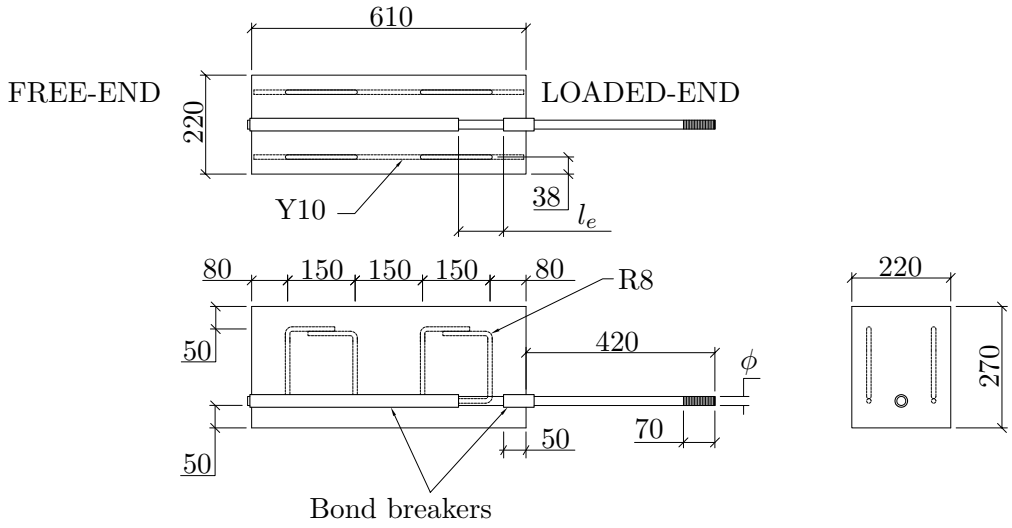

Figure 3.23: The top, side and front views of the beam-end specimen design used for this study, showing the bonded region, reinforcement and dimensions.

The BE specimen used in Figure 3.23 was eventually altered from what is standardized. The specifications for the BE specimen from (ASTM A944-10, 2002) specify that the embedded length be provided from the loaded-end after which a bond breaker will only be installed 115 mm towards the free-end. This implies a fully bonded region after the bond breaker. This arrangement will influence the free-end LVDT slip reading, which for the methodology of this study is considered an important measurement (refer to Section 3.4 for info and terms used during bond tests). The specimen used in this study and seen in Figure 3.23, provides a bonded region only at the intended embedded length (l_e) and nowhere else in the specimen. This alteration was also implemented by Farghal Maree and Hilal Riad (2014). However, they placed the embedded length next to the bearing area of a lateral support (from the loading setup in Section 3.12.3) on the specimen. It is thought that this pressure and stresses will influence the measured bond properties if the embedded length were to be provided in that vicinity. Also, this region is at the free-end of the specimen where there is minimal bending moment. For this study the BE embedded length is provided 50 mm from the loaded-end face, which takes it away from the lateral strut bearing position and into the bonding moment region to simulate bond in a structural member.

The embedded length is offset by 50 mm from the loaded-end and is chosen as a result of the work done by Soltani et al. (2003), in which the curvature influencing zone is explained. This region, at the loaded end of a embedded bar and next to a cracked region, is crushed due to the flexural action induced on a beam (structural member). To allow for this crushing region to not influence the embedded length an offset from the loaded-end specimen face (simulated to effectively be a crack) of 50 mm is provided. Figure 3.24 shows the curvature influencing zone, L_c, adapted from Soltani et al. (2003) showing the crushing of concrete adjacent to a cracked region as a result of loading.

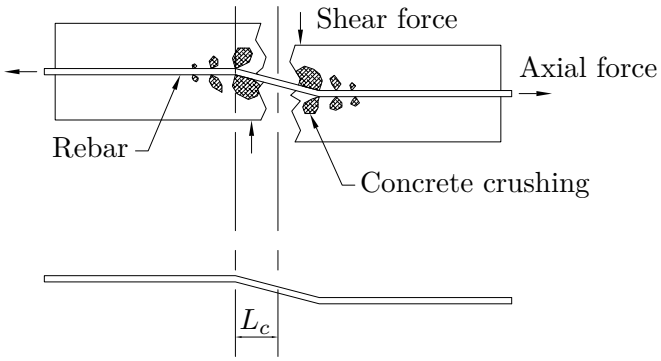

Figure 3.24: Schematic presentation of the curvature influencing zone, adapted from Soltani et al. (2003).

The BE specimens were cast in wooden moulds, constructed from chipboard of 20 mm thick shutterply, and painted to minimise water absorption and prolong the lifetime of the moulds. The wooden moulds are shown in Figure 3.25, with fitted rebar. The secondary stirrups were suspended from the top of the specimen since no top steel is present to tie it to. Figure 3.26 shows the rebar with the initial cast of LWFC mix.

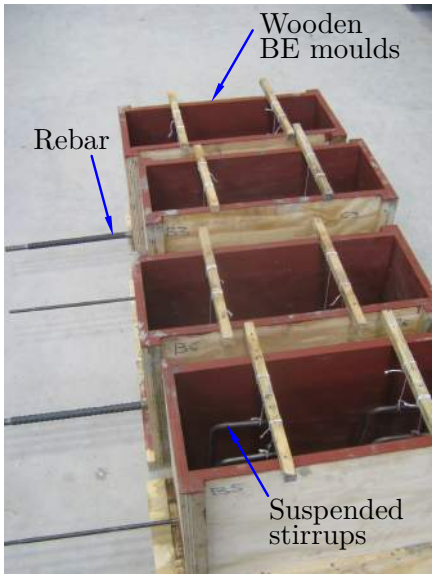

Figure 3.25: Wooden beam-end moulds with fixed rebar, suspended from temporary wooden cross-bars.

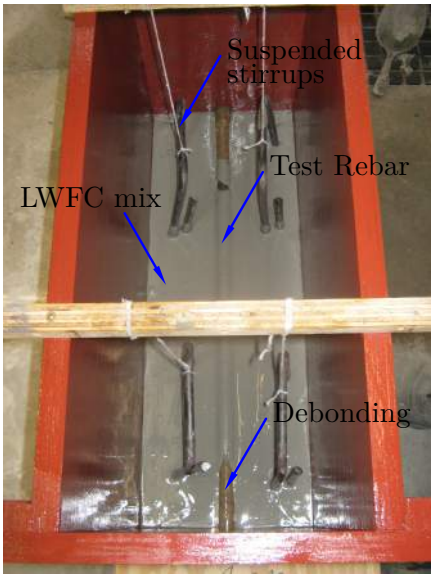

Figure 3.26: Top view of the inside of beam-end mould with fixed rebar and initial casting of a LWFC mix.

3.12.3 Testing machine and rig

The testing machine used for the BE test is an *Instron* with a maximum capacity of 500 kN. The loading rig had to be designed to fit into the existing machine loading frame, as shown in the design drawing in Figure 3.27 (see also Appendix C), which corresponds to a photograph of the BE setup provided in Figure 3.28. This figure refers to a photo focused on the BE

specimen (Figure 3.29), which in turn, refers to photos of the external load cell and the free-end (position 2), loaded-end (position 1) and crack measuring LVDT's (positions 3&4) (respectively in Figures 3.30, 3.31, 3.32 and 3.33). Note the LVDT positions 1, 2 and 3 & 4, for later explanation of measurements and actuator control.

The test setup was constructed from salvaged structural steel from previous studies at the university. Care was taken to ensure enough rigidity in the rig to minimize the deflections and to ensure that no structural failure occurred prior to bond failure. The weakest point in the test setup is, like the PO tests, the connection of the rebar to the testing rig, which governed the design forces allowed during testing. The connection was achieved with a washer and nut assembly, similar to what is done for the PO tests of Section 3.11.

The beam like specimen is installed vertically with the bottom tensile steel (the test bar) on the right side of the specimen (see Figure 3.28). A compression member is fitted to the *Instron* actuator, which provides a compressive force on the top, left face of the concrete. This is typically where the compressive state is found in a beam during flexure. The specimen hangs freely from the rebar connection, whilst being supported laterally. The bottom, right support, provided from the test rig, simulates the beam being vertically supported by a column. The top, left support ensures a shear force being applied as a result of the actuator pressing down on the specimen. This loading assembly ultimately breaks the bonding and the test bar and pulls the bar free from the specimen, simulating the stresses induced by a structural member on an embedded bar.

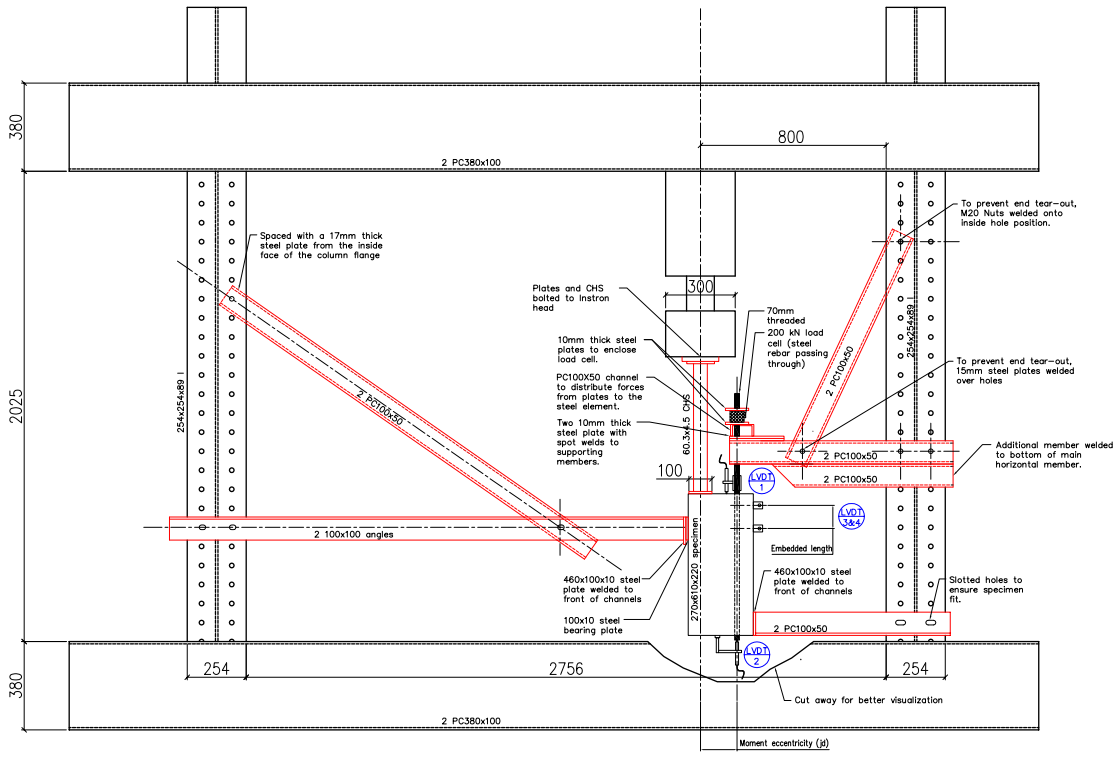

Figure 3.27: The beam-end test design drawing with indication of LVDT positions and fitting of specimen. Refer to Appendix C for the complete design drawing.

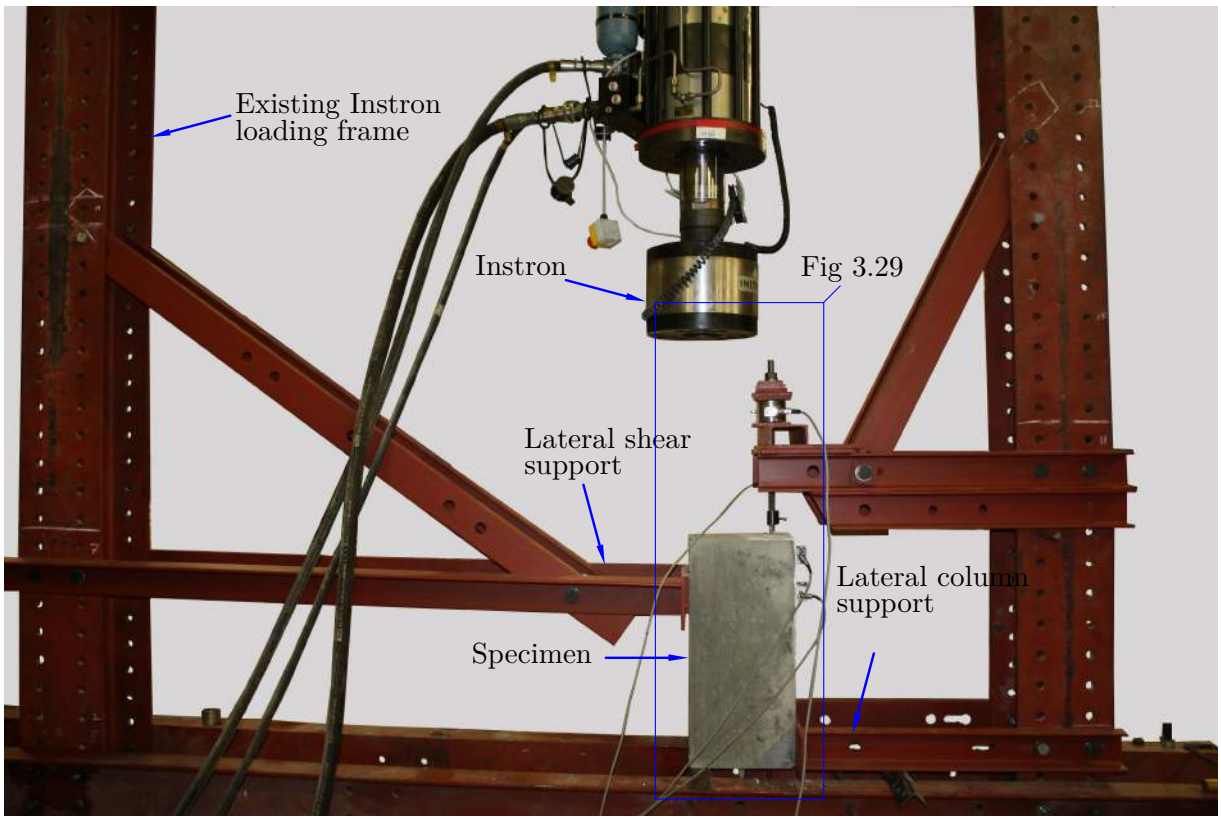

Figure 3.28: The manufactured beam-end test setup assembled into the Instron loading frame, with loaded BE specimen in place.

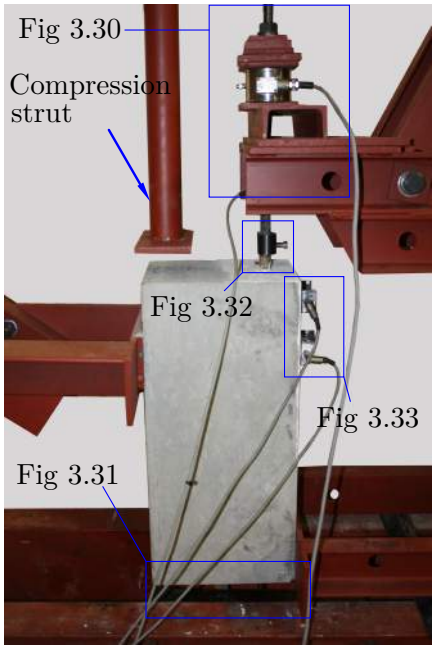

Figure 3.29: Close-up view of the beam-end specimen loaded into the testing rig with the vertical compression strut fitted.

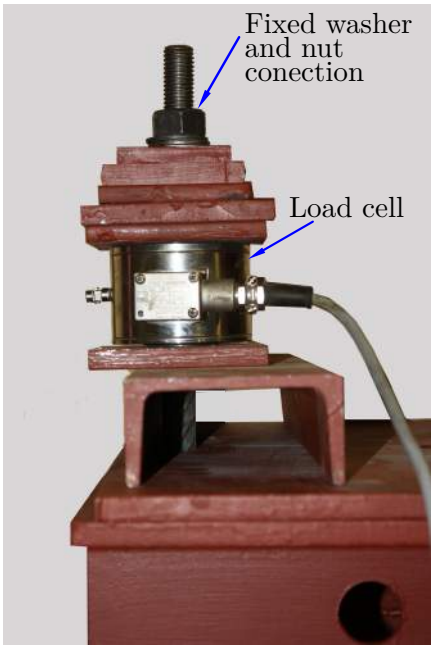

Figure 3.30: Close-up view of the external load cell assembly with the test rebar passing through the load cell, providing an accurate internal bar force reading.

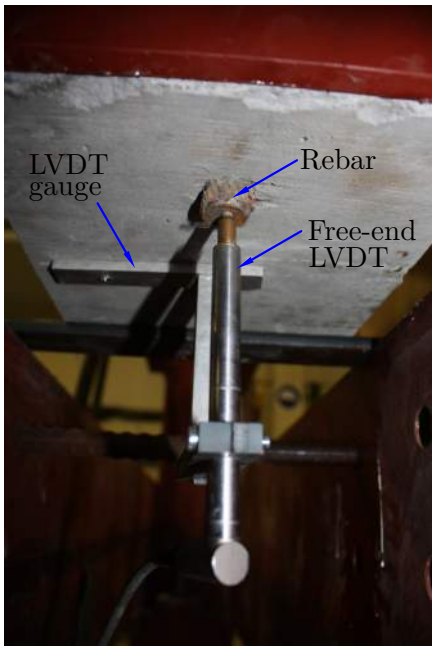

Figure 3.31: The free-end LVDT fitted to a manufactured gauge at the bottom of the specimen, taking the free-end slip measurements. This corresponds to LVDT position 2 in Figure 3.27.

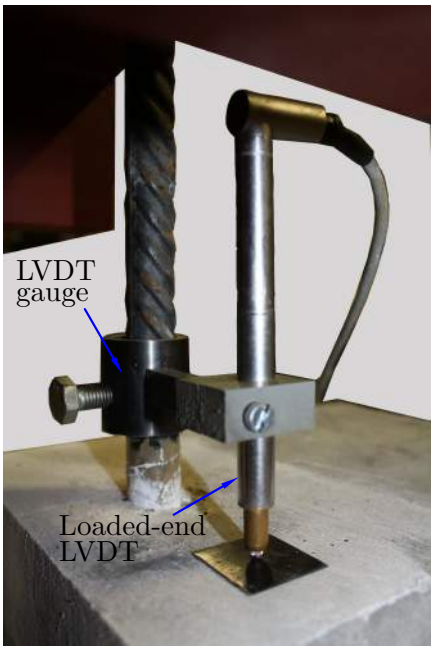

Figure 3.32: The loaded-end LVDT fitted to a manufactured gauge, 50 mm above the top concrete face. This corresponds to LVDT position 1 in Figure 3.27.

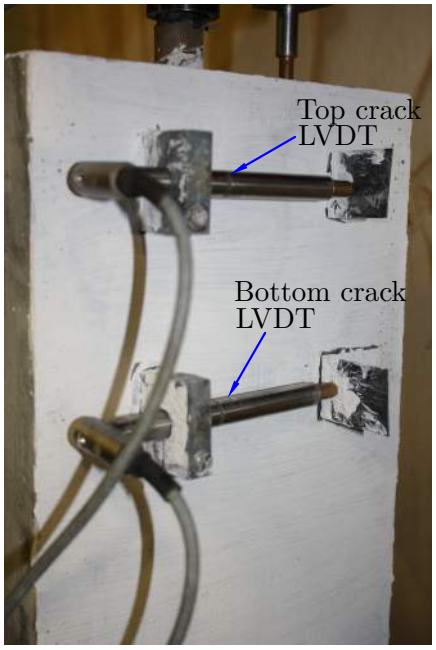

Figure 3.33: The arragement of LVDT's for measurement of a secondary splitting crack, at the start and end of the embedded length. It corresponds to LVDT position 3 & 4 in Figure 3.27.

The embedded steel rebar is fixed, through a load cell to the horizontal support on the right side of the test loading rig. A 200 kN load cell was used to measure the axial force in the reinforcing bar whilst being pulled from the specimen. The bar passes through the load cell as

seen in Figure 3.30. This is done to ensure an accurate force reading within the steel bar, rather than having to rely on a force relationship between the force in the *Instron* actuator and the reinforcing bar.

Figure 3.31 shows a 10 mm LVDT fixed on a gauge fitted to the bottom concrete face and positioned to measure the free-end slip of the bar during the test. This LVDT position corresponds to position 2 on Figure 3.28. A hole is drilled into the bottom face (free-end) of the test bars to ensure a proper seating for the LVDT tip. This is similar to the procedure followed during the PO tests in Section 3.11. This measurement is a crucial reading during the test and is used to obtain the design bond stress. Care should therefore be taken to ensure a proper alignment of the LVDT gauge device and no movement thereof.

Figure 3.32 shows another 10 mm LVDT fixed to the loaded-end of the rebar, 50 mm above the top concrete face with a special gauge. This LVDT position corresponds to position 1 in Figure 3.28. This measurement is sent to the *Instron* as the displacement to control the actuator force being applied. This control process and rates specified during the test are explained in Section 3.12.5. The test setup had to ensure no movement of the LVDT device during testing, since the reading is interpreted by the *Instron* for load application and any erratic or irregular readings, caused by movement of the device, could damage the machine, specimen or test setup.

In addition to the free-end and loaded-end slip measurements, two 10 mm LVDT′s were fitted to the front side of the specimen to detect any internal cracks reaching the surface of the specimen as a result of the force on the rebar. These LVDT positions correspond to the 3 & 4 positions in Figure 3.27, which are positioned at the start and end of the embedded length. Figure 3.33 shows the LVDT′s attached with plastic LVDT supports, glued to the concrete face.

3.12.4 Loading state

The specimen loaded in BE test rig subjects the embedded bar to a more complicated series of stresses as a result of bending moments and shear forces present within the vicinity of the embedded bar. This is different to what happens during the PO test of Section 3.11. The shear stress distribution and bending moment that govern this test are shown in four schematic illustrations in Figure 3.34. These diagrams indicate the simulation of an actual structural beam. The shear distribution through the length of the beam-end specimen is constant and equal to the reaction load from the lateral supports. The bending moment distribution along the length of the specimen is linear, starting at zero from the free-end to a maximum moment M at the section where the bar is being pulled (loaded-end). The bending moment is the product of the bar load, T, and the lever arm, jd.

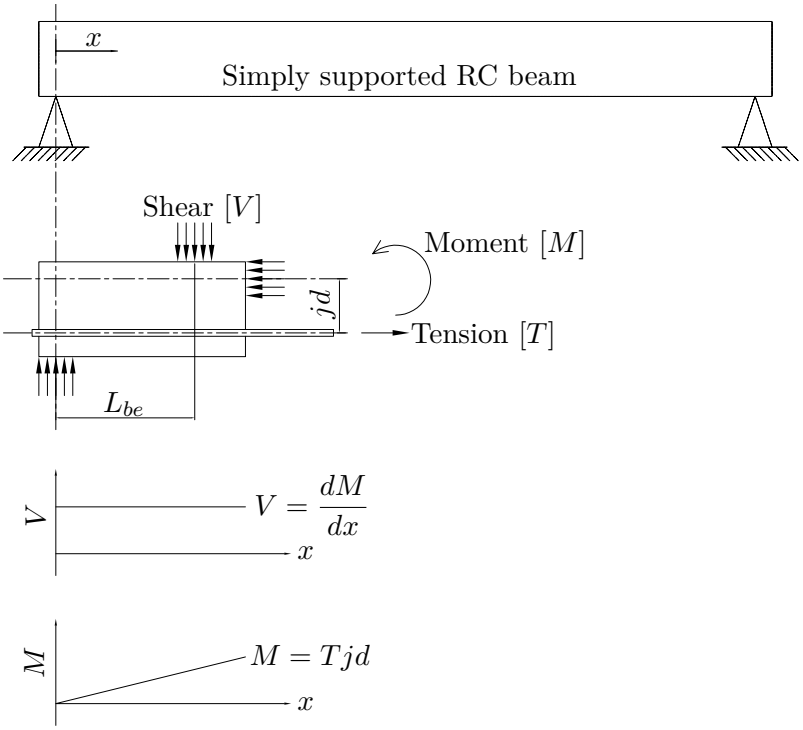

Figure 3.34: Schematic illustration of the shear and bending forces present when loading the specimen during the beam-end test.

Equation (3.10) is used to obtain the bending moment at the section during the tests. Equation (3.11) is then used to obtain the shear force V at the section, which is the derivative of the moment at the section. It is solved by knowing that the area beneath the shear force diagram should yield the maximum bending moment found from (3.10). The shear force can also be solved by considering equilibrium of moments.

$$M = T.jd \tag{3.10}$$

$$V = \frac{dM}{dx} = \frac{M}{L_{be}} \tag{3.11}$$

with

M the bending moment at a cross section in Nm,

V the shear force at a cross section in N,

T the tensile force in a reinforcing steel bar in N,

jd the lever arm of the embedded bar within a structural member in m,

dx the differential length along the specimen length and

L_{be} the length of the beam-end specimen in between lateral supports in m.

3.12.5 Beam-end loading rates

The test specifications provided for the BE test in ASTM A944-10 (2002) do not explicitly define the control system to be used during the test procedure, but do specify that the specimen should not fail within 3 minutes after starting the test procedure. For the preliminary tests of this study the control was rendered to the *Instron* head with a displacement controlled action. These tests ended in abrupt failure, which indicated that better control of the load application would yield more accurate and reliable results. It was therefore decided to control with an external LVDT measurement. The signal from the LVDT is interpreted by the *Instron*, which then alters the actuator reaction to obtain the loading rate specified by the operator. A 10 mm LVDT was set up in position 1 (loaded-end in Figure 3.27), to be the input signal for control.

For the LVDT to function properly loop tuning software was used to calibrate the movement of the LVDT with respect to the load application of the *Instron* head. The machine enters this loop tuning state by altering the applied load to the specimen, which result in sinusoidally fluctuating readings from the LVDT. This sinusoidal path is specified by the user and factors are then altered to allow for the machine to accurately change the load application in order that the LVDT measurement fits the sinusoidal waveform. This alteration in the test control ensures a much slower failure rate and consequently that enough data points are collected during the pre-failure and post-failure stages. Initially it was decided to place the controlled LVDT at position 2 (free-end in Figure 3.27), but the loop tuning seemed not possible at this position since the mean force needed to trigger the movement in the LVDT damaged the bond interface to such extent that the sinusoidal force path could not be established. Position 1 proved to be a much better location for the loop tuning control, since displacement at this point occurs much earlier due to elongation in the steel rebar. The elastic nature of the steel bar ensured that this sinusoidal testing could be done.

For the loop tuning the mean value for the LVDT measurement was set at 0.05 mm and the amplitude at 0.001 mm with a loading frequency of 0.25 Hz. This allows the machine to apply a force until the mean measurement is recorded and then fluctuate the load application at 0.25 times per minute, at an amplitude of 0.001 mm. Therefore the machine ensures the LVDT measurement to displace between 0.049 mm and 0.051 mm. These values were selected by considering the lowest loading rate needed for the BE application. The chosen loading rate is 0.001 mm/s. Therefore the LVDT (when tuned correctly) will displace from zero to 0.001 mm (positive from mean), back to zero, down to −0.001 mm (negative from mean) and back up to zero in 4 seconds. This simulates the machine having to apply a relative displacement of 0.001 mm in a quarter of the period (1 second). Therefore the loading rate at loop tuning stage was simulated to be 0.001 mm in 1 second.

During this loop tuning of the *Instron* machine, the control can be tuned with various factors that all have a unique function of operation. It is known as the PID control; proportional, integral and derivative. Refer to Appendix A for a explanation of these parameters and a summary of the tuning done for the BE tests of this study.

After the control was configured the test method was implemented with multiple steps. The first

step was set at a rate of 0.001 mm/s on the LVDT measurement up to a reading of 0.8 mm. At 0.8 mm the design point has been surpassed and failure, or start of failure should have occurred. The second step was at a LVDT rate of 0.01 mm/s up to a measurement of 5 mm, whereafter the machine was lifted from the specimen and the test concluded with the third step.

-o-O-o-

Chapter 4

Results and Discussion

A series of tests were done in order to determine the design specifications for lightweight foamed concrete and are presented in this chapter. The methods described in design standards that were applied to quantify the engineering properties are compressive strength, Young's modulus, indirect tensile capacity, wedge splitting tests, pull-out and beam-end tests. Stringent control of the specimens and measuring apparatus provided data with information that led to a method to quantify a design bond stress. The mixing of LWFC is accompanied by variation in casting densities resulting from variable constituent addition. Typical deviations in casting density is presented and an acceptable error margin is proclaimed for LWFC.

4.1 Lightweight foamed concrete mix accuracy

The procedure for the design and mixing of lightweight foamed concrete (LWFC), as was given in Section 3.3.4, requires more stringent quality control than with the mixing of conventional concrete and the casting density has to be to within 50 kg/m^3 from the target density. Table A1, in Appendix B, shows the LWFC mixes used with this study, listing the intended target densities, resulting casting densities and the deviation from the nominal values, for both the final mixture of LWFC and the initial base mixture. The average deviation is 25.9 kg/m^3 and 9.8 kg/m^3 for the final and base mixes, respectively.

The mixing apparatus may have an impact on the quality of a mix and has to be carefully monitored and controlled to achieve reliable mixes. In the case of this study the LWFC mixer has a lollipop valve at the bottom for easy extraction of the fresh concrete. The design of the valve leaves a pocket in the mixer into which dry materials accumulate during the initial mixing procedures. The blades of the mixer are not able to reach this accumulated material, which may lead to large errors of the base mix density and eventually the final LWFC casting density. For this reason it is needed to have a quality check on the base mix density prior to the addition of foam. Before the base density is checked, it is advised, after the mixer has been disconnected from the electrical supply, to manually clear out the plug of accumulated materials to allow for uniform mixing. This was done by hand for each mix (wear clean protective latex gloves).

The average errors in the LWFC mixes ranged from 22.2 kg/m^3 to 30.7 kg/m^3, with the 1200 kg/m^3 LWFC yielding the largest error and the 1600 kg/m^3 LWFC the lowest. This is to be expected since the addition and control of the foam entrainment is the least controllable factor during

mixing and therefore a mix that requires more foam content (lighter mix) will inevitably have the highest relative error value.

The foam produced from the foam generator is controlled to retain a density of 75 g/m^3. Various factors influence the foam generation such as the water and air flow, which is a function of the variance in pressure from the compressor. The rate at which the foam is generated is also of importance since the foam is sprayed into the base mix directly from the foam generator, which requires the operator to know the exact rate of flow. The exact mass of foam needed to obtain the required density is known and therefore, after verification of the correct foam density, it is possible to weigh the required mass foam before adding it to the base mix. This method significantly reduces the error made with the foam generation rate and also eliminates human error when adding the foam directly into the base mix. These guidelines were strictly adhered to in order to ensure accurate mixing of the LWFC and compliance with the deviation margin of 50 kg/m^3 could readily be obtained under laboratory conditions.

During this study the mixes were prepared under convenient laboratory conditions, which will most likely be less favourable when done on site. The deviation margin of 50 kg/m^3 should be decreased, because of the significant effect the mixing density has on the strength and bonding capacity, which are discussed in later sections. A drop of 50 kg/m^3 below the target density of 1400 kg/m^3 allows for a drop in compressive strength of 2.46 MPa, which is a loss of 13% of the expected strength at a casting density of 1400 kg/m^3. Mixing LWFC on a construction site, in varying weather conditions and with semi-skilled labour, poses great concern for the accuracy with which the mixing can be performed and therefore stricter control of the mixing process should be implemented in practice to ensure a product of reliable strength.

4.2 Compressive Strength

The procedure for obtaining the 100 mm concrete cube compressive strength at 28 days is provided in Section 3.7. With LWFC's the density has the largest influence on the resulting compressive capacity. The cube compressive strength, f_{cu}, is plotted in Figure 4.1 for the various casting densities, ρ, of the LWFC's tested with a regression fit to the data. Each data point in the figure represents the average for 3 specimens from the concrete mix of every test conducted within this study, in order to compare strengths and also to quantify batch inconsistencies. This figure indicate that the casting density has a significant influence on the compressive strength at 28 days. The 12F, 14F, 16F and 18F specimens yielded average compressive strengths of approximately 10 MPa, 18 MPa, 31 MPa and 51 MPa, respectively. The 20 MPa structural compressive strength lower limit falls between the groups of 14F and 16F data points.

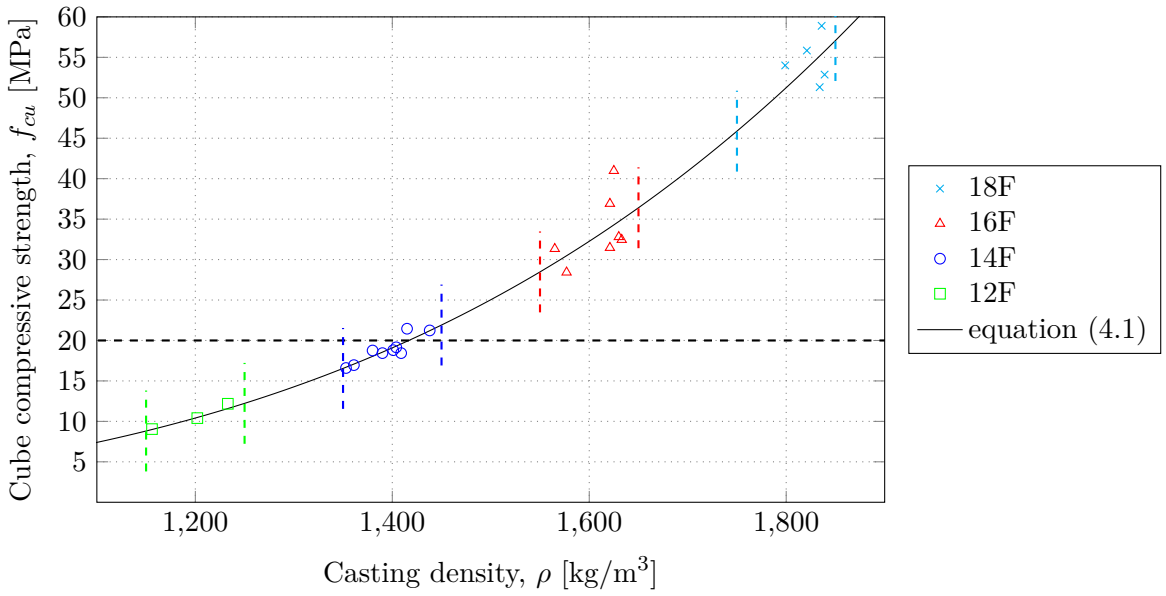

Figure 4.1: A plot of the measured mean cube compressive strength results of all tests on LWFC, versus the casting density. A power law relation is seen between the density and resulting cube compressive strength, and the data is fitted to a regression line (solid line). The lower limit to compressive strengths suitable for structural use is indicated by the dashed line at 20 MPa, showing the 14F falling just below, and the 16F surpassing this limit. The allowable casting density error margin is also indicated (vertical dashed lines) and shows the effect the error could have on resulting compressive strengths.

The data in the figure also indicates the measured variance in casting densities with the data points loosely grouped around the target densities. These deviations in casting density were reported in Section 4.1. The effect of these deviations from the target densities on the resulting compressive strength is prominent when considering the gradient of the fitted curve (solid line) in Figure 4.1, which is given by equation (4.1).

$$f_{cu} = 8.25 \times 10^{-12}.\rho^{3.93} \tag{4.1}$$

The allowable casting density error of 50 kg/m^3 is also indicated in Figure 4.1 with the coloured dashed lines for every casting target density of LWFC tested. It can be concluded that an error in casting density has a larger influence on the variance in compressive strengths of denser LWFC (e.g. 16F and 18F), opposed to that for a similar density error for a lighter LWFC (e.g. 12F).

These findings indicate that sufficient structural compressive strengths can be obtained for the LWFC tested and that the effect of deviations in target density as these points influence the resulting compressive strength considerably.

The mean cube compressive strengths of the normal weight concrete (NWC) specimens were also tested and listed in Table 4.1, also indicating the associated coefficient of variance (COV) of three tests for each result. The NWC specimens yielded compressive strengths similar to what was recorded for the 16F specimens.

Table 4.1: NWC cube compressive strength (f_{cu}) results for the various tests conducted with NWC.

Specimen	f_{cu}	COV
N-T	36.91	0.042
N-E	40.30	0.051
N-PO	36.91	0.042
N-BE	40.50	0.015
Specimen notation in Section 3.2.		

4.3 Young's modulus

The Young's modulus of LWFC with densities 1200 kg/m^3, 1400 kg/m^3, 1600 kg/m^3 and 1800 kg/m^3, and the NWC were measured according to the test procedure specified in Section 3.8, and compared to expected Young's modulus values from existing models for NWC and lightweight aggregate concrete (LWAC). The results obtained for the Young's modulus are represented by an average of 3 tests conducted and Figure 4.2 provides the relation between the Young's modulus, E_c, and the cube compressive strength, f_{cu} (introduced in Section 4.2). The results are compared to accepted equations from British Standards and also listed in Table 4.2, with COV again pertaining to the variance seen within three tests conducted.

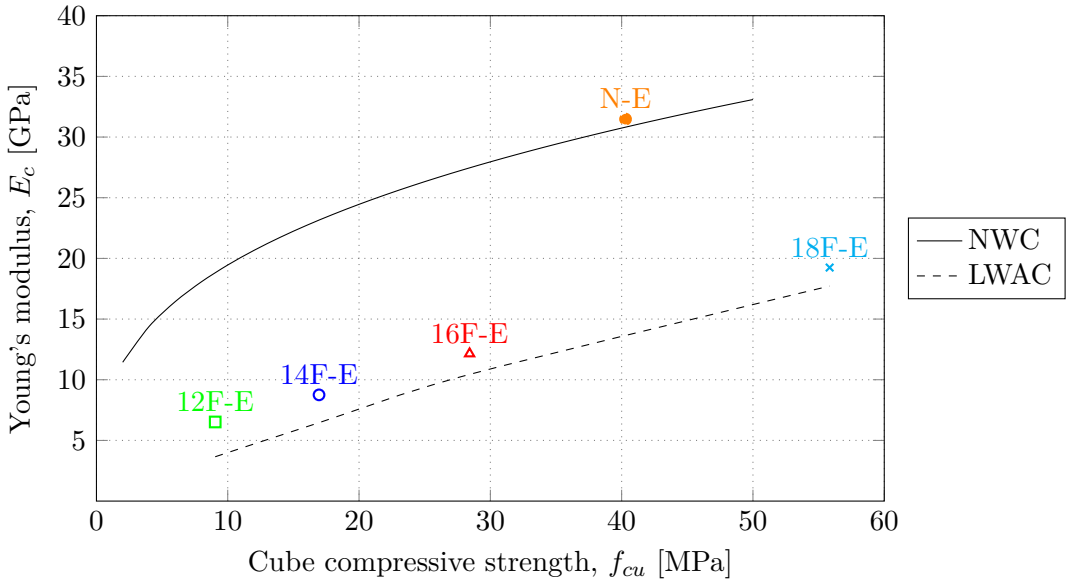

Figure 4.2: The Young's modulus results for the range of LWFC's and NWC compared to accepted equations from British standards (BS EN 1992-1-1, 2004). It concludes on the reduced Young's modulus observed for LWFC compared to NWC and similar results found when compared to LWAC. The NWC curve (solid line) follows from equation (2.7) and the LWAC curve (dashed line) from equation (2.8), in Chapter 2.

Table 4.2: Measured Young's modulus results for LWFC and NWC. The concrete compressive strength (f_{cu}) and COV are indicated for 3 specimens per result.

Specimen	E_c [GPa]	COV	f_{cu} [MPa]
12F-E	6.46	0.0298	9.05
14F-E	8.75	0.0011	16.95
16F-E	12.15	0.0216	28.42
18F-E	19.25	0.0297	55.84
N-E	31.48	0.1143	40.30
Specimen notation in Section 3.2.			

The Young's modulus for the LWFC falls below that of the nominal values stated in BS EN 1992-1-1 (2004), as expected. However, it is seen that LWFC has a larger Young's modulus compared to LWAC. As mentioned before, LWAC is used extensively and design codes have additional prerequisites for its effective use in design, which is a clear indication that reduced stiffness materials can still be used in design, provided that sufficient tests and studies are carried out to characterize the behaviour of the material. The reason for LWAC having a lower Young's modulus than that of LWFC, is attributed to the fact that lightweight aggregates do not exhibit much stiffness and therefore they do not contribute to the concrete-aggregate matrix combined stiffness. In the case of LWFC the only factor that adversely influences the Young's modulus is the voids as a result of the foam ingredient.

The LWFC's with casting densities 1200 kg/m^3, 1400 kg/m^3, 1600 kg/m^3 and 1800 kg/m^3 respectively achieved 35%, 38%, 44% and 56% of their NWC compressive strength equivalent.

The single NWC test correlates well with the predicted Young's modulus for typical NWC.

4.4 Indirect tensile capacity

The indirect tensile splitting tests were performed according to the specifications stipulated in Section 3.9. The average of 3 results for the tensile splitting stresses are presented in Figure 4.3, which gives the relation between concrete compressive strength (f_{cu}) and tensile cube splitting stress (f_t). The results are also listed in Table 4.3 with f_t the indirect tensile strength and coefficient of variance (COV) for three tests.

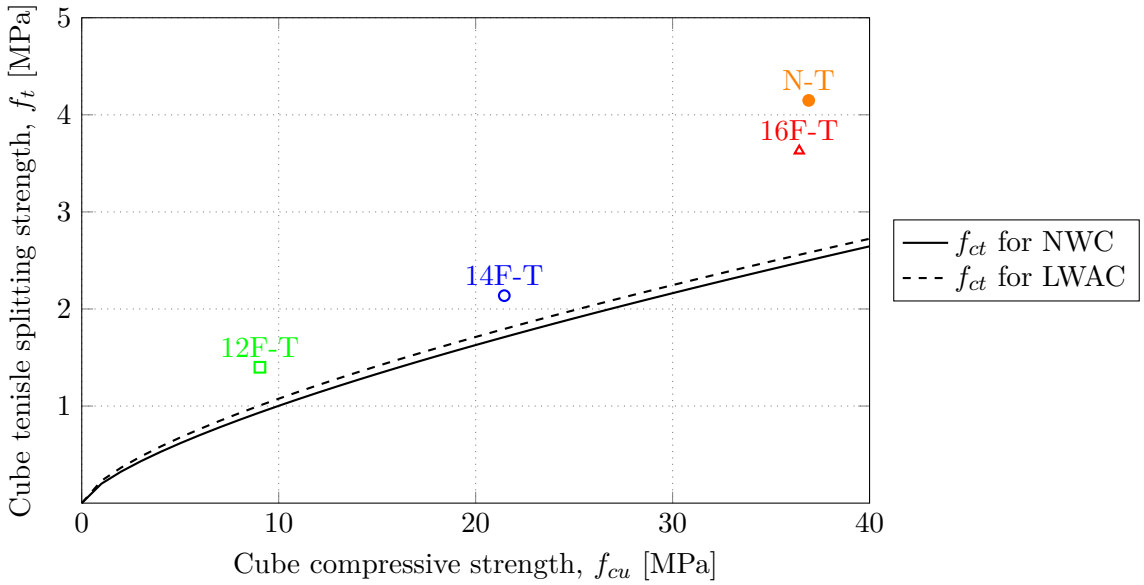

Figure 4.3: Indirect tensile splitting strength test (cube) results of LWFC and NWC in relation to the resulting compressive strength, compared to a known relation for split cylinder tensile strength (f_{ct}) for NWC and LWAC from BS EN 1992-1-1 (2004).

Table 4.3: Indirect tensile strength results for LWFC and NWC tested.

Specimens	f_t [MPa]	COV	f_{cu} [MPa]
12F-T	1.31	0.061	9.05
14F-T	2.14	0.062	21.45
16F-T	3.63	0.092	36.43
N-T	4.15	0.017	36.91

Figure 4.3 shows that the tensile capacity of 1600 kg/m^3 LWFC is slightly less than that of the NWC with similar compressive strengths. The 1200 kg/m^3 and 1400 kg/m^3 LWFC's have reduced tensile capacities in reference to what is considered a structural concrete.

These values are compared to relations found in BS EN 1992-1-1 (2004) for NWC and LWAC, given by equations 2.5 and 2.6, respectively. These models were fitted to measured data on indirect tensile tests conducted on cylindrical specimens and suggests that the these specimens yield a more conservative indirect tensile strength since the LWFC and NWC tests surpass the suggested envelope for NWC or LWAC. The tests do however still provide a relative indication of increase in indirect tensile capacity for increase in LWFC casting density.

These results are later used in the evaluation of the characteristic length in the following section.

4.5 Wedge splitting tests

The wedge splitting tests were conducted on the range of LWFC's according to the specifications described in Section 3.10. These results, together with the tensile splitting results, provide an indication of the ability of LWFC to handle tensile stresses, relative to what is acceptable for NWC. The low crack resistance of LWFC forced the machine control rates (rate of crack opening displacement - COD) to be kept very low in order to obtain stable fracture.

Wittmann (2002) conducted the same wedge splitting test on two normal concretes (NC) (or NWC) and one high strength concrete (HSC) of cube compressive strengths 35.3 MPa, 57.4 MPa and 112.2 MPa, respectively. Wittmann (2002) presented a specific fracture energy (G_f) formulation as a function of the maximum particle size of the aggregates (φ_{max}) in the concrete matrix. This formulation is based on the fact that crack propagation is delayed by aggregates in the crack path and the larger the aggregates the more crack deviation is enforced. In the case of mortar mixes the maximum particle size of cement is used. The formulation is given by equation (4.2).

$$G_f = (80.6) .\varphi_{max}^{0.32} \tag{4.2}$$

The maximum particle size is in mm and the specific fracture energy in N/m. For the mortar mix tested by Wittmann (2002) the assumed cement particle size was 0.01 mm, which resulted in a G_f of 18.5 N/m. This provides a good indication of the typical fracture energy values expected for mortar mixes, which closely resembles LWFC.

Brittleness can also be correlated to the rate at which cracks propagate through the concrete matrix and is quantified by the characteristic length, l_c, introduced in Section 3.10. With NC and HSC the aggregates delay this propagation and ensure a less brittle failure. A pure mortar mix therefore yields a higher degree of brittle failure since there is no delay in the crack propagation due to the absence of aggregates. LWFC, which is essentially a mix of paste and entrained air, will show high degrees of brittle failure and a lowered specific fracture energy. In the case of LWFC the presence of voids actually promote crack growth since the voids can not oppose any tensile stresses in the material. One can therefore deduce that the amount of entrained air would be inversely proportional to the measured specific fracture energy for LWFC.

Figure 4.4 shows the measured LWFC wedge splitting test results, where the horizontal splitting force (F_h) is plotted against the crack opening displacement. Refer to Section 3.10 for test setup with indication of COD measurement and control. Of the three specimens tested for each LWFC density, only one of each density group exhibited stable fracture. The dashed and dotted lines indicate the paths of the specimens that failed prematurely and unfortunately their data cannot be used for interpretation. These premature failures emphasize that LWFC fracture energies are relatively low and it is believed that the pre-load could have damaged the specimen, rendering the COD control not effective. The pre-load of the machine was set to the lower limit, which is 100 N. For the purpose of comparison between the fracture energies of LWFC and NWC, only

the specimens that showed stable fracture were used for further evaluation.

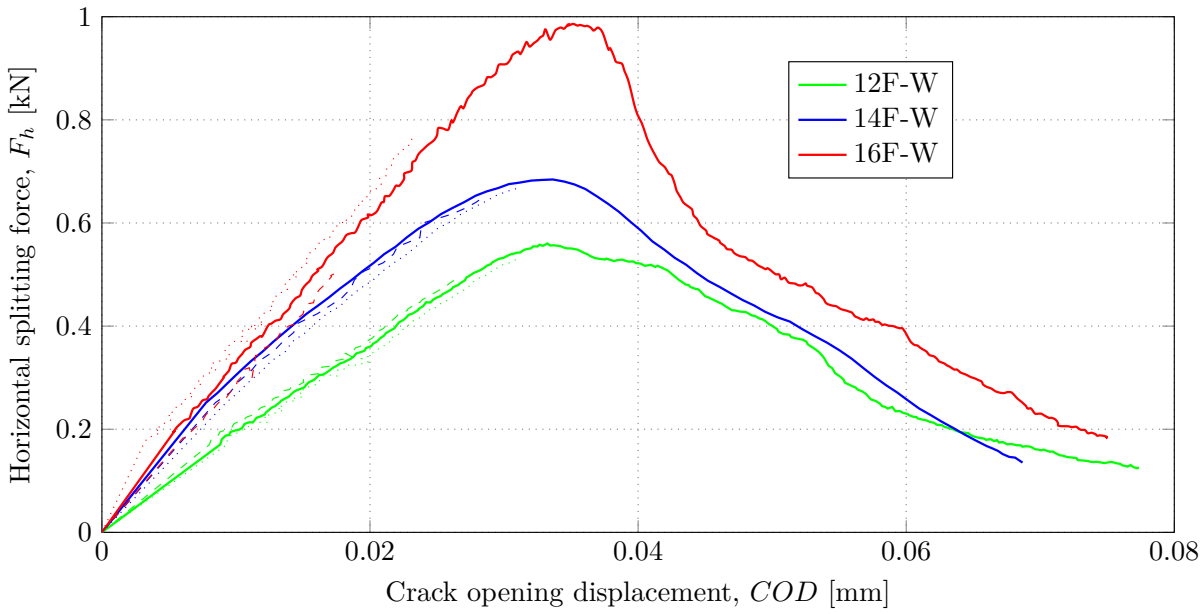

Figure 4.4: The results of the wedge splitting tests on LWFC with the horizontal splitting force versus the crack opening displacement (COD) being indicated. Only one specimen in the group of three similar specimens had stable fracture and was used in further evaluation.

The area under a curve in Figure 4.4 is the fracture energy in Nm, whilst this value, normalized to the fracture area, provides the specific fracture energy, G_f, in N/m. In Section 3.10 the specimen dimensions were introduced with an indicated fracture area of 50x100 mm^2.

Table 4.4 lists the specific fracture energies (G_f) and characteristic lengths (l_c) obtained from the tests performed, which correlate to the stable fracture graphs in Figure 4.4. The specific fracture energies and characteristic lengths for the study by Wittmann (2002) are also listed in this table for comparison to typical structural concrete fracture properties. HSC is considered a be a very brittle concrete, which is confirmed by the lower characteristic length value, relative to the NC. The values for both the NC and HSC are much larger than those measured for LWFC.

Table 4.4: Specific energies (G_f) and characteristic lengths (l_c) obtained for LWFC from wedge splitting tests presented in Figure 4.4, compared to values for NWC by Wittmann (2002).

Specimens	G_f [N/m]	l_c [mm]
12F-W	4.67	17.58
14F-W	5.72	11.12
16F-W	7.32	6.75
NC1*	123.55	938
NC2*	152.05	1300
HSC*	158.70	538
*Wittmann (2002)		

Table 4.4 provides the means to assess the relative brittleness of LWFC. The denser 16F-W specimens attained a characteristic length of 6.75 mm, while the 12F-W specimens yielded 15.42 mm, which renders the 1600 kg/m^3 LWFC a much more brittle material. The measured data therefore confirms that the fracture energy and brittleness are inversely proportional to the amount of air entrained.

These distinctive trends can be observed when the specific fracture energies (G_f) (Figure 4.5) and characteristic lengths (l_c) (Figure 4.6) are plotted against the air entrainment, for which the ratio of casting density to the base mix density, $\frac{\rho}{\rho_b}$, is used to define the latter. The specific fracture energy is directly proportional and the characteristic length, and therefore brittleness, is inversely proportional to the mix density ratio or air entrainment.

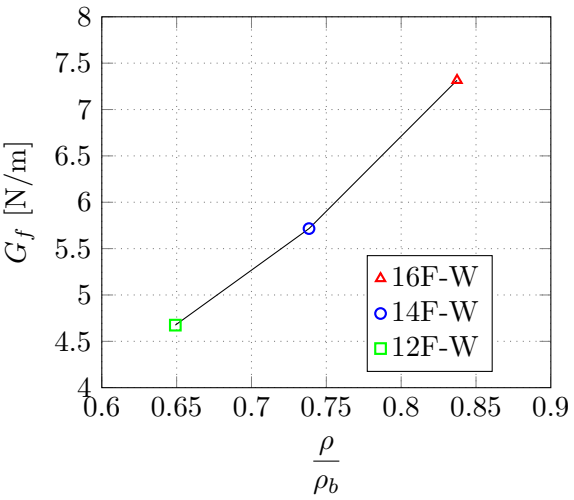

Figure 4.5: A plot indicating the direct proportional change in the specific fracture energy observed for a decrease in air entrainment (the ratio of casting density to base density) of LWFC.

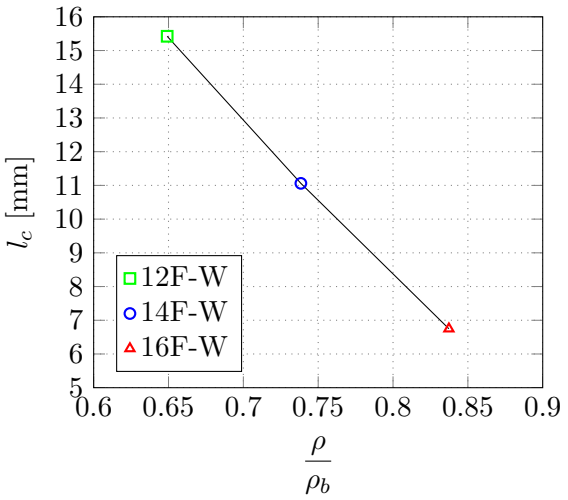

Figure 4.6: A plot indicating the inverse proportional change in the characteristic length observed for a decrease in air entrainment (the ratio of casting density to base density) of LWFC.

The gradients between the data points in these figures give a good indication of the change in fracture energy and brittleness with the addition of air to the mixture. The 1400 kg/m^3 LWFC, with density ratio of 0.74, yields a specific fracture energy and characteristic length of approximately 5.72 N/m and 11.06 mm, respectively. Considering a change of 50 kg/m^3 from a 1400 kg/m^3 to 1450 kg/m^3 LWFC presents an G_f increase of approximately 0.37 N/m and l_c decrease of 1.22 mm. From these data points an extrapolation can be made to predict the approximate fracture properties of the base mix (at $\frac{\rho}{\rho_b} = 1$). The predicted G_f and l_c for the base mix, at a ρ_b of 1881 kg/m^3, is 9.537 N/m and 0 mm. This suggests the base mix is a completely brittle material.

4.6 Pull-out tests

4.6.1 General

The 150 mm cube pull-out (PO) tests were conducted according to the specifications set out in Section 3.11. The PO specimens were cast and tested for the range of LWFC and NWC mixes with Y10, Y12 and Y20 bars, each embedded at 3ϕ, 4ϕ and 5ϕ lengths, with ϕ the nominal bar diameter in mm. The use of testing various embedded lengths is not specified in standards for the testing of PO specimens. However, it is common in literature, dealing with bond behaviour, to test different lengths (Farghal Maree and Hilal Riad, 2014; El Zareef and Schlaich, 2008; Sancak et al., 2011). The selected lengths ensure that test results will exhibit the two failure modes, namely pull-out and splitting failures. It is known that a longer embedded length is more susceptible to fail in splitting, whereas a short embedded length more readily pulls out (Dae-Jin et al., 2014). The reason for this is that the longer embedded length requires a larger force to pull the bar from the concrete, which in turn induces larger local stresses associated with the onset and propagation of internal cracks. The longer embedded length has more steel-concrete interface over which to induce internal cracks. Splitting failure becomes more prominent with increased relative rib area and bar diameter. This increase in rib area induces more direct and drastic transverse stresses, which ensures internal cracks developing more aggressively. The embedded length and steel geometry have a profound influence on the bond behaviour observed, but the response of the surrounding concrete influences the bond capacity even more.

4.6.2 Stresses at the bond interface

The schematic diagram in Figure 4.7 shows the various stresses present when an embedded bar is axially loaded by a force T. The side of the bar to which the load is applied is the loaded-end while the opposite end is termed the free-end. Refer to Section 3.4 for an indication of the loaded-end and free-end on a specimen. v_a represents the adhesion stresses, which are considered to be the chemical adhesion of the steel surface to the concrete in contact. The adhesion stress exists all over the contact area of the steel and is the first contributor to the bond capacity to fail during testing, and usually only manifests in micro-slip. The adhesion stress in NWC is considered so insignificant that it may effectively be ignored (Park and Paulay, 1975). This assumption is evident in the bond-slip model proposed by Model Code (2010) which allows for zero adhesion stress (refer to Section 2.4.1). The bearing stress of the steel rib on the concrete is indicated by v_b and the failure of the concrete bearing capacity is accompanied by crushing of the concrete keys, which are embedded between the steel ribs and contribute to the slip of the bar. The shear stress is represented by v_s acting on the surface of a cylindrical portion of the concrete in between successive steel ribs, which is induced by the relative movement of the concrete and the bar. The bearing and shear contributes to the collective, so-called, mechanical bond term, which is considered the resistance of bond after adhesion has been lost. Some frictional stresses also exist after the initial adhesion bond is surpassed, however these frictional stresses are insignificant compared to the mechanical bond contribution.

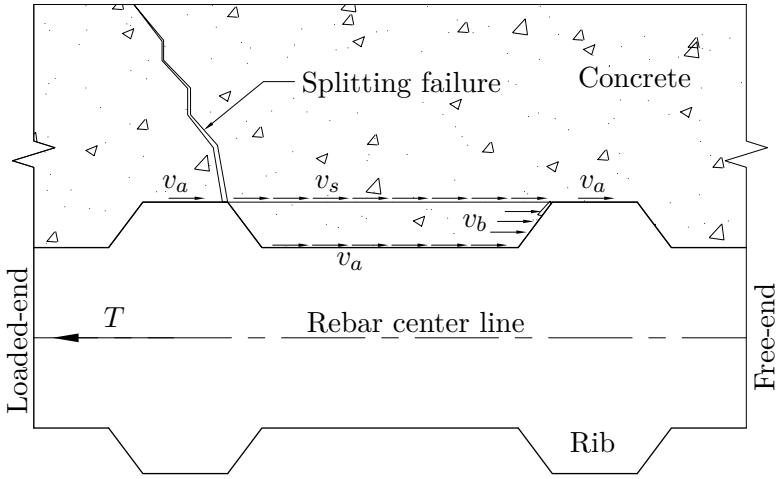

Figure 4.7: Stresses and forces present during axial bar loading in the process of bond deterioration and eventually loss of bond, with v_a the adhesion stress and the mechanical bond characterized by the bearing stress, v_b, and shear stress, v_s.

Pull-out failure is associated with a combination of the shear stress, v_s, reaching the concrete's capacity and the bearing pressure, v_b, reaching the compressive capacity; collectively creating a slip failure surface after which the bar is pulled out with concrete-on-concrete friction being the only resisting force. Splitting failure is characterized by internal cracks starting from the steel-concrete interface as a result of the bearing action of the steel on the concrete and the resistance provided by the shear plane in between ribs. The bearing of the ribs on the concrete crushes the concrete, which allows for bar slip to occur. Theoretically splitting failure can only occur if the shear capacity is not exceeded. The shear capacity resists this slip action as a result of crushing, which ultimately opens an internal crack where the bearing face and shear face meet. The internal crack forms once the tensile stress or strain capacity of the concrete is reached. These internal cracks propagate towards the concrete surface to create secondary cracks which ultimately lead to splitting failure. Once these internal cracks start forming they have a significant influence on the bond capacity and are usually characterized by sudden loss of bond and overall stiffness of the test specimen (Pedziwiatr, 2008).

The failure modes are highly dependant on the parameters shown in Figure 4.7. However, the combined occurrence of these failure modes is also evident. This is observed with bond slip envelopes ending in a sudden splitting failure at a substantial free-end slip value, which implies that the specimen initially pulled out until the internal cracks propagated to form secondary cracks and eventually causing sudden splitting failure. This failure pattern is however recognized with some form of slip (pull-out), which can be explained by the crushing of the concrete in between ribs allowing space for the bar to slip. In these cases the shear capacity is not overcome and this resistance allows for a stress gradient at points along the bar. These points lead to internal cracks, which in turn lead to secondary cracks with increasing bar load. If the shear stress were to reach the concrete capacity within the loading stages, pull-out failure would be recorded rather than splitting failure. This suggests that concrete with a high shear capacity might be more susceptible to splitting failures. Pure splitting failure is observed when the peak splitting force is reached without any free-end slip recorded. In this case the bearing capacity

is not overcome but restricts movement and allows for great resistance to pulling forces at the free-end. Here it has to be noted that zero free-end slip does not necessarily mean the bar is not displacing along the embedded length. In fact the delamination, and thus movement, first occurs at the loaded-end. Therefore a longer embedded length might yield a result which attains the peak splitting stress without any free-end slip. This implies that at the loaded-end, an internal crack has formed and propagated to a secondary crack before displacement occurred at the free-end, ending in splitting failure.

These complex failure mechanisms emphasize the difficulty with testing for bond properties. This is especially evident in the LWFC of which material properties are not as well characterized as for NWC. The LWFC generally exhibits more splitting failures due to its reduced tensile capacity (Dae-Jin et al., 2014). This however does not imply that a LWFC structural member will exhibit splitting failure along all embedded bars once loaded in a structural application. With the correct addition of lap lengths, anchorage and the use of secondary reinforcement, the same bond performance could be achieved as for structural application of NWC. Refer to Figure 2.9, which shows that given sufficient transverse pressure from secondary stirrups and cover concrete, the splitting failure could be overcome. The question remains what these design considerations are and whether they are at all economically feasible.

4.6.3 Adhesion loss and design point

The adhesion is the first bond resistance to fail and starts at the loaded-end and progresses towards the free-end. It is therefore fair to assume that as soon as the first free-end slip measurement is read, loss of adhesion has already occurred towards the loaded-end and has therefore lost adhesion across the entire embedded length. It is assumed that the loss of adhesion is taken at the moment where the free-end LVDT measurement first registers 0.001 mm. This value is the resolution of the LVDT measuring device and therefore provides the operator with the closest point where adhesion was lost at the free-end.

As mentioned in Section 3.5, it is common in literature to accept a design bond stress at a certain slip. A peak stress cannot be used in design since it is associated with near complete loss of bond; something which should be avoided at all cost in a reinforced concrete structure. This design point is commonly taken at 0.1 mm free-end slip (Leonhardt, 1977; Farghal Maree and Hilal Riad, 2014) as discussed in Chapter 2. This slip position will from here on be referred to as the design point and any stress or bond stress ratio with a subscript d represents the design point. The peak stress is used for those specimens that failed in splitting and have not reached a slip of 0.1 mm. The reason is that if sufficient concrete cover was provided the stress would have developed along the same path until pull-out peak failure is reached. Taking this peak splitting stress is then proven to be a lower bound solution and therefore still safe and applicable when assessing the design bond stress. Refer to Section 2.4, Figure 2.12, for a schematic explanation to the conservative bond stress found from splitting failure tests.

The development length, l_d, is the length needed in order to fully transmit the bar yielding force through the bond interface. This development length is obtained with equation (4.3), which is

found from summation of forces using the average design bond stress (σ_{ad}) as the mechanism for equilibrating the forces. This average design stress is taken as an average across the various embedded lengths tested.

$$l_d = \frac{\phi.f_y}{4.\sigma_{ad}} \tag{4.3}$$

with

l_d the development length in mm,

ϕ the nominal bar diameter in mm,

f_y the characteristic yield strength of the reinforcement in MPa (taken as 450 MPa), and

σ_{ad} the average design bond stress in MPa.

4.6.4 Pull-out results and presentation envelopes

The compiled results obtained from the pull-out tests are listed in Table A2 in Appendix D, with σ_d the design bond stress, σ_a the bond stress at which adhesion is lost, σ_{ad} the average design bond stress, and l_d the development length.

The data in Table A2, are presented as pull-out envelope graphs in Figures 4.8 to 4.19, each with similar characteristic information. The stress at which the first slip is recorded is considered to be the point of adhesion loss. In order to enhance the presentation of data in the region of the bond stiffness interface, the slip between 0 mm and 0.2 mm was enlarged by a factor of 5. This area on the graph is left in white, while the rest of the graph is presented with a grey background. At the transition from the enlarged region to the normal region a jump can be seen in all the bond envelopes. These blips on the envelope should not be interpreted as physical phenomena, but merely the result of this transition of scaling. The position of the design point is indicated with the vertical dashed line at 0.1 mm.

The bond stress distribution is assumed to be constant and uniform, acting on the bar surface found from the nominal bar diameter. For short embedded lengths this uniform bond stress (average bond stress) assumption may be made. For example, a Y20 bar's uniform bond stress will be calculated by dividing the bar load by the area in contact with a cylinder of diameter 20 mm and length equal to the embedded length.

4.6.5 Pull-out envelopes of NWC

The NWC specimens with Y10 and Y12 bars all exhibited pull-out failure while the tests with the Y20 specimens all ended in splitting failure. This was expected since it is known, and mentioned earlier, that specimens with bars with larger diameters are more susceptible to splitting failure. Similar results can be seen in literature (Dae-Jin et al., 2014). Figures 4.8, 4.9 and 4.10 show

the bond stress development of NWC as a function of the free-end bar slip for Y10, Y12 and Y20 bars respectively. These graphs have specific features that were introduced in Section 4.6.4.

The results for the Y10 bars in Figure 4.8 indicate that the peak bond stress is inversely proportional to the embedded length. The same figure shows an almost similar trend at the design point, with N-P-10-5 yielding a design bond stress just above N-P-10-4, indicated in the magnified region. It is mentioned that longer embedded lengths are more prone to splitting failure and the Y10 envelopes supports this. The relative low bond stiffness, indicated by the gradient of the bond-slip envelope of N-P-10-5 between 0 mm to 0.1 mm slip, gives an indication of possible internal crack formation, which diminishes the bond stiffness.

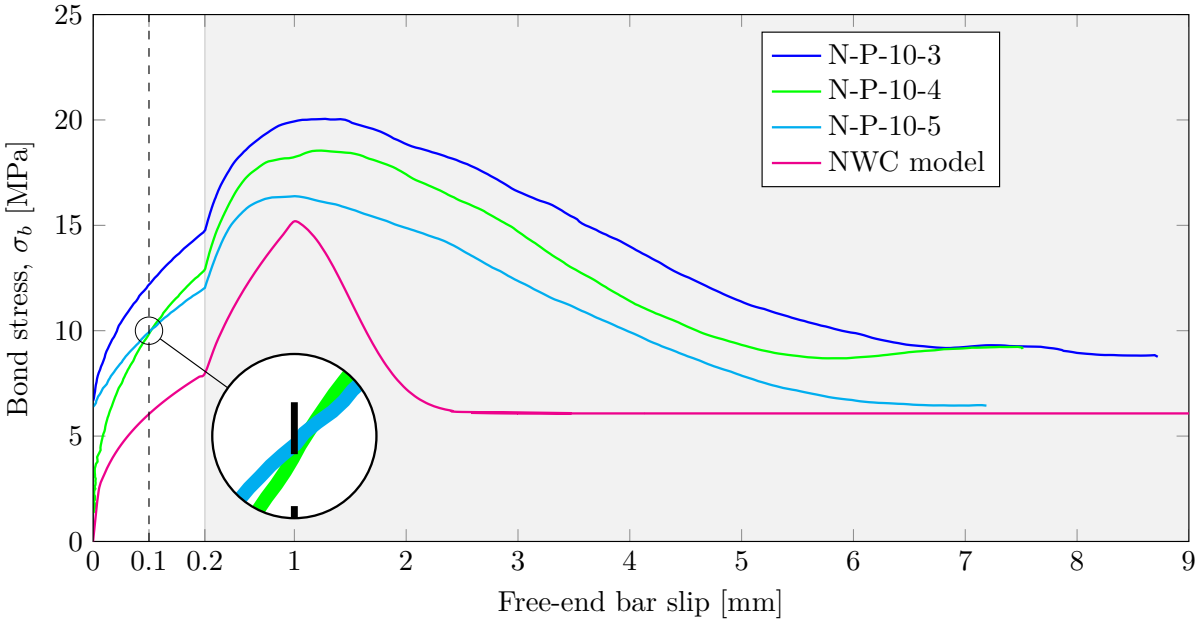

Figure 4.8: The uniform bond stress development versus free-end bar slip for the Y10 bar PO tests with NWC. Free-end slip is enlarged between 0 and 0.2 mm. The proposed bond-slip model by Model Code (2010) is also included.

Theoretically the stress at which adhesion is lost should be equal for all the tests of the same concrete classification. The adhesion is considered such a small contribution to the overall bond capacity that, in most cases, it is ignored. According to the proposed model (shown in figure) of Model Code (2010), the adhesion bond stress is also taken as zero. From the measured data the adhesion loss stresses are not equal and also not zero for NWC and the N-P-10-3 and N-P-10-5 specimens reached the adhesion loss point at a much higher stress than the N-P-10-4 specimen. These adhesion points can be influenced significantly by both the dispersion of voids within the concrete and the aggregates at the bond interface. Here it is seen that the adhesion loss stress is insignificant compared to the resulting bond envelope.

Model Code (2010) has a model representing the relationship of an averaged local-bond versus local-slip for short embedded lengths, which is also presented in the figures together with the measured data for NWC. This model is thoroughly introduced in Section 2.4. In each case the results from the model gives a lower bound solution to the measured results. This is similar

to what was found by Farghal Maree and Hilal Riad (2014), who reported larger NWC peaks than given by this model. In Figure 4.8 the peak of the N-P-10-5 curve is within reasonable agreement with the Model Code (2010) model, but not with the slip position of the peak stress. A 5ϕ embedded length is what is generally reported in literature and is therefore assumed to be the length specified in ASTM C234. The 5ϕ embedded length also corresponds to the residual bond capacity towards the end of the PO test. The lower bound solution provided by the model suggests additional partial factors incorporated, however no documentation exist on any such factors used.

Figure 4.9 indicates the development of bond stress for Y12 bars embedded in NWC. Again these tests all exhibit pull-out failure. The pattern of peak stress, design bond stress and adhesion bond loss is similar to what is seen in Figure 4.8 for the Y10 bars.

For the Y12 bars the 5ϕ curve does not follow the modelled prediction, as was found for the Y10 bars, but it still suffice as a lower bound solution to bond stresses at slip. The model does not change from Y10 to Y12 bars (for the same concrete type), which seems strange since literature suggest a variation in bond with a varying bar diameter (ACI 318-11, 2011; Farghal Maree and Hilal Riad, 2014; El Zareef and Schlaich, 2008).

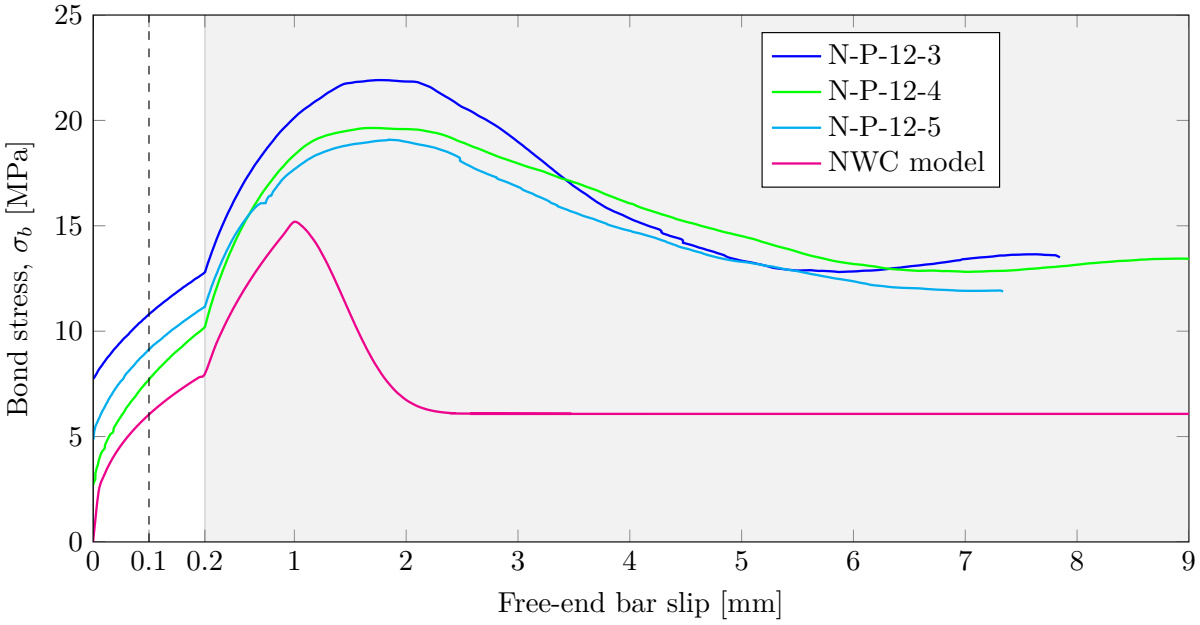

Figure 4.9: The uniform bond stress development versus free-end bar slip for the Y12 bar pull-out tests with NWC. Free-end slip is enlarged between 0 and 0.2 mm. The proposed bond-slip model by Model Code (2010) is also included.

Figure 4.10 shows Y20 bars embedded at the 3 lengths all exhibiting splitting failure, as can be seen from the sudden drop in bond stress after reaching a peak stress. Again, a similar trend is seen with the longest embedded length (N-P-20-5) yielding the lowest design bond stress and the shortest embedded length (N-P-20-3) yielding the largest design bond stress. This is also what is to be expected since larger bars and longer embedded lengths are more susceptible to splitting failure and therefore results in a more conservative bond envelope, similar to what is

seen for Y10 and Y12 bars embedded in NWC. Specimens N-P-20-4 and N-P-20-5 reached a peak load before the design slip occurred . The design bond of these specimens will therefore be taken at the peak load and not at the lower actual design point. This, as explained earlier, will still form a lower bound solution to the bond development and the design value used.

The modelled splitting failure is also visible in the graph, but it does not resemble the measured results. Splitting failure is considered a complex failure mode since it is influenced by the concrete matrix surrounding the steel and not just the concrete at the steel interface. It can therefore be deduced that the constituents of the concrete mix influence splitting failure more than with pull-out failure. The model does still form a lower bound solution to the local bond-slip relation during splitting failure. The adhesion loss stresses occur at a larger stress than for the Y10 and Y12 bars, which can be attributed to the increased rib geometry with a greater area of adhesion, which must be overcome before slip occurs. These points do however not occur at the same stresses as suggested by Model Code (2010).

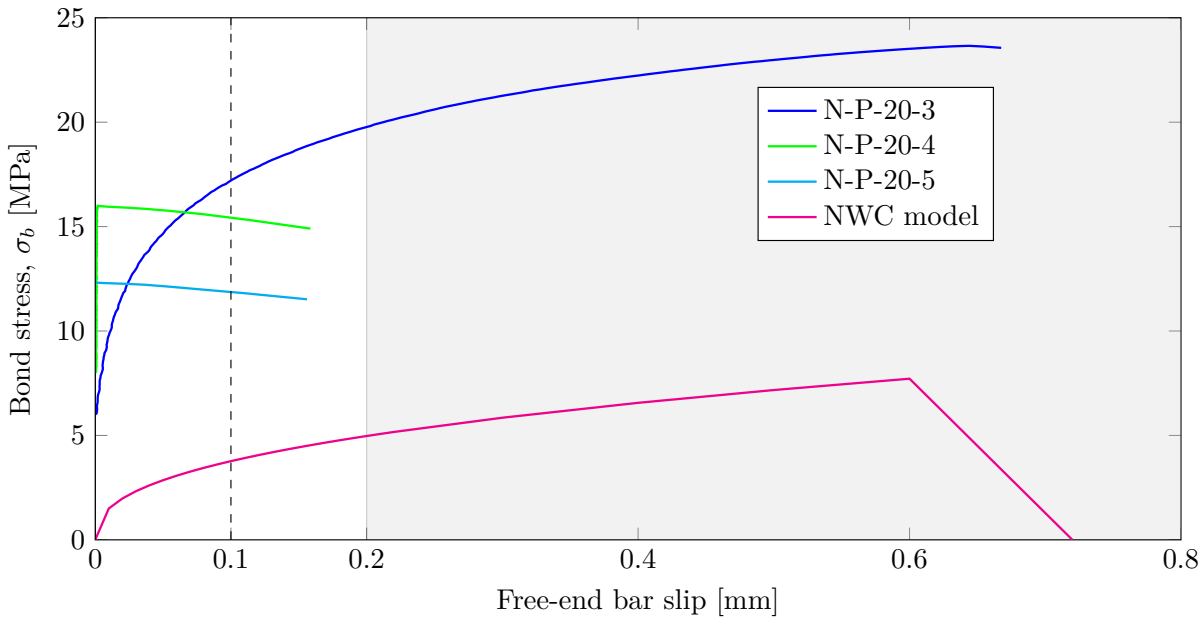

Figure 4.10: The uniform bond stress development versus free-end bar slip for NWC in the pull-out tests of Y20 bars. The proposed bond-slip model by Model Code (2010) is also included.

4.6.6 Pull-out envelopes of 1200 kg/m^3 LWFC

The 1200 kg/m^3 LWFC specimens all failed in pull-out failure during the PO tests. It was shown in Section 4.4 that this LWFC exhibits the lowest tensile strength and with reduced tensile capacity, a splitting failure in a pull-out test would intuitively be most likely. However, Section 4.5 indicated that this LWFC is the least brittle, which ensures other governing failure criteria.

The resulting failure mode depends on which stress capacity is reached first and consequently results in a specific failure associated with that occurrence. In the case of the 1200 kg/m^3 LWFC the bearing of the ribs on the concrete overcomes the compressive capacity of the concrete before

enough stress is built up to induce internal crack formation. Also the shear resistance is reasoned to be low, and thus easily overcome to induce the pull-out failure observed, and not the splitting failure as expected. For this reason pull-out failure is more likely to occur for this mix than splitting. This explanation is a further manifestation of the complicated failure mechanisms present within the steel-concrete bonded system.

Figures 4.11, 4.12 and 4.13 show the results for the pull out tests of Y10, Y12 and Y20 bars, respectively, embedded in 1200 kg/m^3 LWFC. These graphs are similarly constructed as reported above for NWC.

The bond behaviour of 1200 kg/m^3 indicates bond-slip envelopes that do not look similar to what was seen for the pull-out tests of NWC. These graphs start out at a peak value whereafter the bar is pulled out and a negative stiffness in the vicinity of the design bond stress. This suggest that the resistance to pull-out, provided by bearing and shear, is so low that it falls below the adhesion stress resulting in a negative stiffness after adhesion is lost. In the case of a weaker material the adhesion stress becomes much more significant, opposed to the case of NWC.

The measured data of the LWFC pull-out tests are much more erratic and the expected patterns are not observed for the different embedded lengths, compared to what was expected and found for the NWC.

The direct proportional relationship between the bond stress envelope and embedded lengths of Y10 bars are shown in Figure 4.11. In these cases the adhesion is larger than the mechanical bond, because a longer embedded length implies more ribs exposed to retain more mechanical bond capacity. However, even the 5ϕ embedded length yielded a negative gradient at the design point. This suggests that when the rib bearing dominates the failure, a longer embedded length provides the most resistance and eventually leads to a larger bond strength.

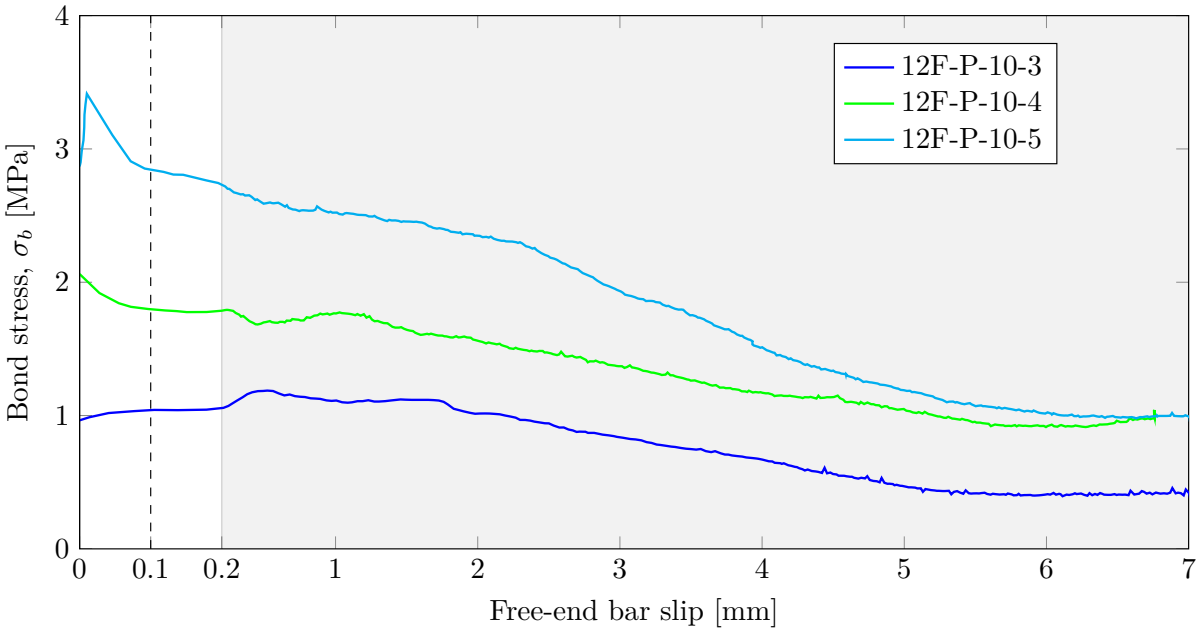

Figure 4.11: The uniform bond stress development versus free-end bar slip for 12F in the pull-out tests of Y10 bars. Free-end slip is enlarged between 0 and 0.2 mm. A negative gradient is seen at the design point, which suggests the adhesion stress is larger than the resulting mechanical bond contribution.

Figure 4.12 shows the bond slip envelopes for 1200 kg/m^3 LWFC with Y12 embedded bars. In this case the 3ϕ embedded length has the largest stress and the 4ϕ and 5ϕ embedded lengths the lower bond stress envelopes. This data is a better emulation of what is seen for typical Y12, NWC pull-out specimens in Figure 4.9 and suggests that the Y12 bar, with a larger relative rib area (f_r), ensures greater mechanical bond relative to the adhesion stress. This argument follows from the positive gradient seen after the adhesion stress is lost for 12F-P-12-3 and 12F-P-12-5.

Specimen 12F-P-12-4 in Figure 4.12 indicates a negative gradient at the design point, similar to what was seen in the Y10 envelopes of Figure 4.11. However, the Y12 test regains stiffness, shown by the positive gradient at 0.2 mm free-end slip. It is believed that this specimen might have been damaged during handling, compromising the adhesion stress and consequently indicating lowered stiffness at the start of the test procedure. With the observed low adhesion, and mechanical bond capacity, the danger of damaging tests specimens prior to testing is very high.

For a listing of the relative rib areas of the rebar used, refer to Section 3.6 in Chapter 3.

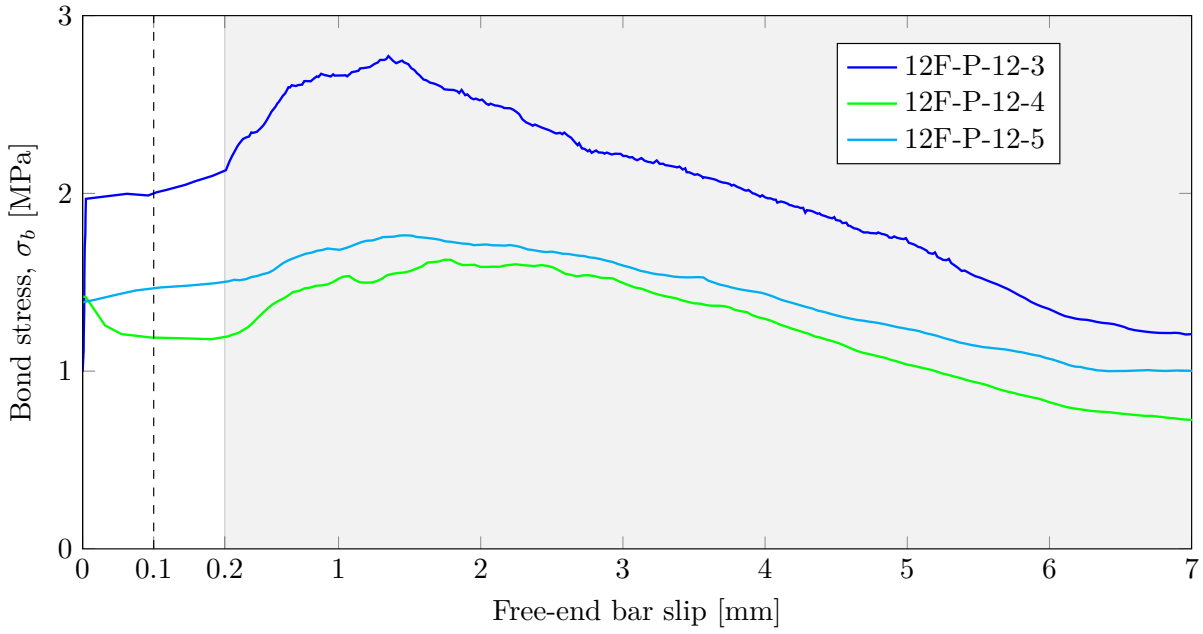

Figure 4.12: The uniform bond stress development versus free-end bar slip for 12F in the pull-out tests of Y12 bars. Free-end slip is enlarged between 0 and 0.2 mm. It is believed that specimen 12F-P-12-4 was damaged during handling and preparation, compromising the initial stiffness of the bond interface.

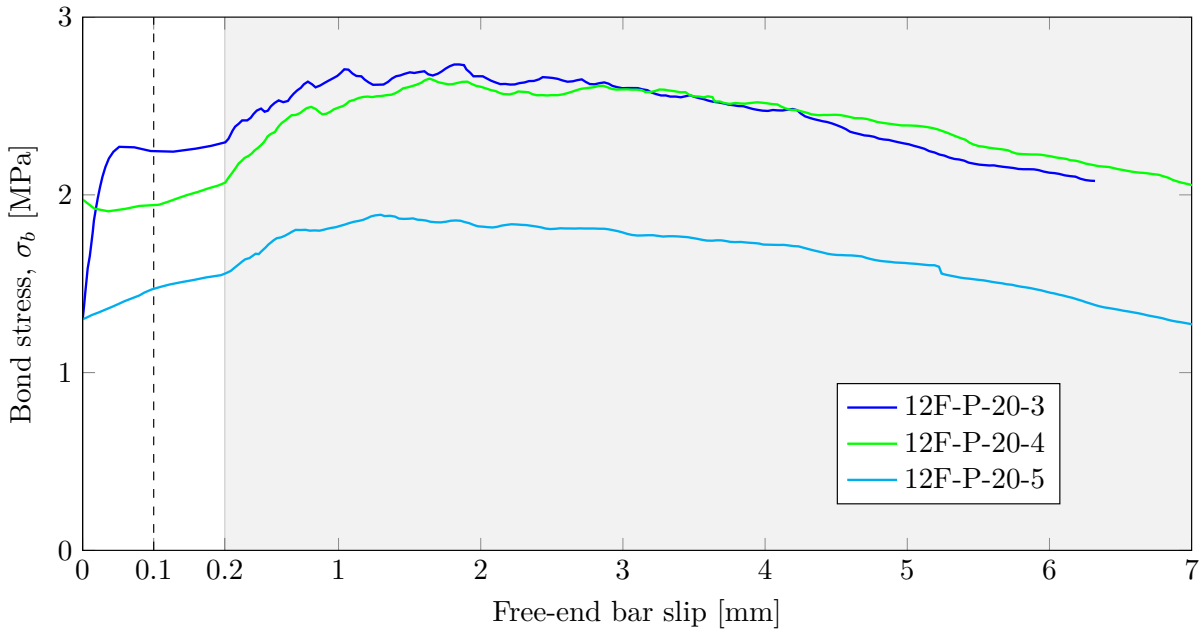

Figure 4.13: The uniform bond stress development versus free-end bar slip for 12F in the pull-out tests of Y20 bars. Free-end slip is enlarged between 0 and 0.2 mm. The observed envelopes is the only Y20 tests to fail in pull-out failure and emphasize the non resistive nature of the 12F specimens, even with bars with larger diameters and relative rib areas.

Figure 4.13 shows the 1200 kg/m^3 LWFC bond-slip envelopes for embedded Y20 bars. Here the design bond is largest for 12F-P-20-3 and lowest for the 12F-P-20-5. This set of data is also in agreement with what was observed for the tests of Y20 bars in NWC, apart from the

difference in failure modes. With the Y20 bars the increase in relative rib area is substantial and thus the increase in mechanical bond, after adhesion is lost, should suffice a positive bond slip gradient around the design point. Even so, these specimens failed in pull-out and are the only Y20 specimens to fail as such, which suggests that, even with the increased rib geometry, the bearing and shear capacity of the 1200 kg/m^3 could not restrain the stresses enough as with the equivalent NWC tests, and thus pull-out failure resulted. These specimens failing in pull-out indicate the non resistive nature of the 1200 kg/m^3 LWFC.

4.6.7 Pull-out envelopes of 1400 kg/m^3 LWFC

The 1400 kg/m^3 LWFC failure modes are similar to those found for NWC, with only the Y20 bars resulting in splitting failure.

Figures 4.14, 4.15 and 4.16 show the bond stress envelopes of 1400 kg/m^3 LWFC for Y10, Y12 and Y20 bars respectively. When comparing the earlier mentioned measured results of engineering properties, the increase in density of LWFC ensures larger compressive stress, Young's modulus and tensile strength, and increased brittleness. These findings have to be considered when addressing bonding.

The 1400 kg/m^3 LWFC Y10 specimens in Figure 4.14 show a positive gradient in bond development within the vicinity of the design point. This was not seen with the results of the 1200 kg/m^3 LWFC Y10 specimens in Figure 4.11, where the adhesion bond stress dominates the subsequent mechanical bond resistance. This implies the denser LWFC exhibits greater bearing and shear resistance, enabling greater mechanical bond after adhesion is lost.

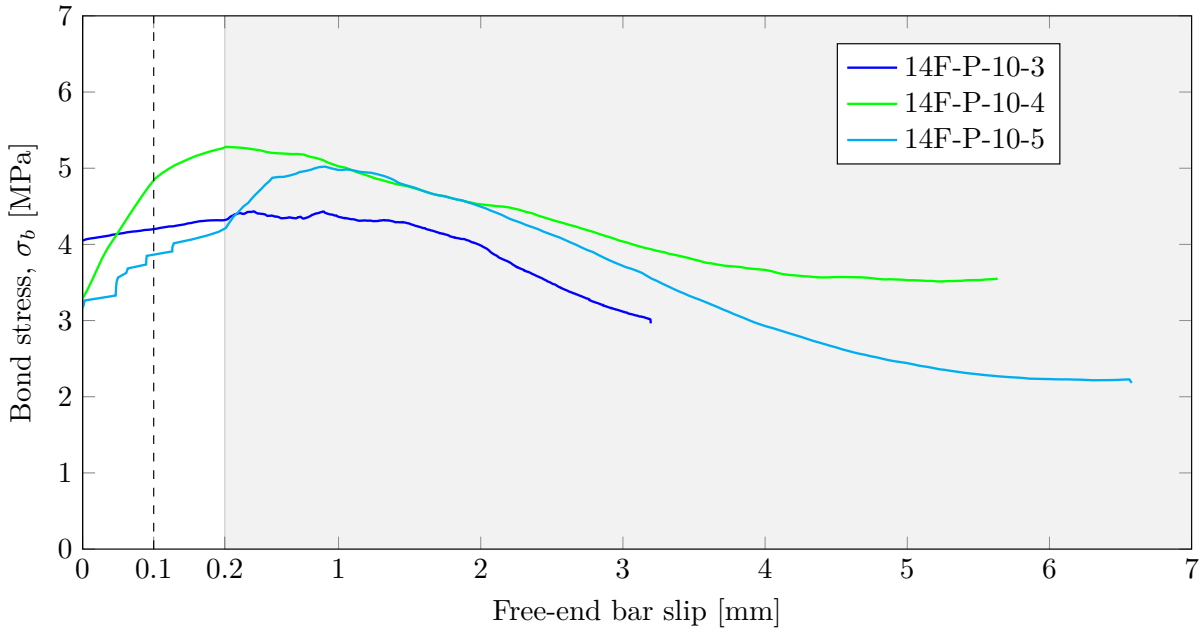

Figure 4.14: The uniform bond stress development versus free-end bar slip for 14F in the PO tests of Y10 bars. Free-end slip is enlarged between 0 and 0.2 mm. Compared to the 12F equivalent tests, these specimens exhibit better mechanical bond after the adhesion is lost, which can be attributed to the increase in relative rib area.

In Figure 4.14 the 4ϕ embedded length yields the largest design bond stress and the 5ϕ leads to the lowest design bond stress. Again, erratic patterns were observed for the various embedded lengths, though these measured data points do occur within a narrow margin of stress at very low magnitude compared to that found for NWC. A comparison between the envelopes of LWFC and NWC can be seen in Section 4.6.9.

Figure 4.15 shows the envelopes for the Y12 bars. The 14F-P-12-3 specimen yields the largest bond-slip envelope and the longer embedded length specimens yield lower design stresses. This resembles what was found for NWC and indicates increased susceptibility to splitting failure with increase in nominal bar diameter and relative rib area. Extrapolating this reasoning, the Y20 bars should then follow the same pattern, with the 14F-P-20-3 yielding the larger design bond stress. This was confirmed with the results as shown in Figure 4.16.

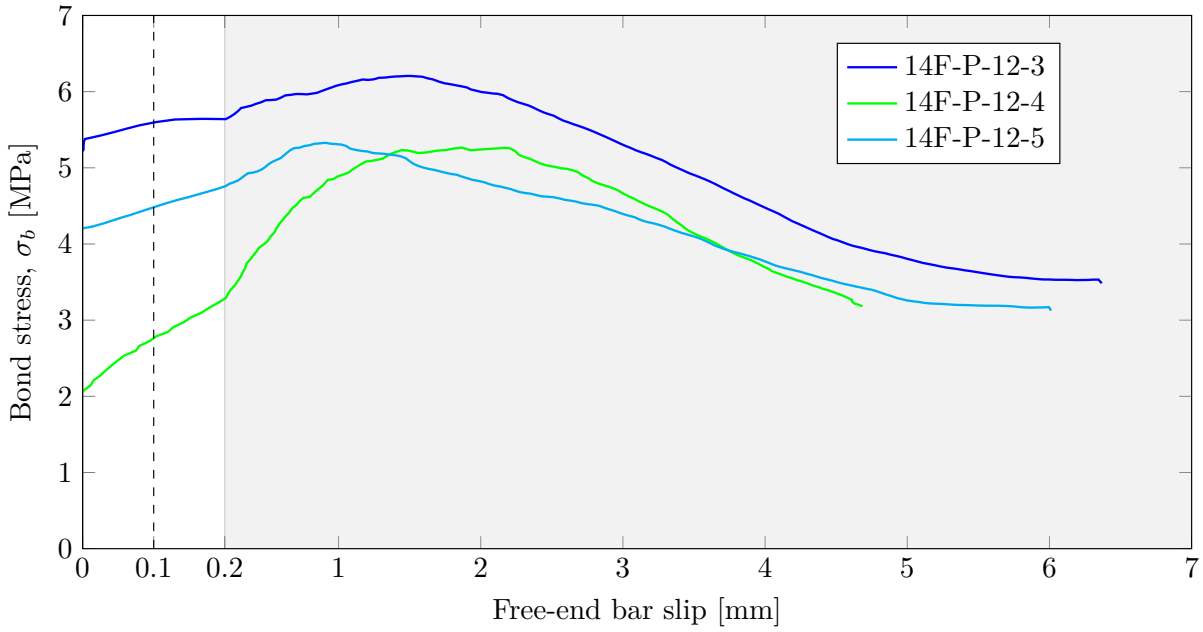

Figure 4.15: The uniform bond stress development versus free-end bar slip for 14F in the PO tests of Y12 bars. Free-end slip is enlarged between 0 and 0.2 mm.

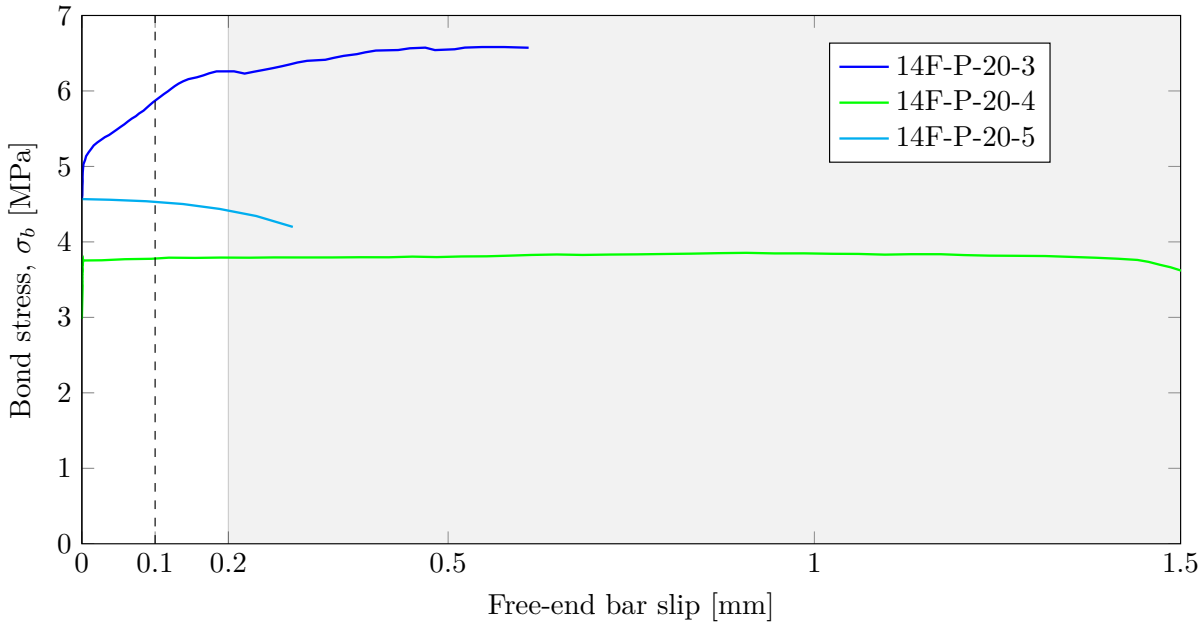

Figure 4.16: The uniform bond stress development versus free-end bar slip for 14F in the PO tests of Y20 bars. Comparing these envelopes to the 12F equivalent, show the 12F exhibiting pull-out failure at lowered magnitude, while the envelopes of this figure exhibit splitting failure at an increased bond stress magnitude.

Comparing the Y20 specimens of Figure 4.13 and Figure 4.16 it can be seen that the 1200 kg/m^3 LWFC pulled out as a result of low resistance to bearing failure, whereas the 1400 kg/m^3 LWFC failed in splitting as a result of increased resistance to bearing failure and brittleness.

4.6.8 Pull-out envelopes of 1600 kg/m^3 LWFC

All tests with 1600 kg/m^3 LWFC PO specimens terminated with splitting failure. This indicates that the tensile strength and onset of internal cracks governed the failure mode, even with the bars with smaller diameters (Y10 and Y12), which was not seen with the 12F and 14F LWFC PO tests. The 1600 kg/m^3 LWFC has only 15% air entrainment, which ensures a strong, yet brittle material. These findings are reported in Section 3.10 as the results from wedge splitting tests. This brittleness of the material does not allow for much elastic deformation and eventually leads to a large resistance when the bar ribs start to bear on the concrete. This in turn causes internal crack formation, which ultimately leads to a premature and sudden splitting failure.

Figures 4.17, 4.18 and 4.19 show the bond stress envelopes for Y10, Y12 and Y20 bars, respectively, all embedded in 1600 kg/m^3 LWFC. Moving from Figure 4.17 to 4.19, shows the decrease in ductile failures observed i.e. the increase in splitting failure. This relative decrease in ductile failure observed for increase in bar diameter again suggests that the two failure modes happen simultaneously as initially proclaimed in Section 4.6.2.

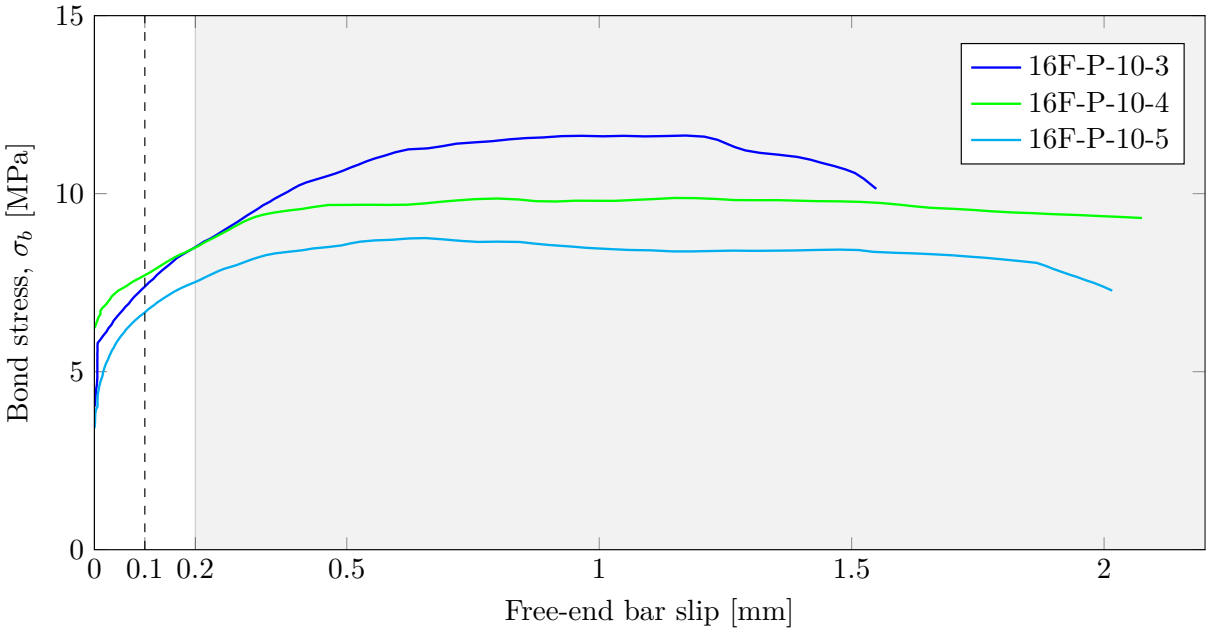

Figure 4.17: The uniform bond stress development versus free-end bar slip for 16F in the PO tests of Y10 bars. These tests were the only Y10 PO tests to fail in splitting failure and is attributed to the brittleness of increased density LWFC. Even though splitting failure is recorded, a ductile path is still observed.

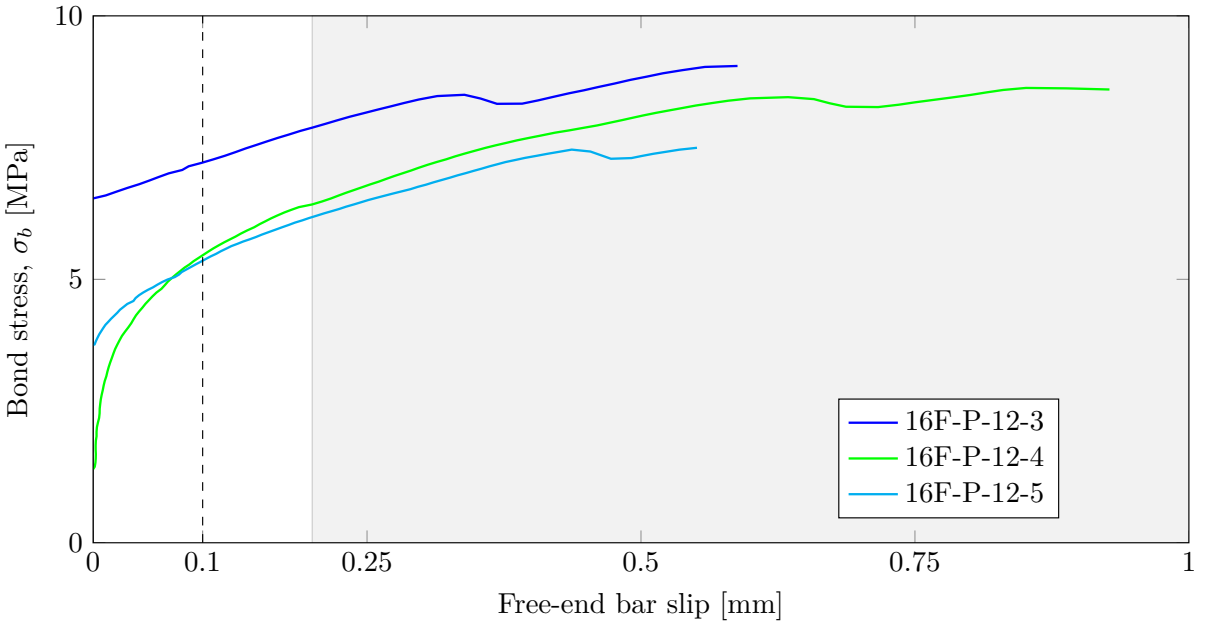

Figure 4.18: The uniform bond stress development versus free-end bar slip for 16F in the PO tests of Y12 bars. These tests were the only Y12 PO tests to fail in splitting failure and is attributed to the brittleness of increased density LWFC. This figure shows the Y12 exhibiting less ductile failure opposed to the Y10 specimens from Figure 4.17 above.

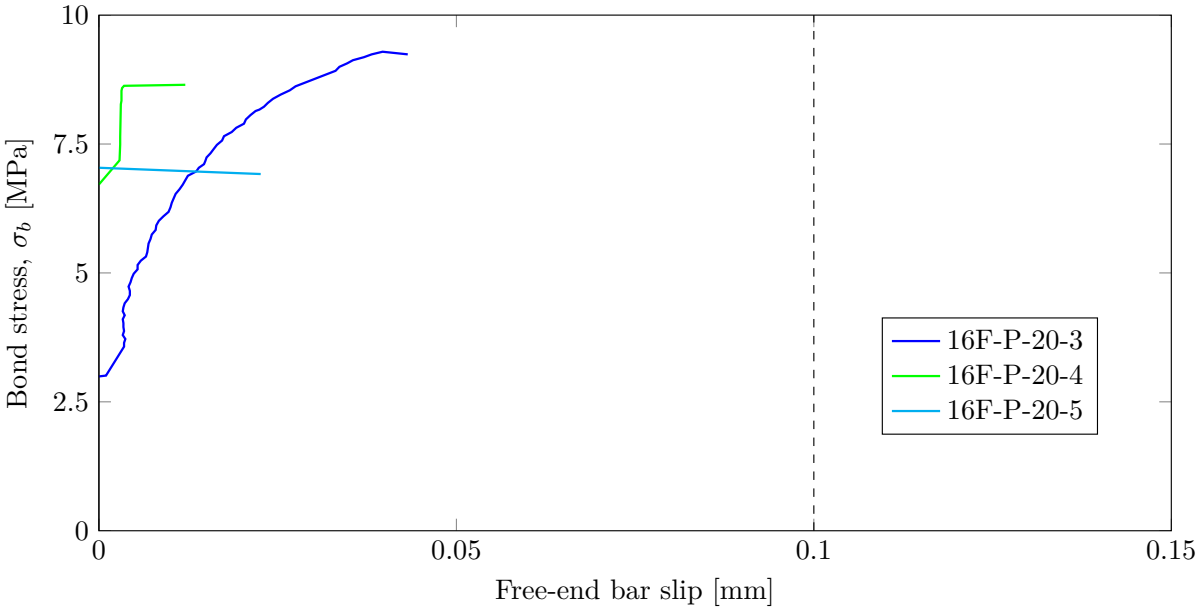

Figure 4.19: The uniform bond stress development versus free-end bar slip for 16F in the PO tests of Y20 bars. These tests showed the least ductile failure of all PO tests, all failing in spitting before reaching the design point.

The envelopes of the 16F specimens show the longer embedded length of 5ϕ yielding the lowest bond stress values for all rebar tested, which again points to the fact that longer embedded length causes secondary crack formation more readily. Although splitting failure is the result for all these tests, it still showed some ductility with the splitting failure, which decreases with increase in bar diameter tested. Figure 4.17 shows much more ductile failure of up to 2 mm slip for the Y10 specimens, the Y12 specimens of Figure 4.18 only show ductile failure up to 1 mm slip and the Y20 specimens of Figure 4.19 show almost no ductile failure with splitting occurring before the design point.

4.6.9 Comparison and conclusion of pull-out results

In order to better visualize the relative bond envelopes found for the various PO tests conducted, Figure 4.20 compares all the 4ϕ embedded length envelopes for the NWC and the range of LWFC, seen in Figures 4.8 to 4.19. The bond stress envelopes for LWFC are significantly lower than for NWC and the difference in failure behaviour is also prominent. When considering only the LWFC range (red, blue and green graphs) the average design bond stress (stress at 0.1 mm bar slip) is directly proportional to the density of the LWFC and inversely proportional to the ductility of the failure. This implies the 1200 kg/m^3 LWFC (shown in green) exhibits ductile behaviour at low bond stress and the 1600 kg/m^3 LWFC (shown in red) exhibits the least ductile behaviour at a higher bond stress. The NWC envelopes (shown in orange) show both ductile failure and significant bond stress magnitude, compared to the LWFC envelopes. This combination of ductile failure at large stresses has the best bond performance, which can be correlated to the area under the bond-slip envelope.

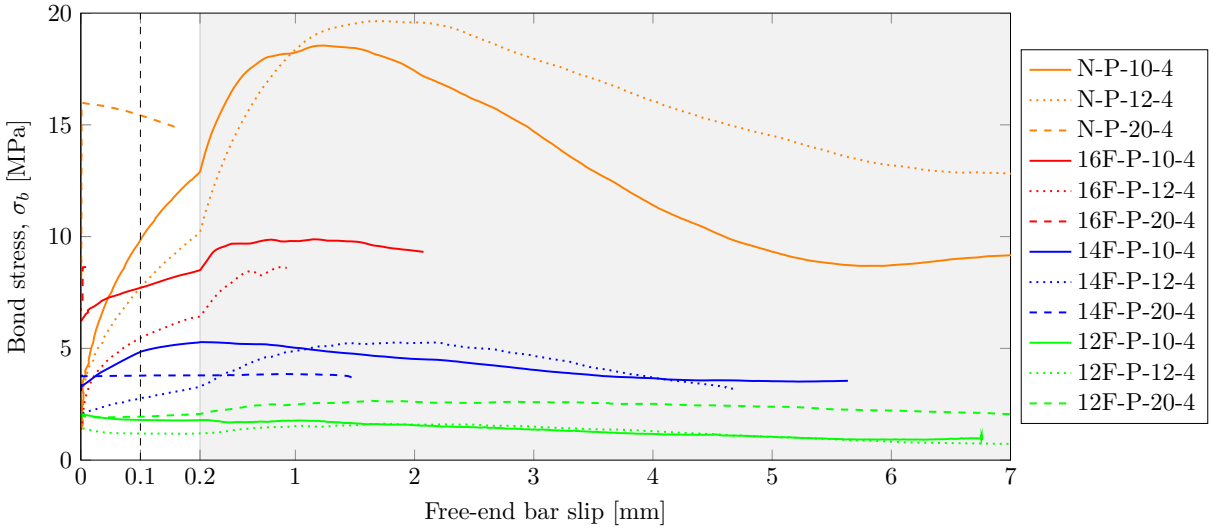

Figure 4.20: PO test bond stress envelope plots for the LWFC and NWC tested, for rebar sizes Y10, Y12 and Y20, embedded at a length of 4ϕ. These plots show the relative performance of LWFC, indicating the 12F with good ductility and poor magnitude and the 16F with good magnitude and poor ductility performance. The NWC has ductility and magnitude, surpassing the overall performance all the LWFC's.

The measured design bond stresses for tests of similar concrete type and bar diameter are averaged to yield a stress value (σ_d), which, from here onwards, will be used for further evaluation. The stress at which the adhesion is lost is indicated with σ_a, and is similarly averaged as was done for σ_d. These averaged stresses are listed in Table A2 in Appendix D.

The effect of the concrete cube compressive strength, and accordingly the density of LWFC, on the measured σ_d (solid markers) and σ_a (void markers) can be observed in Figure 4.21. This figure provides a direct proportionality and almost linear relation between σ_d and f_{cu}.

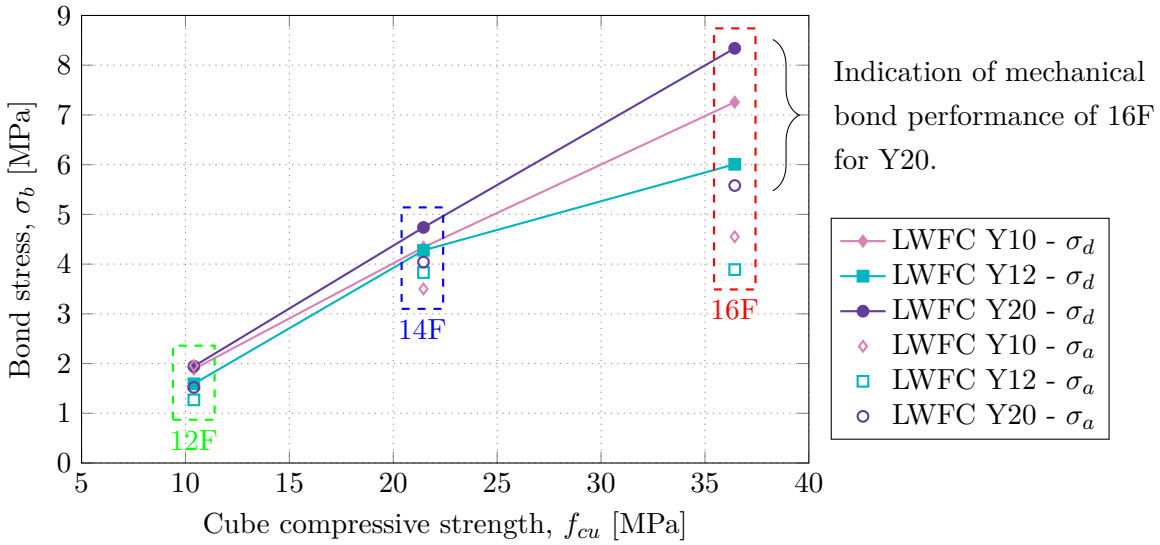

Figure 4.21: The measured design bond stresses (σ_d) and adhesion loss stresses (σ_a) of the PO tests of LWFC, averaged over the embedded lengths tested, are plotted against the corresponding compressive strength (f_{cu}). σ_d is shown in solid markers and σ_a in voided markers.

The σ_a for the LWFC's tested, relative to the accompanying σ_d provide a good indication of the bond performance between the instance of adhesion loss and the design point. The 1200 kg/m^3 LWFC, which is represented by f_{cu}-values near 10 MPa in Figure 4.21, shows a close spacing between σ_a and σ_d, which implies a weak mechanical bond response. On the contrary, the denser 1600 kg/m^3 LWFC yields larger differences, which imply better mechanical bond performance. The NWC PO tests, which σ_a and σ_d results are listed in Table A2 of Appendix D, yielded nearly the same adhesion stresses as the LWFC tests, but displayed larger differences in σ_a and σ_d, which as mentioned, imply good mechanical bond capacity. The physical condition of voids close to the steel concrete interface, which leads to reduced contact area, intuitively predicts that the 1200 kg/m^3 LWFC will have the lower adhesion loss stress, which is confirmed in Figure 4.21. With LWFC the porosity and dispersion of entrained air has a profound influence on the area of concrete in contact with the steel and thus the adhesion capacity.

A representative development length (l_d) can be derived from σ_d by using equation (4.3) in Section 4.6.3, which is an indication of the length of bar needed to fully anchor the bar in the LWFC's and NWC. The derived development lengths are represented in Figure 4.22, separately for each bar diameter tested and each concrete type.

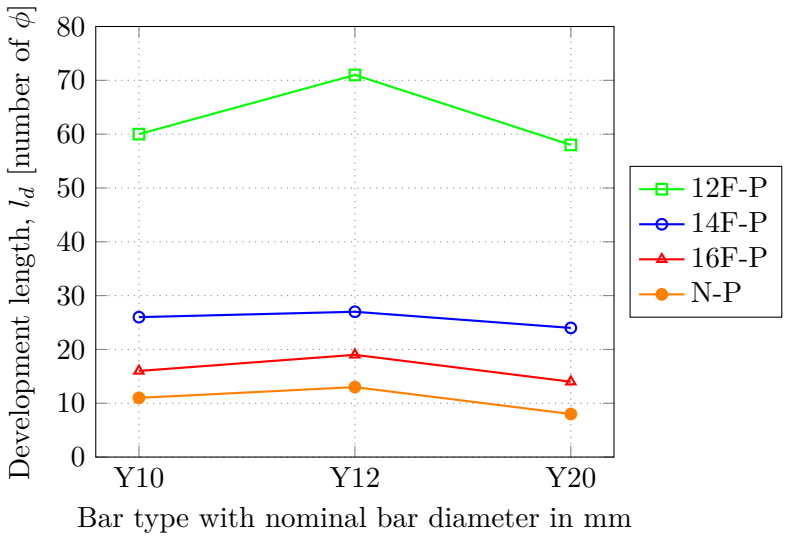

Figure 4.22: The development lengths required (in number of bar diameters) to develop yield stress in the various bar types embedded in the LWFC's and NWC, are derived from the average design bond stress (σ_d) obtained from PO tests. For derivation refer to equation (4.3) *in Section 4.6.3.*

For a Y12 bar embedded in NWC, 13 bar diameters or (156 mm) would suffice as an acceptable development length. The same bar embedded in 1200 kg/m^3 LWFC would need 71 bar diameters or 852 mm, 1400 kg/m^3 LWFC would need 27 bar diameters, and 1600 kg/m^3 LWFC would need 19 bar diameters, to transmit the yield force through the bond interface. These increased development lengths will influence the way in which the steel will have to be anchored in a structural application. Evidently, more steel and longer lap lengths will be required to obtain the same structural response from LWFC as in the case for NWC.

4.7 Beam-end tests

4.7.1 General

The measurement and analysis of data from the beam-end tests, where specimens are subjected to a complex loading state, provide another method for determining bond properties and yields results more representative of a reinforced structural member. A whole range of LWFC and NWC specimens were tested according to the specifications introduced in Section 3.12 on the BE test. Due to the size and weight of the specimen only the 5ϕ embedded length was studied. The shorter embedded lengths in weak concrete are, as mentioned before, more susceptible to damage during handling and initial installation of the BE specimen. The pull-out (PO) tests, discussed in Section 4.6, proved that a 5ϕ embedded length is sufficient for inducing splitting cracks. It also induced bond failure prior to connection failure, which is similar to what is explained in Section 3.11 for the conventional PO tests.

4.7.2 Recorded load fluctuations

The measured bar forces against the free-end and loaded-end slips for the BE test of specimen 12F-B-12-5, are presented in Figure 4.23. The data shows load variations, which initially start out with a relative small oscillation amplitude and change to larger peaks and drops, spiking at bigger intervals. For a better interpretation at the initial stage of rapid oscillations, Figure 4.24 shows the same test result for the free-end slip and the loaded-end slip from 0 mm to 0.2 mm.

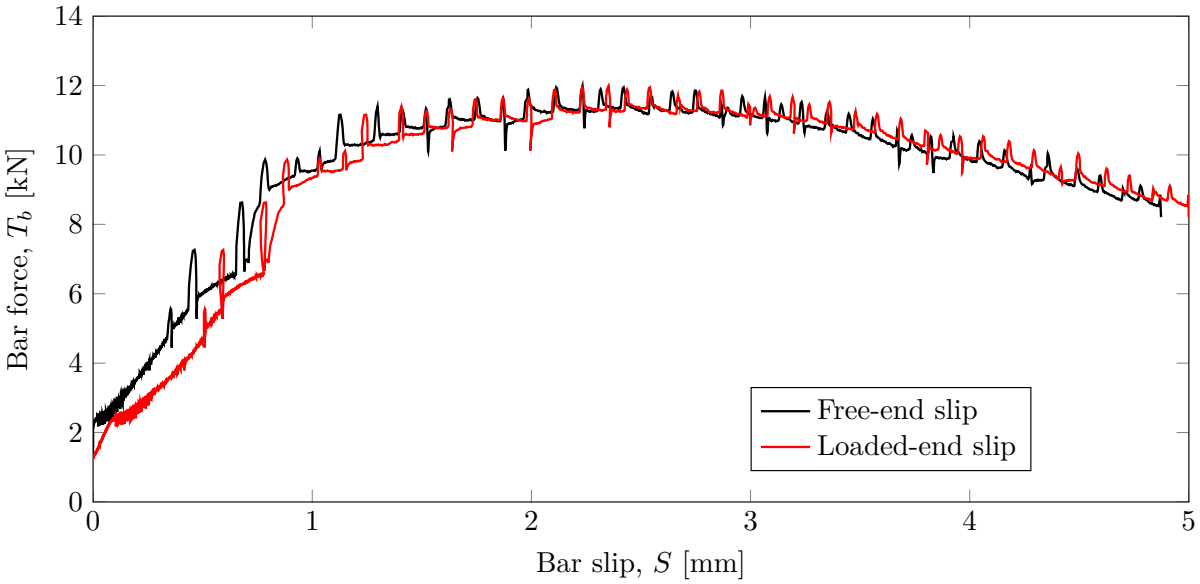

Figure 4.23: Bar load vs free-end and loaded-end bar slip for BE specimen 12F-B-12-5, indicating the load fluctuations during the BE test. This phenomenon is explained in Section 4.7.3.

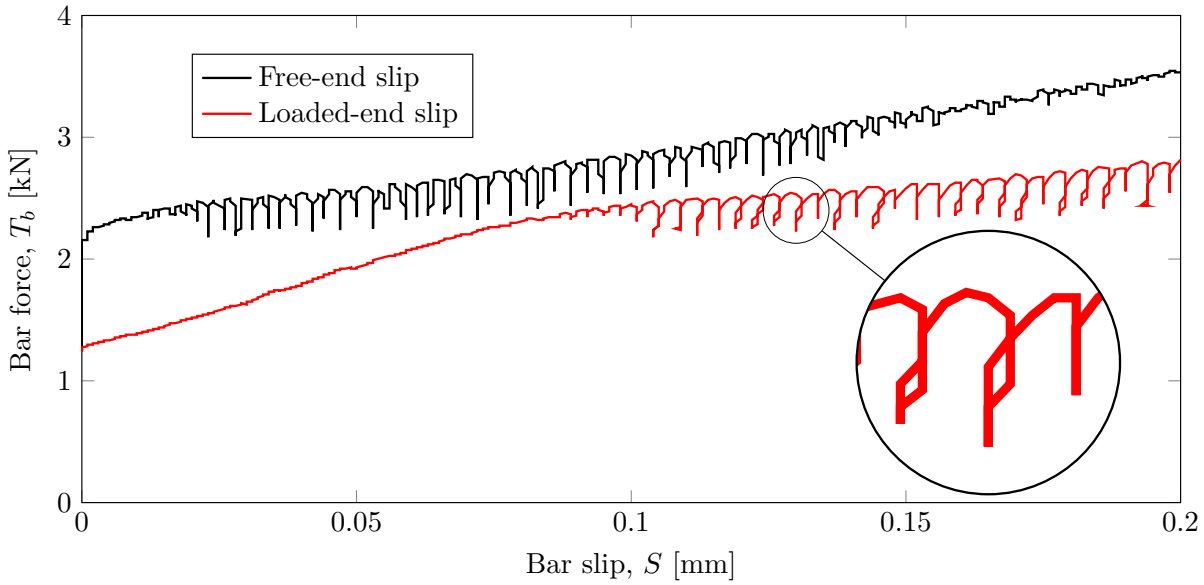

Figure 4.24: Bar load vs free-end and loaded-end bar slip from 0 mm to 0.2 mm slip of BE specimen 12F-B-12-5. The behaviour of the measured data in the enlarged insert is explained in Section 4.7.3.

4.7.3 Explanation of load fluctuations

At first the load fluctuations depicted in Figures 4.23 and 4.24, were interpreted to be a flaw in the control of the Instron testing machine, but soon led to the understanding that the nature of the test control has to show this variation in load application.

The BE tests were performed according to the methodology provided in Section 3.12.5 and the result of LVDT displacements against the testing time of specimen 12F-B-12-5 is presented in Figure 4.25. The initial loading rate of 0.001 mm/s was set on the Instron to automatically change to a new tempo of 0.01 mm/s after 0.8 mm loaded-end slip. In all BE tests the data was recorded at a fixed rate of 5 Hz and the quality of the timing control of the Instron can be derived from the linearity of the data in each of the segments. The practically perfect displacement control for the BE test procedure confirms the notion that the deviations in Figure 4.24 is connected to the breaking of the bond and not faulty test control.

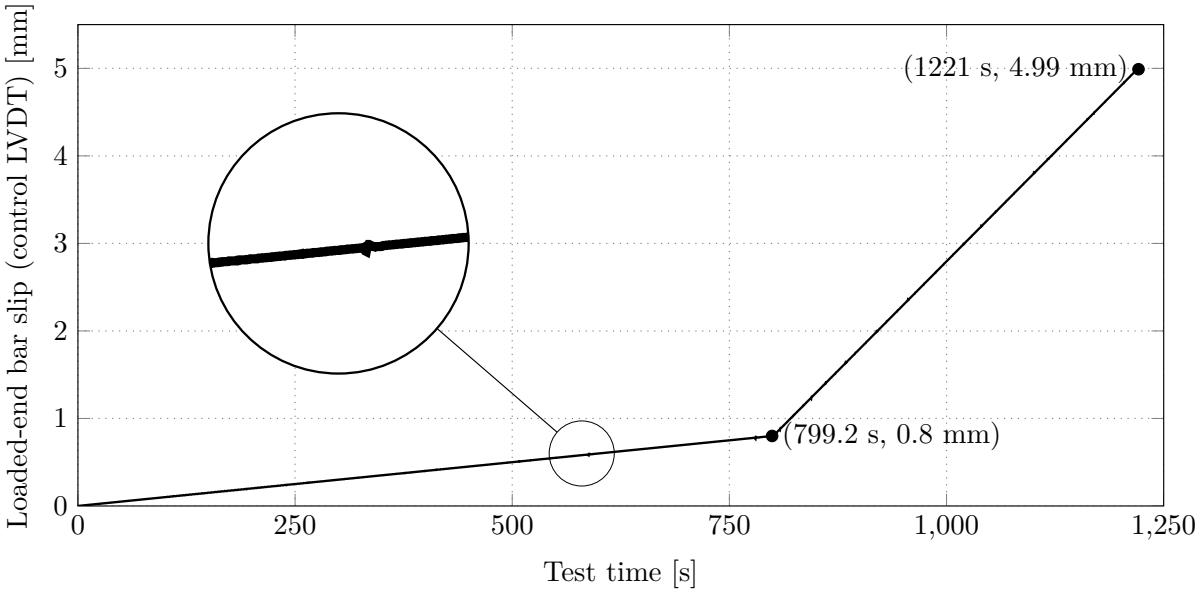

Figure 4.25: The accuracy of the tuned test control is shown graphically with the loaded-end LVDT measurement as a function of the test time. The displayed graph is a multitude of data points, collected at a constant rate of 5 Hz and the linearity of the sections indicate practically perfect displacement control. The gradients of the two sections refer to the preselected displacement rate of 0.001 mm/s that instantly changes to 0.01 mm/s after a preselected 0.8 mm of loaded-end slip is reached. This change in rate occurred after about 800 s. The magnified region of the graph gives an indication of one insignificant deviation blip in the data from the intended rate.

The magnified region in Figure 4.24 shows the loaded-end slip exhibiting an elastic response to the change in load application from the machine actuator. This elastic response is accompanied by the reverse of the loaded-end slip and implies that the bar is not elongating, but shortening at that specific times in the test procedure. This is explained in the sketch of Figure 4.26, depicting the two LDVT's (one each at the free-end and loaded-end) for slip measurements. The free-end LVDT measures the displacement of the bar relative to the underside of the concrete specimen. The loaded-end LVDT measures, relative to the top face of the concrete, the elongation of the bar at the point where it is fastened to the bar. This loaded-end measurement occurs as soon as loading commences, whereas the free-end slip only starts once adhesion is lost over the entire embedded length. At the earliest stage only the elongation of the bar contributes to the measurement reading at the loaded-end of the specimen. However, once the free-end measurement occurs (loss of adhesion is surpassed), the free-end slip is added to the loaded-end slip reading, which affects the bar slip control of the test. The increase in loaded-slip will have to be countered by releasing the applied force to a level where the prescribed rate of displacement is regained. For this reason sudden load drops occur and form an envelope which very accurately, and with precise control represents the bond-slip results of the structural member.

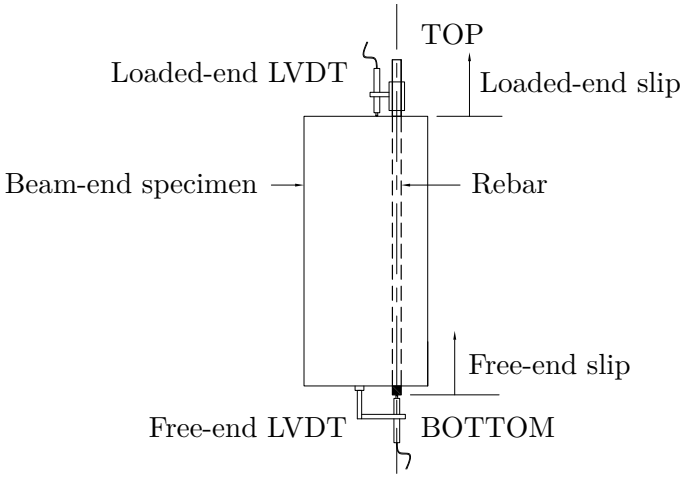

Figure 4.26: A schematic representation of the LVDT setup for the relative slip measurement at the free-end (bottom) and loaded-end (top) of the BE specimen.

It is also important to realise that up until the stage where the free-slip starts recording, the displacement is strictly dependant on the behaviour of the steel bar, which is predictable and easily used for the control setup of the test. After the free-end displacement starts, the control is dependent on a feed-back reading from the steel bar elongation and the bond loss mechanics associated with bearing and mechanical interlock. This process is unpredictable and non-uniform, and varies with different strengths (densities) of specimens.

This interpretation of the data and machine behaviour is further confirmed by the data in Figure 4.27, which shows the bar force and bar elongation plotted over an arbitrary selected part of the testing period of specimen 12F-B-12-5.

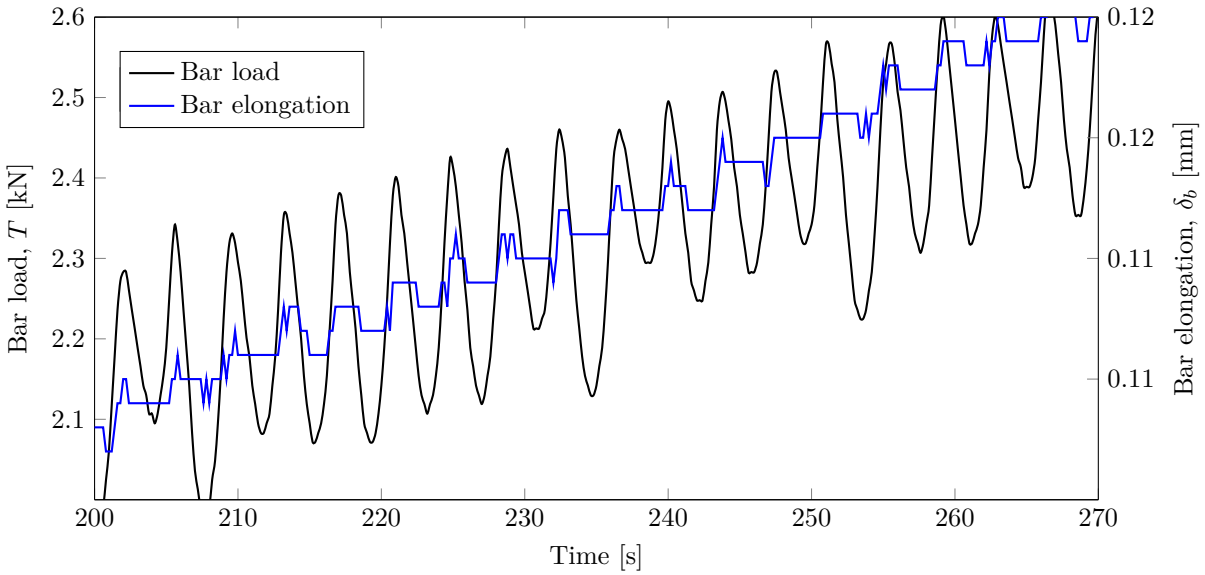

Figure 4.27: Bar load and elongation over an arbitrary time period within the test of specimen 12F-B-12-5, showing the bar elongation and shortening with the applied bar load during the BE test.

The elongation of the bar is the difference between the loaded-end slip and the free-end slip. It can be seen that for every drop in load there is an associated drop in bar elongation, or elastic shortening. When the load is applied to regain the required rate of loading the bar elongates again until the free-end slip contribution becomes too large and eventually removes the load again. This cycle is repeated, which yields the load drops seen in the beam-end tests results.

These fluctuations are therefore not included for the evaluation of the design bond stress (σ_d) values. An envelope is fitted to the data, which describes the bond behaviour and is then used for design bond stress readings and further evaluation. The design bond stress is obtained similarly to the PO tests and is explained in Section 4.6.3.

4.7.4 Beam-end envelopes for Y20 LWFC specimens

Figures 4.28, 4.30, and 4.32 show the resulting BE test bond stress envelopes for a Y20 bar embedded in each of the 1200 kg/m^3, 1400 kg/m^3 and 1600 kg/m^3 LWFC mixes and also indicate the crack width on a secondary vertical axis, in relation to the free-end slip. Figures 4.29, 4.31, and 4.33 include pictures of the respective failed BE specimens with secondary cracks visible on the concrete face over the embedded length. (Refer to Section 3.12 or Appendix C for the positions of these LVDT measurements on the specimen). It is important to remind the reader that this secondary crack measurement can only be recorded once the crack reaches the surface of the concrete and should therefore not be used as an indication of when the initial onset of the internal cracking at the bond interface occurred. It does however provide an indication of the crack growth and the aggressive nature of these secondary cracks for the various concrete specimens tested.

In the sections to follow a concise description of observed measurements of BE tests is reported and explained.

4.7.4.1 Specimen 12F-B-20-5

The BE test of 12F-B-20-5 resulted in the loaded-end (black line) and free-end (red line) slip envelopes observed in Figure 4.28 and they are almost identical. Since the bond stress (derived from the recorded bar load) is the common factor in the two envelopes, two data points of equal stress resemble the same point in the test time. For these envelopes to join and develop along the same path implies that the slip occurs at equal stress magnitude and testing time, which in turn suggests that the embedded Y20 bar was not restricted enough by the 1200 kg/m^3 LWFC to allow for the bar to elongate before free-end slip recording commenced. The failure is considered to be associated with a weak bond performance as a consequence of the crushing of the concrete in between the steel ribs and, eventually, the shear failure of the concrete keys in between the steel ribs.

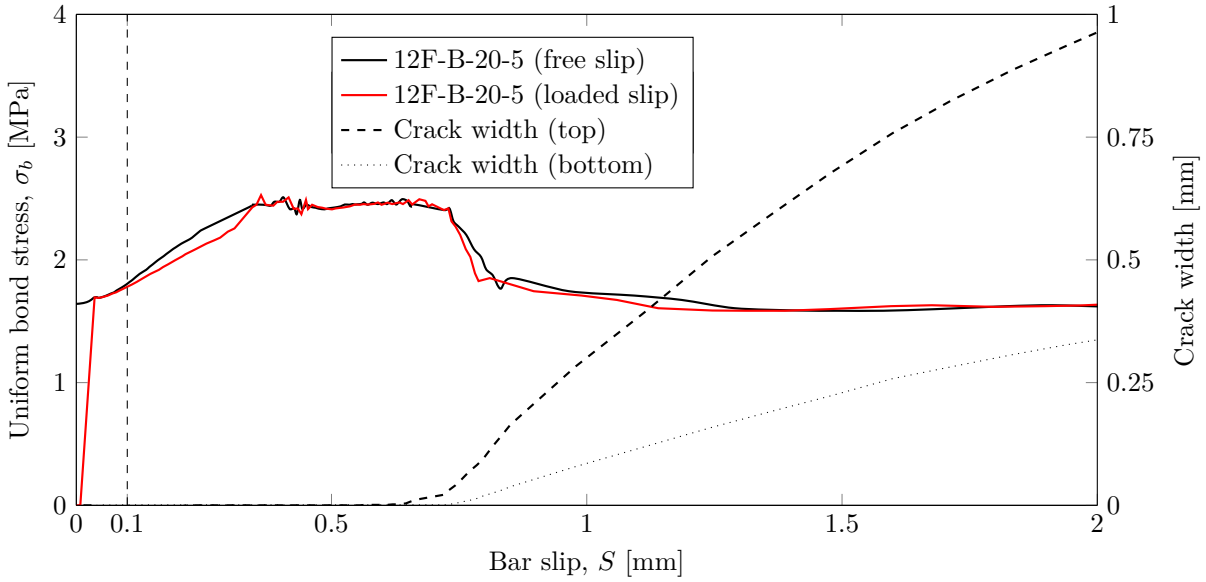

Figure 4.28: The beam-end bond-slip envelope for 12F-B-20-5 shows the free-end bar slip (solid black line) and loaded-end bar slip (solid red line) with almost identical paths. The crack growth is plotted on the secondary vertical axis, also against the free-end slip. The similar patterns of the loaded and free-end slip recordings are an indication of the poor bond resistance. The measured growth of the crack openings at the loaded and free-ends are respectively indicated with dashed and dotted lines.

Secondary crack measurements are also plotted in Figure 4.28 and a photograph of the specimen after testing is shown in Figure 4.29. The surface of the specimens was painted with a chalk based mixture for easier visual inspection for cracks. The secondary crack opened along the embedded bar and is wider at the loaded-end of the specimen, which opened up to a maximum width of just under 1 mm. At the free-end of the embedded length a transverse crack is observed (perpendicular to the secondary crack), which occurred at the point where the bonded length changes into the un-bonded region. These cracks can be considered as primary cracks. At the point where primary cracks, or flexural cracks, in structural members occur, the tensile forces are transferred to the steel reinforcement since bond can not exist in the crack region. Immediately adjacent to this crack the steel concrete interface is dealing with the tensile forces and therefore needs bond to ensure structural performance. This structural mechanism is simulated by the beam-end test and the occurrence of these primary cracks at the embedded length boundary confirms the effective debonding measures used. Primary cracks are shown in the photographs of the 1200 kg/m^3, 1400 kg/m^3 and 1600 kg/m^3 Y20 BE specimens in Figures 4.29, 4.31 and 4.33 respectively.

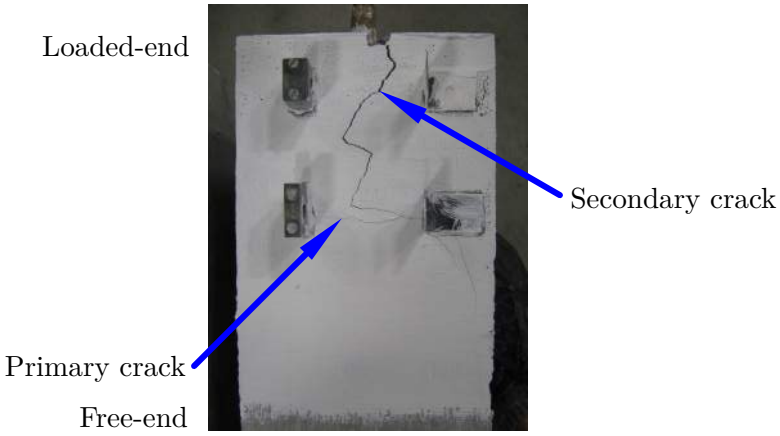

Figure 4.29: Photograph of the failed 12F-B-20-5 specimen with secondary cracks visible. Primary cracks can also be seen at the free-end side of the embedded length, suggesting good debonding measures and structural loading.

The obvious governing failure of specimen 12F-B-20-5 (above) is splitting failure, but some bond resistance was regained after the secondary crack reading started, showing the typical behaviour of a pull-out failure mode. This is similar to the bond deterioration observed with the 1200 kg/m^3 PO specimens in Section 4.6, with ductile failure envelopes for all embedded lengths and rebar diameters tested. The equivalent PO test of this BE test terminated without any secondary cracks. This furthers the notion that pull-out and splitting failure exist in combination, as introduced in Section 4.6, and that the BE test yields more critical (conservative) results due to the fact that the same configuration in both tests leads to splitting in the BE and pull-out in the conventional PO tests. This increased critical bond recordings can be attributed to the bar being loaded at an eccentricity in the BE specimen, which causes the bar to bear on one side of the bond interface, effectively forcing longitudinal cracks in addition to the transverse force exerted from the steel ribs. A comprehensive comparison between the pull-out and beam-end test is done in Chapter 5.

4.7.4.2 Specimen 14F-B-20-5

The denser 1400 kg/m^3 LWFC was subjected to the same test and loadings as done for specimen 12F-B-20-5, introduced above. The resulting envelopes of the recorded bond stress versus, respectively, loaded-end slip and free-end slip are shown in Figure 4.30. This figure indicates two distinct paths of the envelopes implying that, unlike the 1200 kg/m^3 specimen, sufficient bond resistance was provided causing substantial elongation of the steel rebar before any free-end slip occurred. The elongation of the bar up to the point where the free-end recording commences serves as a good indicator of the bond integrity and resistance. A comparison of the 12F-B-20-5 and 14F-B-20-5 tests shows that the 1400 kg/m^3 has a better bond performance when considering the magnitude of its recorded bond stress, but does terminate in a sudden loss of bond stiffness; splitting failure. The sudden drop in bond stress, moments after the design point, suggests a high level of failure due to brittleness of the 14F-B-20-5 specimen. The conventional PO tests for the equivalent test also yielded splitting failure.

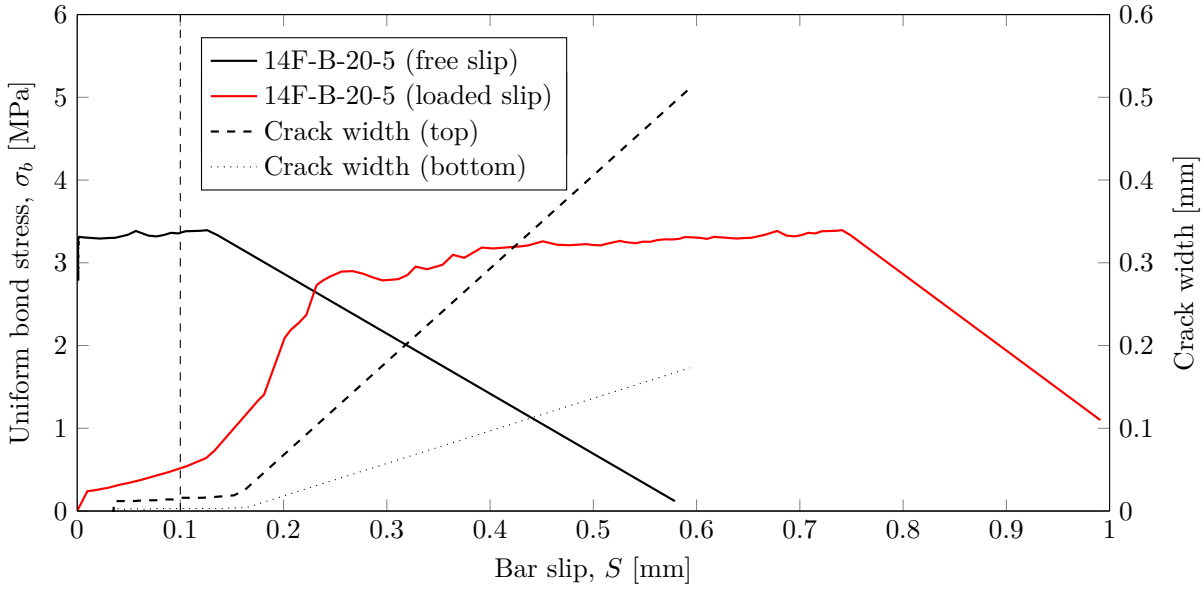

Figure 4.30: The beam-end bond-slip envelope for 14F-B-20-5 shows the free-end bar slip (solid black line) and loaded-end bar slip (solid red line). The crack growth is plotted on the secondary vertical axis, also against the free-end slip. This specimen showed bond resistance by inspecting the bond stress magnitudes and the substantial difference in loaded and free-end slip envelopes. The measured growth of the crack openings at the loaded and free-ends are respectively indicated with dashed and dotted lines.

Figure 4.31 shows the splitting cracks after testing 14F-B-20-5, which provides similar results as seen for the specimen 12F-B-20-5. The crack opened up to a maximum of 0.5 mm, half of what is recorded for the 12F equivalent specimen.

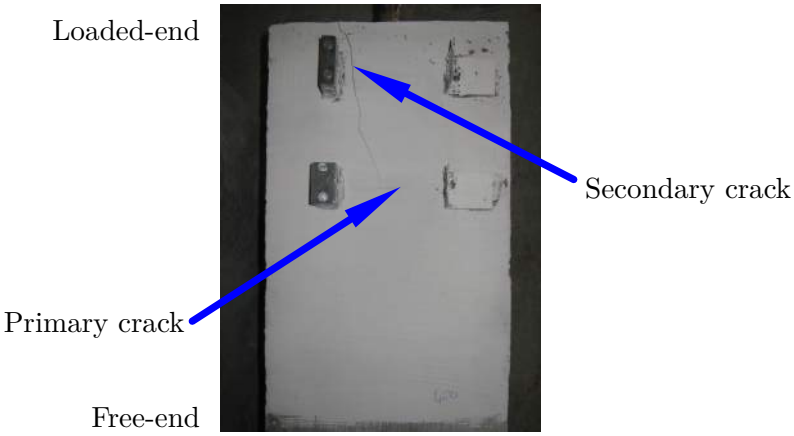

Figure 4.31: Photograph of the failed 14F-B-20-5 specimen with secondary cracks visible. Primary cracks can also be seen at the free-end side of the embedded length, suggesting good debonding measures and structural loading.

4.7.4.3 Specimen 16F-B-20-5

The same brittleness characteristic property and failures were observed for all 1600 kg/m^3 LWFC beam-end specimens, similar to what was obtained with the conventional PO tests in Section 4.6.

Figure 4.32 shows the envelopes for the bond stress as a function of the loaded and free-end slip measurements. These envelopes are also identified with sudden load drops, implying splitting failure, which is confirmed with the recorded crack opening reaching a maximum of 0.8 mm. The photograph in Figure 4.33 indicates the longitudinal secondary crack for this specimen. Like the 14F, and unlike the 12F equivalent test, the bond interface provided enough resistance to allow bar elongation before the first free-end slip was recorded.

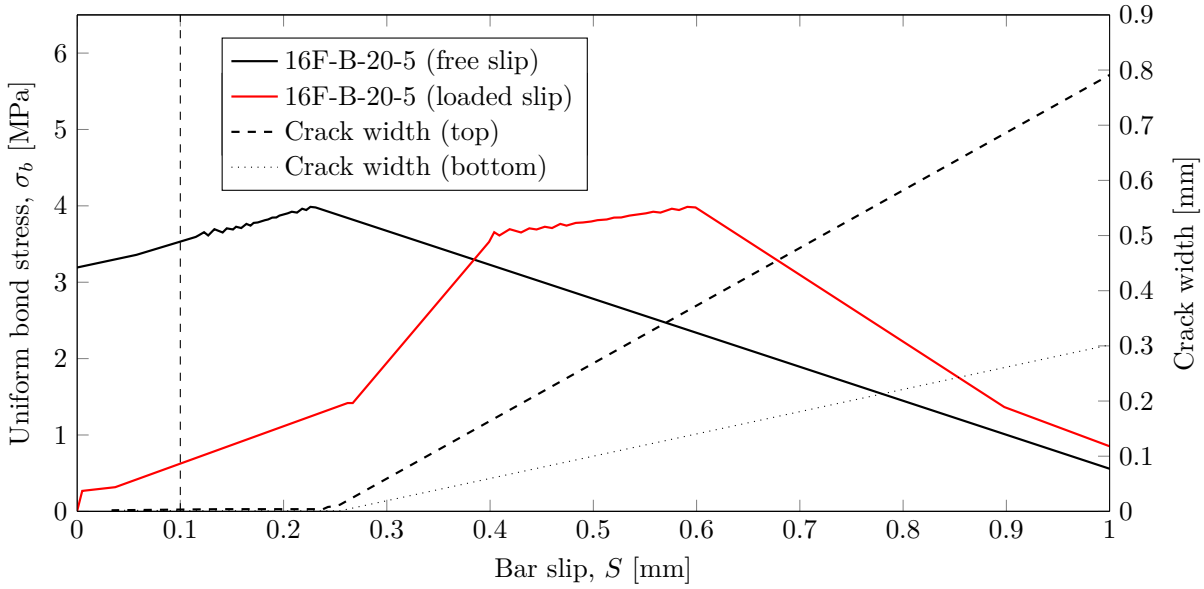

Figure 4.32: The beam-end bond-slip envelope for 16F-B-20-5 shows the free-end bar slip (solid black line) and loaded-end bar slip (solid red line). The crack growth is plotted on the secondary vertical axis, also against the free-end slip. The measured growth of the crack openings at the loaded and free-ends are respectively indicated with dashed and dotted lines.

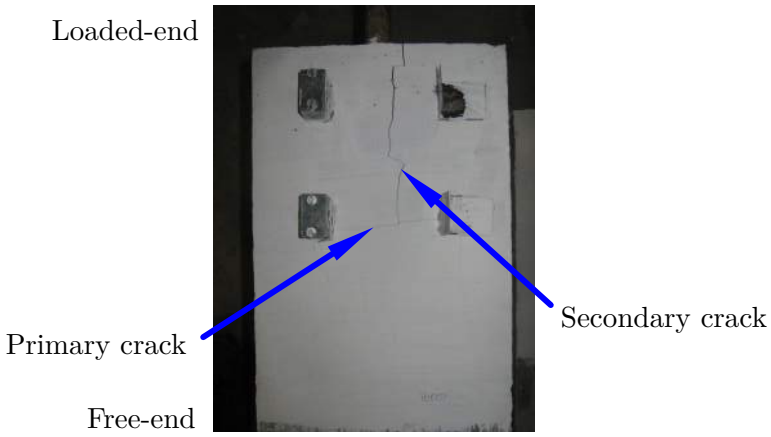

Figure 4.33: Photograph of the failed 16F-B-20-5 specimen with secondary cracks visible. Primary cracks can also be seen at the free-end side of the embedded length, suggesting good debonding measures and structural loading.

The most likely explanation for the bonding failures is the brittleness of the 1600 kg/m^3 LWFC, which ensures early internal cracks and eventually earlier loss of adhesion and therefore loss of bond and free-end slip.

4.7.4.4 Comparison of Y20 beam-end tests

Figure 4.34 compares the bond-slip envelopes measured for 12F-B-20-5, 14F-B-20-5 and 16F-B-20-5, introduced above in Figures 4.28, 4.30 and 4.32, respectively. The 1600 kg/m^3 LWFC has the largest design bond stress and the 1200 kg/m^3 LWFC the lowest. The design points for 16F-B-20-5 and 14F-B-20-5 are nearly the same and a feasible explanation for this similarity in the design bond values is that the more brittle 1600 kg/m^3 LWFC provides more resistance and therefore attains a higher bar force (larger stress), but on the contrary forms internal cracks much more readily, which compromises the bond integrity and effectively lowers the bond force developed. All the specimens failed in splitting failure, but in varying degrees of splitting intensity. The relative ductile failure behaviour of 12F-B-20-5 at a relatively low magnitude can also be observed in the figure. The lighter LWFC exhibits excellent ductile behaviour at low magnitude in bond stress, whereas the denser LWFC exhibits better bond stress magnitude, but lacking ductility.

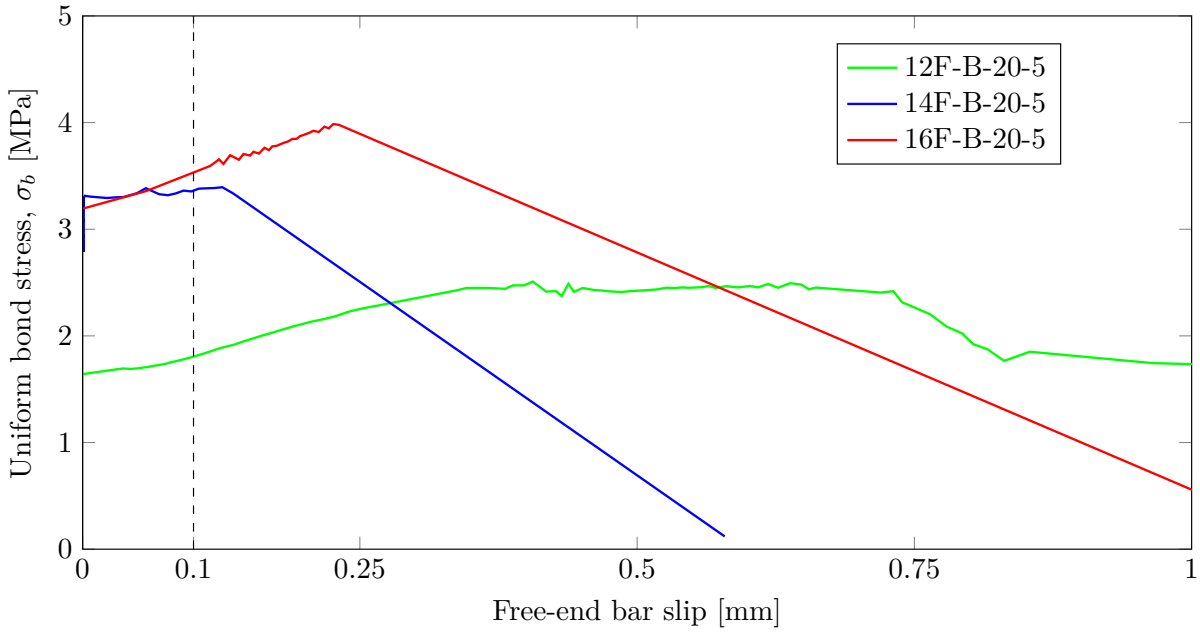

Figure 4.34: The measured bond performances with BE tests on the range of Y20 specimens (12F-B-20-5, 14F-B-20-5 and 16F-B-20-5), are compared to the free-end bar slip. The 12F specimen showed ductile failure at a low magnitude, whilst the denser LWFC showed more brittle failure at a higher magnitude of bond stress. These results are similar to what was obtained for the equivalent PO tests.

The rate at which the secondary cracks propagate, provides a useful indicator of the brittleness associated with the LWFC specimen. In order to obtain a measure of the brittleness of the LWFC, the crack opening measurements are plotted versus the testing time period for the specimens and the top crack opening of specimen 12F-BE-20-5 is shown in Figure 4.35. Here the 1200 kg/m^3 LWFC exhibits ductile splitting failure with the crack opening at an average rate of 0.0033 mm/s.

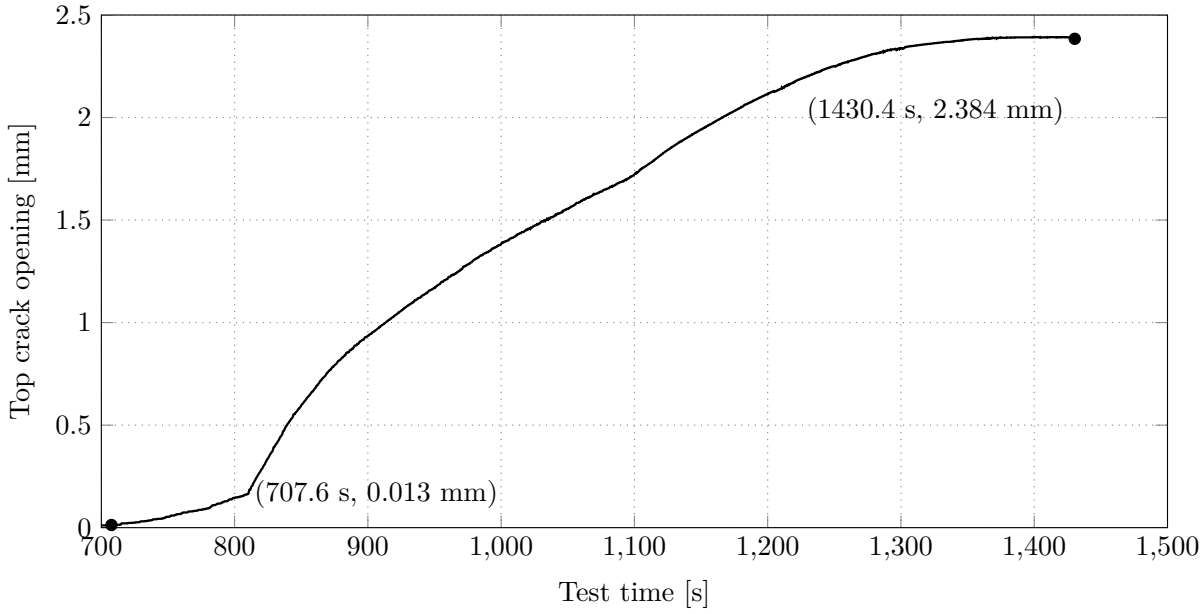

Figure 4.35: The graph shows the crack opening versus the testing time of 12F-BE-20-5 as an indication of the rate of internal crack propagation. This 12F specimen exhibited relatively slow crack opening (ductile failure) at an average rate of 0.0033 mm/s.

On the contrary, specimen 14F-BE-20-5 has a much larger rate of crack opening compared to 12F-BE-20-5. Figure 4.36 shows that it opened at a rate of 1.335 mm/s, which indicates the effect of the larger brittleness of 1400 kg/m^3 LWFC.

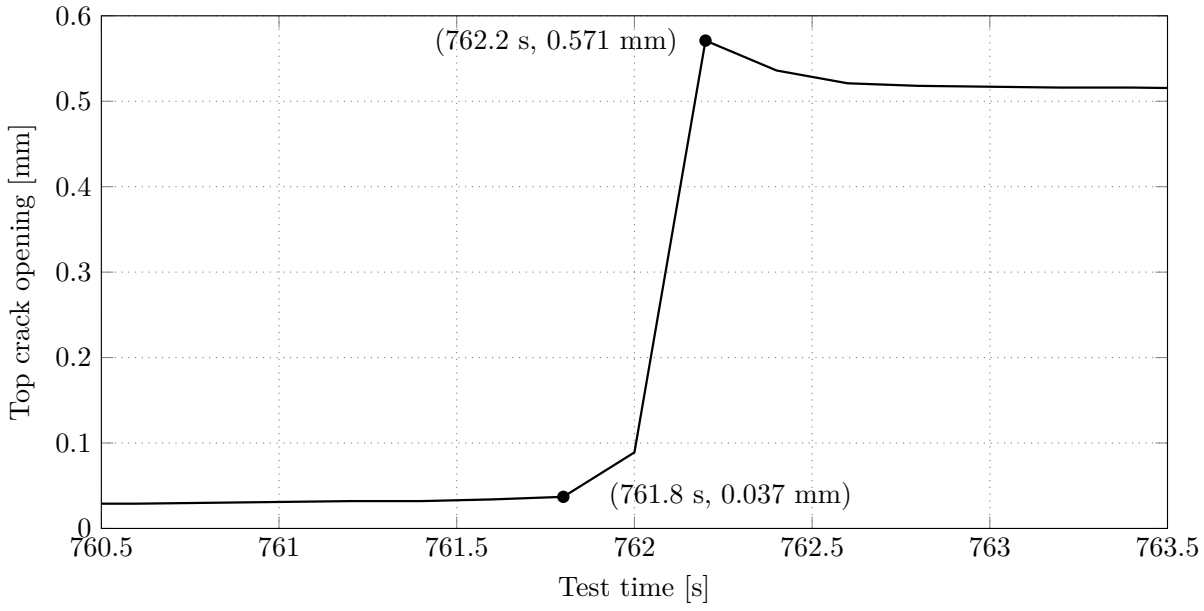

Figure 4.36: The graph shows the crack opening over the testing time of 14F-BE-20-5 as an indication of the rate of internal crack propagation. This 14F specimen exhibited relatively fast crack opening at an average rate of 1.335 mm/s, implying a more brittle material.

Figure 4.37 shows an even greater rate of crack opening for specimen 16F-BE-20-5 at an average rate of 2.18 mm/s. This relative indication of brittleness again points to the fact that the density of LWFC is proportional to te brittleness of the concrete.

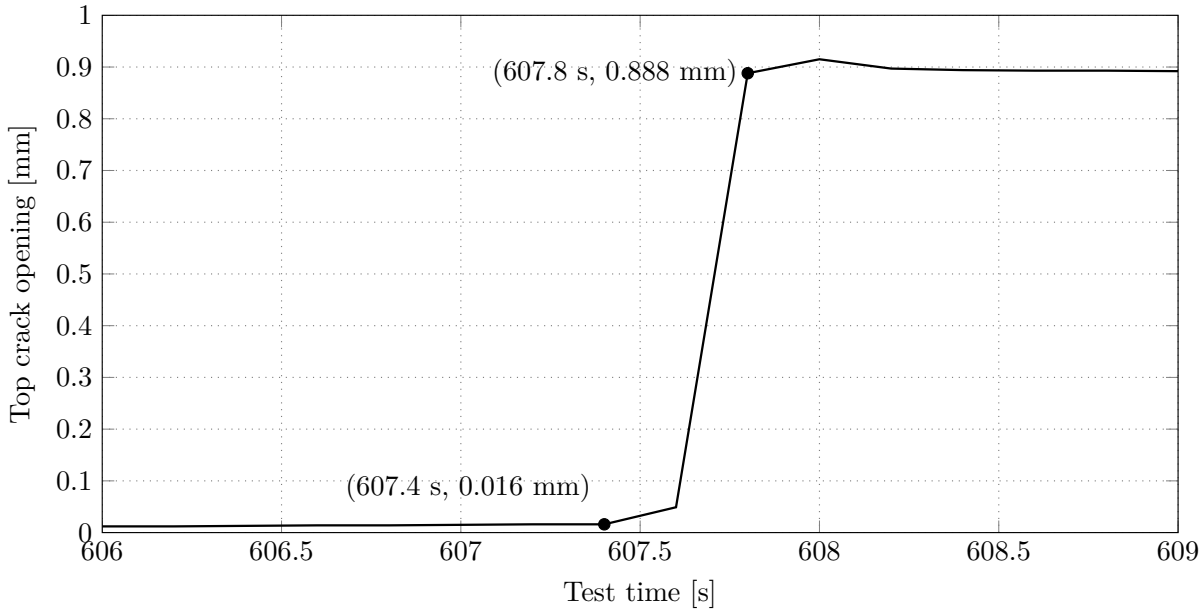

Figure 4.37: The graph shows the crack opening over the testing time of 16F-BE-20-5 as an indication of the rate of internal crack propagation. This specimen showed the fastest crack opening at an average rate of 2.18 mm/s, implying that 16F is the most brittle of the range of LWFC's.

4.7.5 Beam-end envelopes for Y12 LWFC specimens

The exact same test procedure as for the Y20 specimens in Section 4.7.4, was applied to the BE tests for the specimens with Y12 testing bars. The resulting bond stress envelopes for 12F-B-12-5, 14F-B-12-5 and 16F-B-12-5 are compared in Figure 4.38, where all Y12 specimens failed in pull-out failure with no secondary crack measurements recorded.

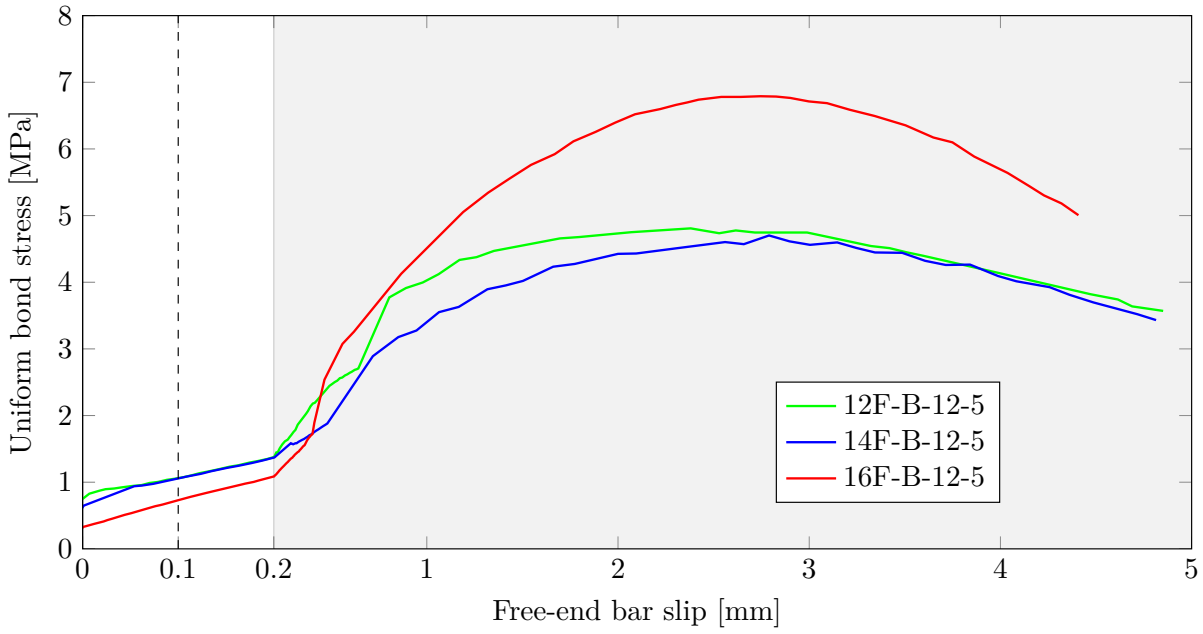

Figure 4.38: Beam-end bond-slip envelopes for all LWFC Y12 BE specimens, indicating that the 16F specimen has the worst bond performance at the design point. The region from 0 to 0.2 mm slip is on a different scale than the rest, for better visualization of the data at the design point.

For the initial part of the test (from 0 mm to 0.1 mm) the bond stiffness and design bond stress is almost the same for the 12F-B-12-5 and 14F-B-12-5 specimens, but the denser 16F-B-12-5 specimen yields a much lower design bond stress. This is unlike what has been seen previously with the conventional PO tests of 1600 kg/m^3 LWFC. However, when viewing the gradients of the plots within this section, it can be seen that the 16F-B-12-5 has a larger bond-slip gradient. This implies that there must be some factor that compromises the adhesion capacity of the bonded system during the early stages, which is only present (or more susceptible) in the 1600 kg/m^3 concrete and intensified for the BE test.

This early compromise of bond integrity for the denser LWFC is attributed to the brittleness of the material and the formation of internal secondary cracks. The results from the wedge splitting tests reported in Section 3.10, confirms the direct proportionality of brittleness and density of LWFC. This phenomenon is not seen in the conventional PO tests. The BE test subjects the specimen to a moment and thus loads the bar at an eccentricity, which induces greater stress on the side of the concrete. This forces the bar to bear on one side of the bond interface while slipping in the axial direction. In a brittle material this stress action will destroy the adhesion as a result of internal cracks much earlier than a more ductile material. This occurrence ensures more concentrated stresses and can be compared to the analogy of the reactions of an elastomeric bearing pad that is typically used in bridge construction.

A soft rubber bearing pad, supporting a concrete beam, will allow some form of rotation and consequently ensure an almost uniform reaction force distribution across the support. A hard rubber will show much more resistance to any rotational movement and consequently force more reaction stress to the leading edge of the rubber bearing. This action forces the reaction

distribution from a uniform state to a scew distribution, which ultimately induces a larger stress concentration. In this analogy the hard rubber represents the denser concrete and provides much resistance without any elasticity, while the soft rubber corresponds to the less dense LWFC, which allows more movement once the bar starts to bear on the one side of the embedded length.

Towards the end of the test the 16F-B-12-5 specimen developed the largest peak, which suggests that when the bearing occurs and the material is crushed in between the ribs, the denser concrete ensures a larger peak stress, because there is more material to wedge between the steel ribs and less voids to result in slip. During these tests no secondary cracks occurred at the surface, but this serves as a good example to show that these failures exist in combination as well. Pedziwiatr (2008) mentions that typically bond tests are conducted with simple PO tests and the effect of secondary cracks is not well catered for. It is stated that although these internal secondary cracks are not visible they change the strain distribution along the embedded bar, which influences the bond.

4.7.6 Bond Integrity

The loadings present in the BE specimen during testing was introduced in Section 3.12.4. Any reinforced structural member subjected to a bending moment, is in a state where the reinforcing is loaded at an eccentricity and thereby introduces a bending moment on the bar. The bond resisting this bending moment is the so-called flexural bond (Park and Paulay, 1975). The BE specimen can simulate flexural bond, as opposed to the conventional PO tests that only loads the reinforcing axially. It is stated by Park and Paulay (1975) that bond integrity is intact whenever the rate of change in the internal tension force (T) in the bar equates the rate of change of the external bending moment (M). Equation (4.4) provides the test for flexural bond in mathematical terms, with T the internal tension in the bar, M the external bending moment on the specimen, t the test time and jd the lever arm over which the external applied bending moment is applied to load the embedded bar.

$$\frac{dT}{dt} = \frac{\frac{dM}{dt}}{jd} \tag{4.4}$$

It can therefore be stated that when the rate of change in the internal tension and external bending moment starts to deviate, it implies bond deterioration. The BE tests of this section were all done at the same displacement rate and therefore the bond interface integrity be quantified using equation (4.4). Any deviation from this equality during testing will be an indication of bond deterioration. It is however important to realise that at any specific moment within the test procedure, two comparing tests do not necessarily yield the same bar load, or applied moment. It should therefore be carefully interpreted within a test and not compared between tests. The only parameter that occurs at the same time is the loaded slip, which is used as the control for the BE test.

The Bond Integrity (BI), in Newton per second, is defined with equation (4.5) to gauge the

equilibrium state given by equation (4.4).

$$BI = \frac{\frac{dM}{dt}}{jd} - \frac{dT}{dt} \tag{4.5}$$

Any non-zero value of BI indicates a difference in the applied moment rate and measured bar load rate.

Once the BE test starts and the bond interface is in perfect condition, the two rates will be exactly the same and BI is zero. Once any factor, like internal cracks and bearing failure, starts to compromise the bond interface and allow slip, the recorded bar load will drop. This drop implies a lower rate for $\frac{dT}{dt}$, which results in a positive BI reading. This change in rate is associated with some slip/bond deterioration, which is then interpreted by the displacement control and the applied moment is adjusted accordingly, until the equilibrium is restored. The cycle then repeats.

To conclude then, any bond deterioration associated with compromising factors will lead to a positive BI reading, whereas the readjustment of the machine control could overshoot and result in a negative BI reading. The magnitude of the readings of BI can directly be correlated to how hard the machine control has to work in order to regain the required rate of displacement after bond loss. The effect of the free-end slip measurement on the machine control and resulting bond envelope are explained in Section 4.7.3.

4.7.6.1 Bond integrity of beam-end LWFC specimens with Y12 bars

Figure 4.39 shows the BI plotted over the testing time for the Y12 beam-end tests, with the BI conforming around zero with positive and negative spikes indicating loss of bond integrity. For easier identification and correlation with the measured data, the occurrence times of the adhesion loss point (solid circle) and design point (circle) for the various LWFC's, are inserted on the time scale axis. These times are also listed in Table 4.5.

The first conclusion from this data is the relative positions of adhesion loss and design point. For the 1200 kg/m^3 and 1600 kg/m^3 the adhesion point occurs relatively quickly after test initiation, with the 16F-B-12-5 specimen showing almost immediate loss of adhesion. This resembles and supports the brittle nature of this dense LWFC.

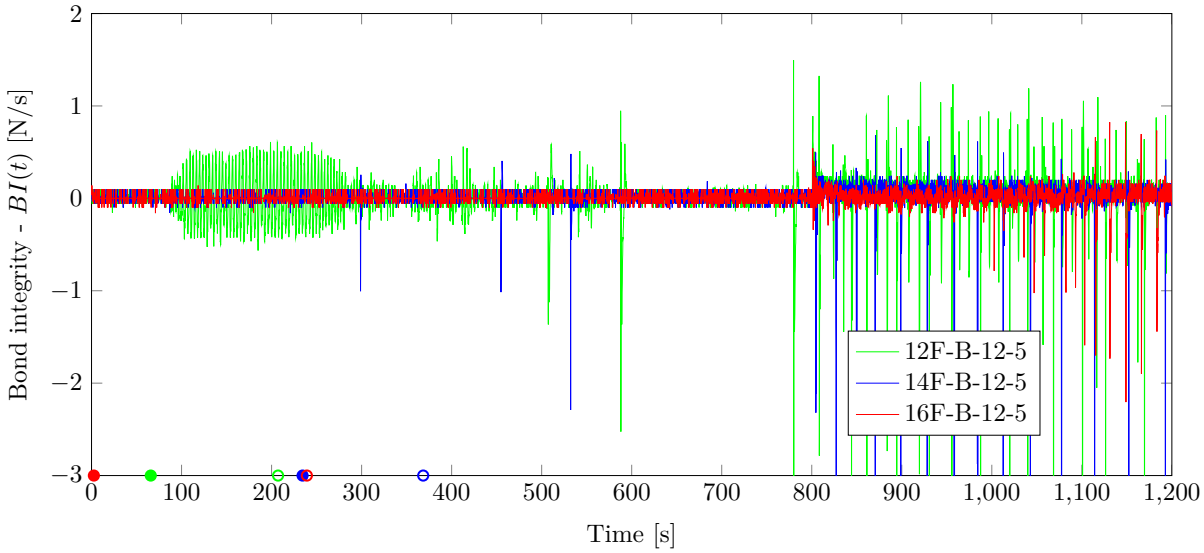

Figure 4.39: Bond integrity (BI) plotted against the beam-end testing time for specimens 12F-B-12-5, 14F-B-12-5 and 16F-B-12-5. The adhesion lost points (solid circle) and design point (circle) occurrences are marked on the horizontal axis for easy correlation with the displayed data.

Table 4.5: Adhesion loss and design point time occurrences during the Y12 BE tests.

Specimen	Adhesion loss time [s]	Design point time [s]
12F-B-12-5	65.8	207.2
14F-B-12-5	234.4	368.4
16F-B-12-5	2.6	239.2

The measured data of Figure 4.39 is repeated in Figure 4.40, but with an enlarged view of the data recorded over the first 250 seconds. This figure shows the BI plots of the 3 LWFC's spread around the $BI = 0$ line. A distinct horizontal strip of signal between -0.06 and 0.1 N/s is associated with the noise from the test control to alter the load application for micro-slip, and indicated with two dashed lines. It can be concluded that any positive BI reading greater than 0.1 N/s before the adhesion point is considered significant and is correlated to some factor influencing the bond integrity. In the sections to follow these 3 specimens will be individually evaluated for the resulting BI.

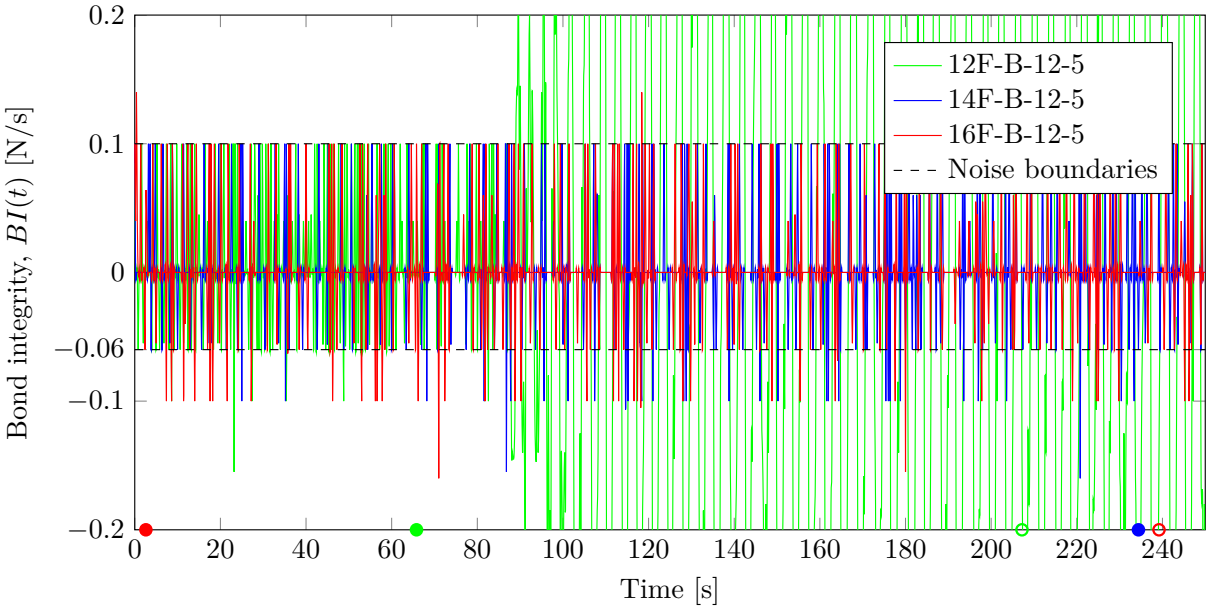

Figure 4.40: Bond integrity (BI) plotted over Y12 beam-end testing time for zero to 250 s, for specimens 12F-B-12-5, 14F-B-12-5 and 16F-B-12-5.

4.7.6.2 Bond integrity of 12F-B-12-5

The BI plot of specimen 12F-B-12-5 is shown in Figure 4.41. The loss of adhesion point (solid circle) occurs 66 seconds after the start of the test. When considering the BI, and therefore bond integrity, prior to the occurrence of adhesion loss, no positive oscillations are recorded above the 0.1 N/s noise boundary. The ductile failure of the 1200 kg/m^3 LWFC suggests that the bond deterioration is primarily governed by crushing of concrete in between the steel ribs. Before the adhesion point no considerable positive BI readings is seen, which suggests minimal internal cracking. On the contrary, just after the design point significant BI readings are seen as a result of the pull-out nature of the 1200 kg/m^3 LWFC, which has very little bond resistance at this stage in the test, and the machine is having to adjust the load applications very rapidly to adhere to the displacement rate.

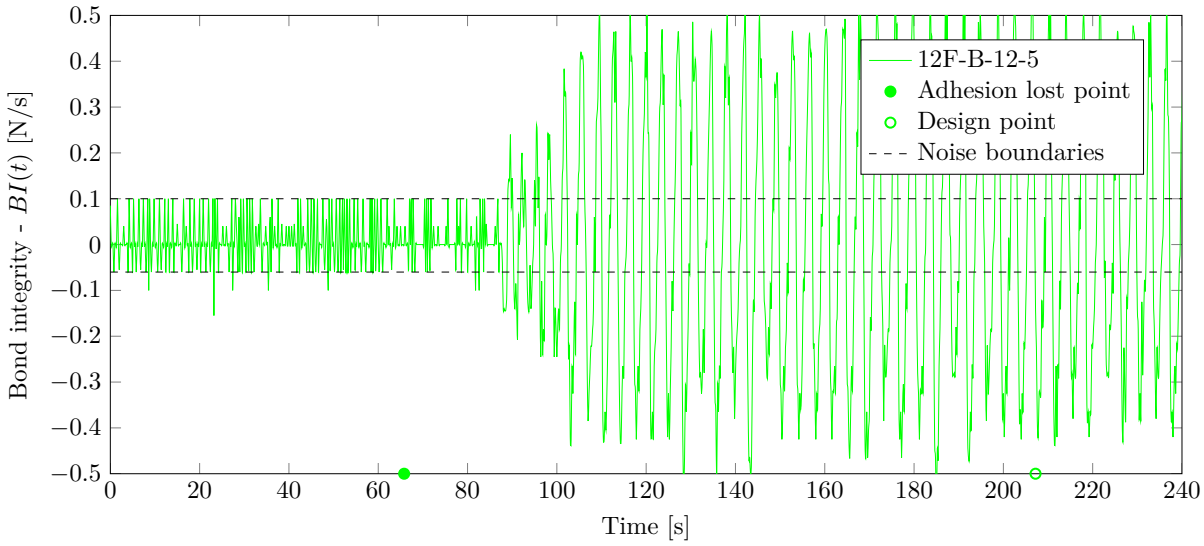

Figure 4.41: Bond integrity (BI) plotted over Y12 beam-end testing time for specimen 12F-B-12-5. The adhesion lost points (solid circle) and design point (circle) occurrences are shown at the bottom horizontal border.

4.7.6.3 Bond integrity of 14F-B-12-5

The *BI* of specimen 14F-B12-5 is plotted in Figure 4.42, showing no positive oscillations larger than the indicated noise boundary prior to the adhesion point, which also suggests minimal internal cracking. This figure concludes that the 1400 kg/m^3 LWFC provides better bond performance after the adhesion point compared to the large deviations seen for the 12F-B-12-5 specimen (Figure 4.41).

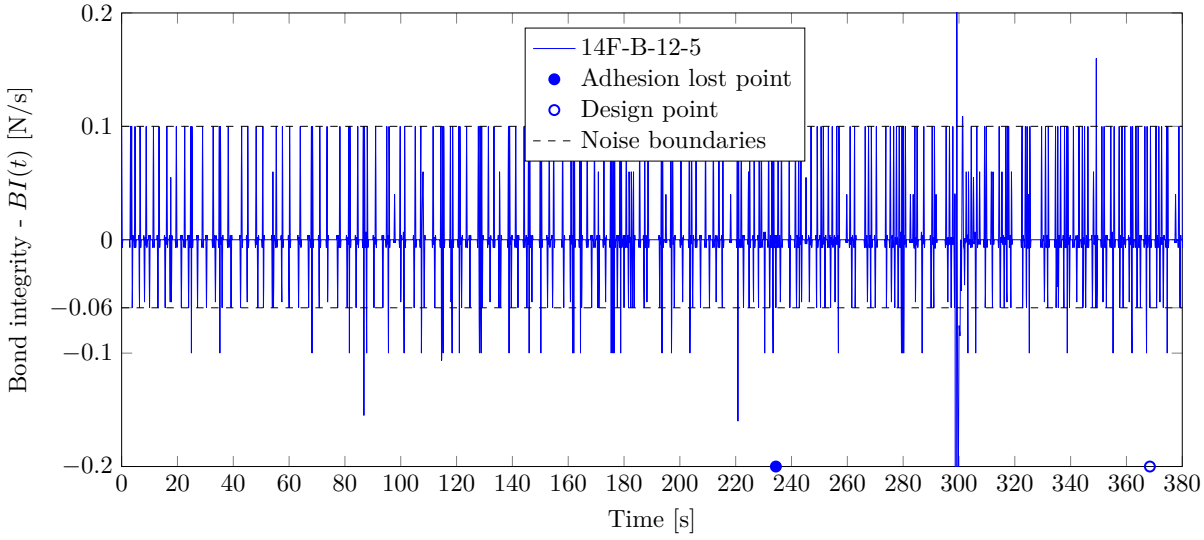

Figure 4.42: Bond integrity (BI) plotted over Y12 beam-end testing time for specimen 14F-B-12-5. The adhesion lost points (solid circle) and design point (circle) occurrences are shown at the bottom horizontal border.

4.7.6.4 Bond integrity of 16F-B-12-5

The BI of specimen 16F-B12-5 is plotted in Figure 4.43, showing a positive oscillation up to 0.16 N/s just before the premature adhesion occurrence at 2.6 seconds after the test procedure started. This concludes that the bond integrity was compromised soon after the test started. An internal crack is the most probable cause resulting from the increased brittleness of the denser LWFC, which then lead to the reduced bond-slip envelope seen in Section 4.7.5, Figure 4.38.

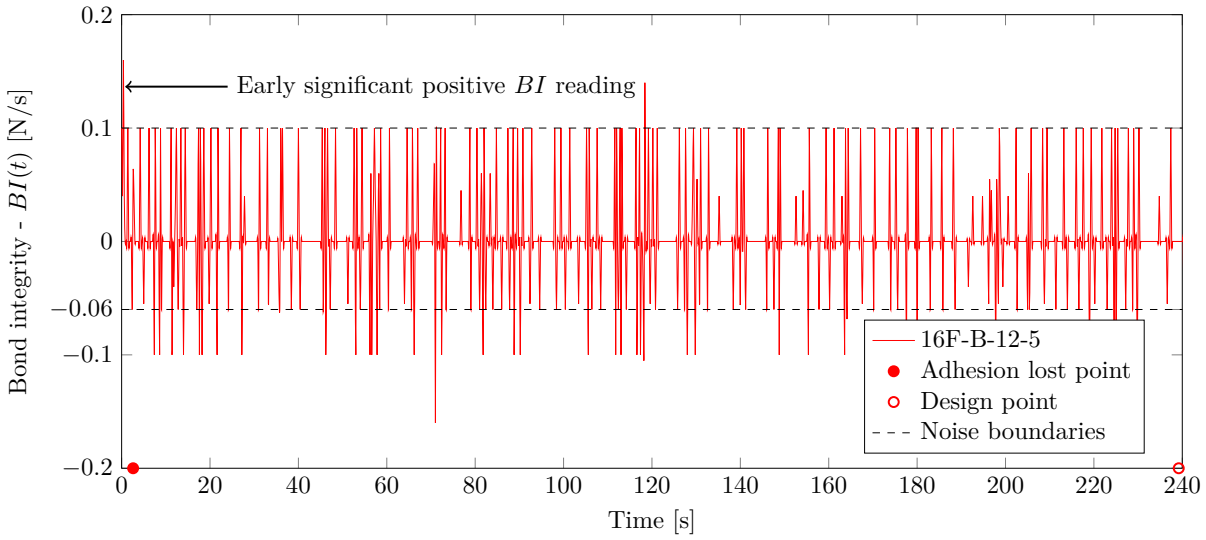

Figure 4.43: Bond integrity (BI) plotted over Y12 beam-end testing time for specimen 16F-B-12-5, showing early signs of bond deterioration with significant positive readings of BI. The adhesion lost points (solid circle) and design point (circle) occurrences are shown at the bottom horizontal border.

4.7.7 Comparison and conclusion of beam-end results

The measured BE design bond stresses (σ_d) are listed in Table 4.6. The NWC results are also indicated which, as expected, surpasses any design value recorded for LWFC.

The BE tests yield results that form a different tendency to what is observed in the conventional PO tests of Section 4.6. The manner in which the BE test is conducted ensures that if a material is susceptible to early secondary crack formation, it will follow suite. A comparison between the PO test and BE test follows in Chapter 5.

Table 4.6: Design bond stresses, σ_d, obtained from the results of the BE tests. For the specimen notation refer to Section 3.2.

Specimen	σ_d [MPa]
N-B-12-5	6.43
16F-B-12-5	0.72
14F-B-12-5	1.05
12F-B-12-5	1.06
N-B-20-5	12.65
16F-B-20-5	3.53
14F-B-20-5	3.36
12F-B-20-5	1.81

-o-O-o-

Chapter 5

Comparisons

Using a formulated method for obtaining the design bond stresses from measured data provided an effective design point and values suitable for comparing various concrete types. In this chapter the measured data from the pull-out and beam-end tests (see Sections 4.6 and 4.7, respectively) are compared. The measured design bond stresses are also correlated to design values specified in design documents used in practice.

5.1 Pull-out and beam-end tests

The bond characterization tests performed on LWFC and NWC resulted in a variation for the design bond stresses (σ_d) when comparing equivalent PO and BE tests. The σ_d obtained for the two tests and the resulting differences are depicted in Figure 5.1 for the range of concretes tested. The equivalent tests with Y12 and Y20 bars were respectively compared. The solid bar indicators of Figure 5.1 indicate PO σ_d values, the outlined bars represent BE σ_d values and the hatched bars indicate the difference in σ_d for PO and BE tests.

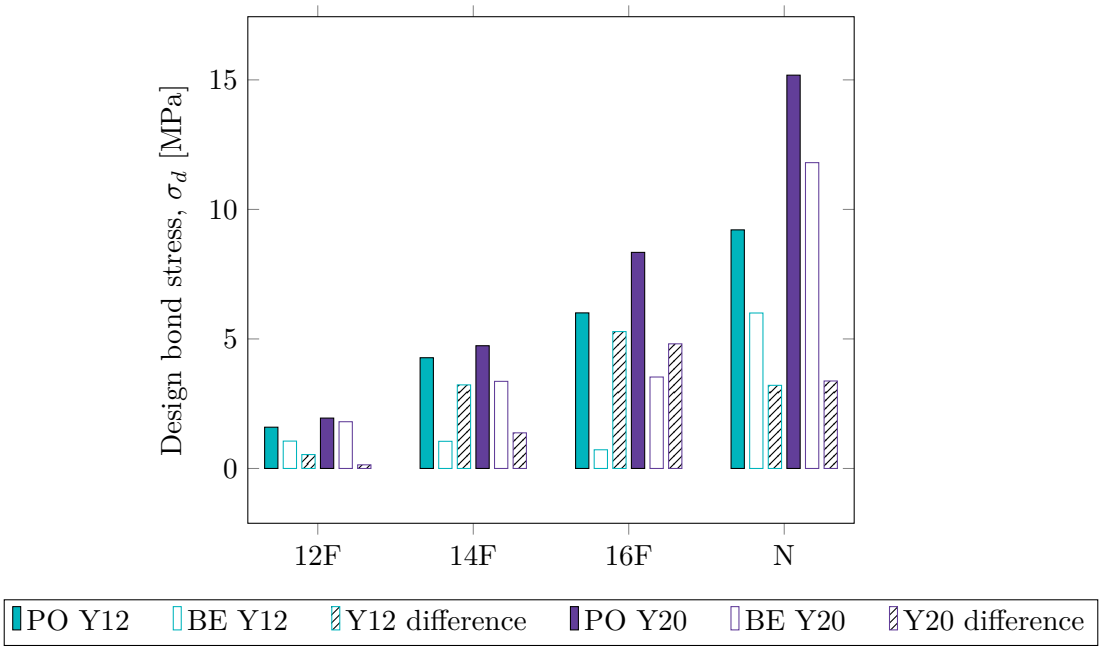

Figure 5.1: A depiction of the relative design bond stresses for all PO (solid bars) and BE (outlined bars) tests and the difference in design bond stresses of the PO and BE tests (hatched bars).

The BE tests resulted in lower σ_d values for all comparisons. The difference in σ_d is proportional to the density of the LWFC tested and is due to the BE test that exploits cracking susceptibility of a concrete matrix. The NWC comparison also indicated variability, but not to the same extent as observed for a LWFC of casting density of 1400 kg/m^3 or higher.

The σ_d results are also listed in Table 5.1. The LWFC that exhibited the best bond performance (16F with a Y20 embedded bar) developed only 55% of the σ_d obtained from the equivalent NWC test. Therefore it can be concluded that the σ_d for LWFC is significantly lower than that of NWC and the BE test provides a more conservative approach for finding the characteristic bond properties of deformed steel rebar in a structural member.

Table 5.1: The measured design bond stress results for the PO and BE tests, and the differences.

Concrete	ϕ	σ_d [MPa]		
		Pull-out	Beam-end	Difference
12F	10	1.89	-	-
	12	1.59	1.06	0.54
	20	1.94	1.80	0.14
14F	10	0.94	-	-
	12	4.27	1.05	3.23
	20	4.74	3.36	1.38
16F	10	1.20	-	-
	12	6.01	0.72	5.28
	20	8.34	3.53	4.81
N	10	1.76	-	-
	12	9.21	6.00	3.21
	20	15.18	11.81	3.38

5.2 Bond stress in design specifications

Engineering design standards do not explicitly identify the method used for obtaining the design bond stresses (σ_d) associated with a specific class concrete and therefore makes it impossible to create a comparative platform for these values and the measured data from this study. For this reason a single method, supported by literature, was used in this study, which comprises of assigning the σ_d as the stress occurring at a certain slip measurement (refer to Section 3.5) (Leonhardt, 1977). Figure 5.2 shows the σ_d obtained for all tests as a function of the cube compressive strengths of the specimens. The solid lines connect the averaged σ_d from the PO tests and the dashed lines connect the BE tests results, for 12F, 14F and 16F, at increasing compressive strengths.

The figure also indicate (black points) the σ_d specified in design standards SABS 0100-1 (2000) and BS EN 1992-1-1 (2004). Again it has to be pointed out these values provided in design standards can not be cross correlated to the measured values from this study, but it does provide some conclusions, as introduced below.

The σ_d obtained from the NWC PO and BE tests are also indicated with single points (orange and brown).

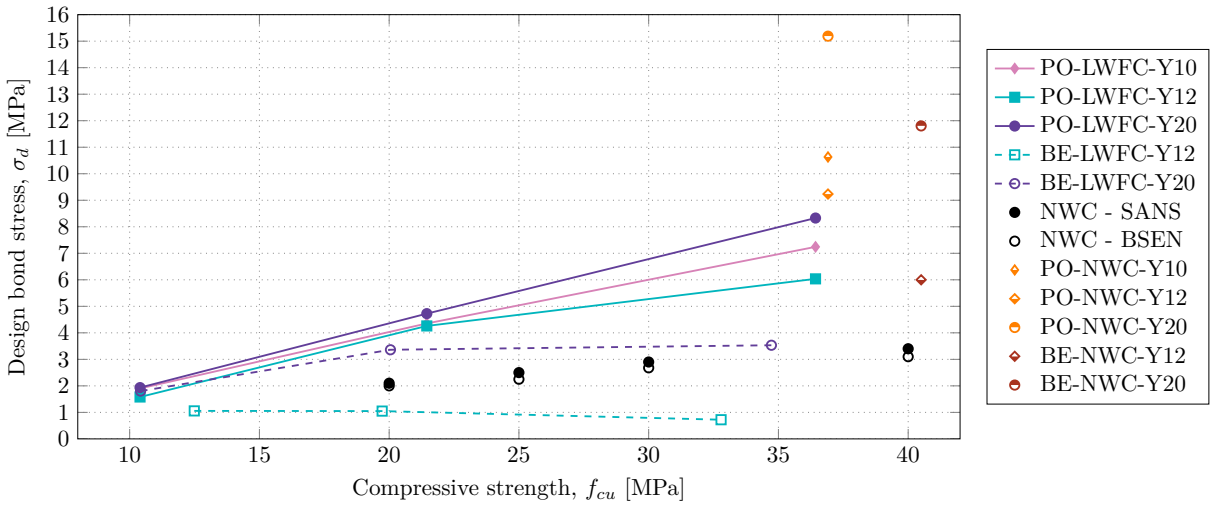

Figure 5.2: A comparative plot of the measured design bond stresses for all tests conducted in this study and specified design stresses from design documents, with the cube compressive stress as the independent variable. This plot is a means to assess the credibility of the method used for obtaining the σ_d values.

The following points can be derived from the data presented in the figure above:

- An almost direct relation is seen between σ_d from the LWFC PO tests (solid lines) and the measured f_{cu}.
- The LWFC BE tests (dashed lines) do not exhibit the same direct relation (see the point above) as for the LWFC PO tests (solid lines), and the former resembles a flattening towards the larger f_{cu} values. This is a similar shape to what is observed for the specified design values (black points) from SABS 0100-1 (2000) and BS EN 1992-1-1 (2004). This suggests that the specified design bond stresses (black points) were most likely obtained from bond tests similar to the BE test, which exploits the splitting susceptibility of stronger, brittler concrete. Also, it suggests that the BE test provides results that seem to simulate actual bond behaviour in structural systems and should therefore be used for design bond determination, rather than conducting the PO test.
- Similar to the conclusion in Section 5.1, the BE tests result in more conservative σ_d values.
- The measured NWC σ_d values (orange and brown points) are higher than the design values recommended by design specifications (black points), which suggest the method used in this study for obtaining the design point at 0.1 mm free-end slip (for PO and BE), might

not be the method used when these design standards were created, or additional safety factors were incorporated.

- Following on to the point above, it is known that the method used in this study provides non conservative σ_d values. The LWFC BE specimens (dashed lines) yield, although following a non-conservative method, in some instances a σ_d below the design values specified in SABS 0100-1 (2000) and BS EN 1992-1-1 (2004). This notion could render the bond performance of LWFC in structural application insufficient.
- When taking the conclusions above into consideration, it seems highly unlikely that the 1200 kg/m^3 LWFC ($f_{cu} \approx 12$ MPa) would yield applicable structural bond behaviour, since the values obtained from this study for all 1200 kg/m^3 LWFC tests lie below the lowest design bond stress specified in BS EN 1992-1-1 (2004).

-o-O-o-

Chapter 6

Modelling

With any industrial application that depends on a vast number of variables and prerequisites, it is advantageous to have a model that guides the user to a rapid selection with the required characteristics. This chapter presents a model that predicts the design bond stress of LWFC at 0.1 mm free-end slip. It differs from the modelling of Dae-Jin et al. (2014) and Zuo and Darwin (2000), which predicts peak bond stresses at varying free-end slip measurements. The model was developed, using an equilibrium of forces at the bond interface as the backbone of a mathematical expression, which predicts the design bond stress of deformed steel rebar embedded in LWFC. This expression can be used for predicting design bond stress in pull-out tests of LWFC and, by incorporating additional factors, predict equivalent beam-end results.

6.1 Pull-out test modelling

The first attempt to fit the measured data to equation (6.1) of Dae-Jin et al. (2014), which defines an existing model for lightweight artificial concrete, failed, because there was no matching of the measured data for bond strengths of LWFC. Dae-Jin et al. (2014) used 3 variables to predict the bond stress (σ) that include the concrete compressive strength (f_{cu}), the nominal bar diameter (ϕ) and the embedded length (l_e).

$$\frac{\sigma}{\sqrt{f_{cu}}} = \frac{37.5}{(\phi + l_e)^{\frac{1}{4}}} - 9.4 \tag{6.1}$$

A novel expression was therefore developed with the measured data of the LWFC pull-out tests. This expression incorporates the contribution of both failure modes (pull-out and splitting failure) to the bond stress at the design point.

The presented expression results from equilibrium of the forces present during bond deterioration at the moment where the design slip is reached. For convenience these forces and stresses are again shown schematically at the bond interface in Figure 6.1, with T_d the force in the rebar at the design point, v_b the bearing stress and v_s the shear stress. The geometric dimensions is repeated here with l_e the embedded length, c the rib spacing, e the inner diameter of the rebar, h the rib height and a the rib width. These dimensions are given in Section 3.6 for Y10, Y12 and Y20 rebars.

The adhesion stress, v_a, is ignored for modelling purposes, similar to what was done for the model published by Model Code (2010). This is justified since the model presented in this chapter predicts the design bond stress at the design point, which, by definition, imply that all adhesion stress have been surpassed and the mechanical bearing stage of the loading had begun. The bearing stress, v_b, of the steel ribs on the concrete and the shear stress, v_s, as a consequence of the concrete keys shearing off in between the ribs, are included in the new model, and are both correlated to the concrete cube compressive strength.

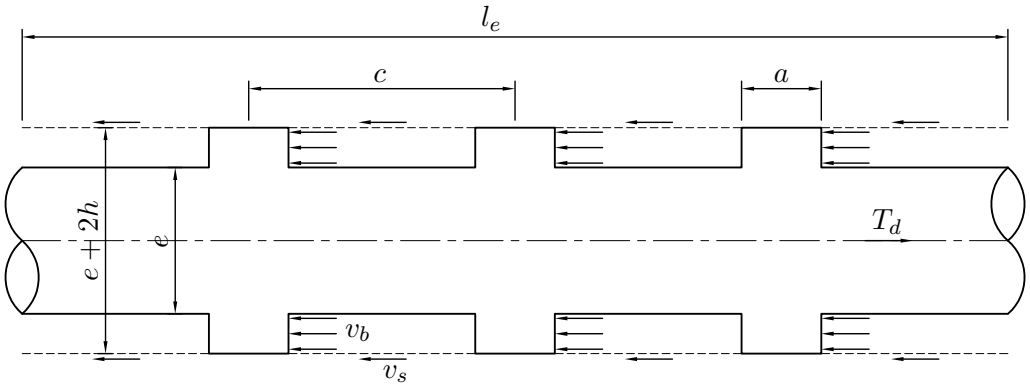

Figure 6.1: A schematic presentation of the stresses and forces present at the bond interface during pull-out tests. These stresses and forces, which contribute to bond development and deterioration, form the terms in the equilibrium force equation that is used for the development of the model.

The simple force equilibrium of the bond interface presented in Figure 6.1, is given by equation (6.2).

$$T_d = v_b.A_b + v_s.A_s \tag{6.2}$$

with

T_d the bar force at the moment of reaching the design point in the test, in N,

v_b the bearing stress in MPa,

v_s the shear stress in MPa,

A_b the contact area (representative rib area) on which v_b acts, in mm^2 and

A_s the contact area (representative shear area) on which v_s acts, in mm^2.

This simple equilibrium is representative of pure pull-out failure and does not incorporate the effect of splitting failure observed in testing. The splitting failure effect can be incorporated by changing the simple equilibrium equation above to

$$T_d = w_p.\left(v_b.A_b + v_s.A_s\right) + w_s.\left(v_b.A_b\right) \tag{6.3}$$

with

w_p a dimensionless pull-out failure weight factor and

w_s a dimensionless splitting failure weight factor.

In equation (6.3) the added term is introduced and allows for the reduction in T_d as a result of splitting cracks. For pull-out failure both v_s and v_b are present during bond loss, whereas for splitting failure the concrete keys do not shear off between ribs, which renders v_b the primary resistive stress. These two actions contribute differently to bond development up to the design point of 0.1 mm free-end slip. The only resisting force during internal crack formation (splitting) is the bearing stresses, which is also the primary source of energy for crack generation. The bearing force ($v_b.A_b$) is therefore used as a measure to predict the reduction brought forth by formation of internal cracks. In addition, dimensionless factors, w_p and w_s, are incorporated to account for degrees to which the various densities of LWFC's respond to the stresses at the bond interface, and the susceptibility of the concrete to the two failure modes.

The paragraphs to follow explains the population of the terms introduced in equations (6.2) and (6.3).

The bearing force term ($v_b.A_b$), which corresponds to the bearing stress contribution, is defined by $f_{cu}.2h.e.\,(l_e/c)$, with f_{cu} the measured bearing strength, $2h.e$ the representative rib area and (l_e/c) the number of ribs within the test embedded length. The shear force term ($v_s.A_s$), which corresponds to the shearing stress contribution is $(f_{cu})^{\frac{1}{3}}\,(l_e - (l_e/c)\,(a))\,.\pi\,(e+2h)$, with $(f_{cu})^{\frac{1}{3}}$ the representative shear strength and $(l_e - (l_e/c)\,(a))\,.\pi\,(e+2h)$ the shear plane contact area over the embedded length, l_e.

The representative shear capacity, $(f_{cu})^{\frac{1}{3}}$ was derived from relations found in §6 of BS EN 1992-1-1 (2004). These equations yield a design shear resistance as a function of $(f_{cu})^{\frac{1}{3}}$. The shear strength of LWFC at the bond interface level was not investigated and could be used for further research on the development of reinforced LWFC. The factor was therefore used to relate the measured compressive strength to a shear capacity at the bond interface.

The two weight factors w_p and w_s, which respectively correspond to the pull-out and splitting failure, are used to shift the intensity effect of these two failure modes on the development of bond force. w_p and w_s are substituted with $(\rho/1200)^2$ and $(-\rho/1200)^{0.25}$, respectively, which simulates the effect of the LWFC casting density (ρ) on the resulting failure mode and consequently the bond development. w_p has a positive influence on the bond development, while w_s presents a negative term, which reduces the bond at the design point as a result of splitting failure. These factors were calibrated by using the resulting failure modes for various density LWFC's tested in Section 4.6. For example, the w_p factor contributes larger bond strength for a dense LWFC. This direct proportional increase in bond strength and density is reported in Section 4.6 and specifically seen in Figure 4.21. The negative splitting weight factor, w_s, intensifies the negative term when considering a denser, more brittle LWFC. The w_s factor is much less weighted than the w_p factor to simulate the degree to which these failures contribute/reduce the design bond stress.

This equilibrium from equation (6.3) can be substituted for equation (6.4), with Ψ given in equation (6.5), which consists of three distinctive terms populated by the terms introduced above.

$$T_d = \Psi \tag{6.4}$$

$$\begin{aligned}\Psi = &\left(\frac{\rho}{1200}\right)^2 \left\{(f_{cu}.2h.e)\left(\frac{l_e}{c}\right) + (f_{cu})^{\frac{1}{3}}\left(l_e - \left(\frac{l_e}{c}\right)(a)\right).\pi\,(e+2h)\right\} \\ &- \left(\frac{\rho}{1200}\right)^{0.25}\left\{(f_{cu}.2h.e)\left(\frac{l_e}{c}\right)\right\}\end{aligned} \tag{6.5}$$

The equality of the equilibrium and the measured data is shown in Figure 6.2. This model is valid for LWFC in the range between 1200 and 1600 kg/m^3 and any extrapolation may neglect the effects of other failure modes. However, this range is adequate for what is accepted as a LWFC and it is also within structural material compression strength classification.

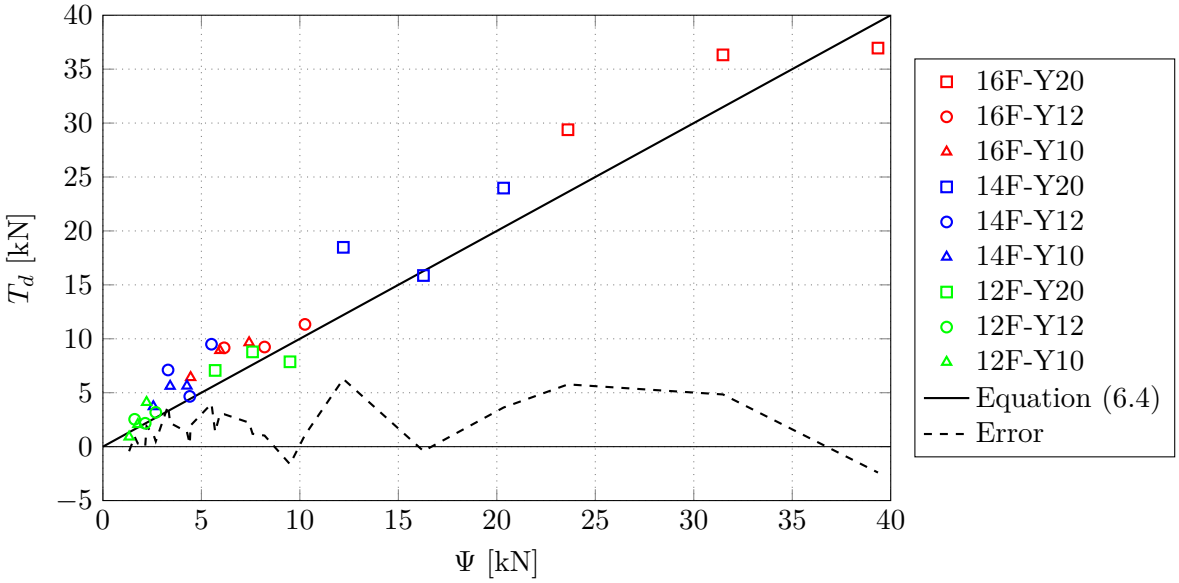

Figure 6.2: The measured pull-out data of LWFC PO tests against a mathematical prediction model (solid line) for the design bond force, T_d. The difference in predicted results and actual result is presented by the error function (dashed line). A positive error is considered a conservative prediction.

Figure 6.2 above shows the data points from the pull-out tests distributed around the proposed model (indicated by solid line). The errors are also indicated on the same axis, with a positive error indicating a conservative prediction. The data points with negative errors are of concern, because the model predicts a higher bond force than the actual design bond strengths. Table A3 in Appendix E, lists the modelling errors associated with each specimen and shows a maximum negative T_d error of 47% for specimen 12F-P-10-3. This is attributed to the bond stresses that are very low for the least dense LWFC, compared to what is measured for the denser LWFC. It also emphasize the fact that the 1200 kg/m^3 LWFC performs poorly in bonding and should for

all intent and purposes be excluded from the modelling, since such a small design bond stress can not economically be used in a safe structural application.

6.2 Beam-end test prediction

The difference observed between the PO test and the more conservative BE test was reported in Chapter 5. The above mentioned model for the PO test can be adjusted to produce a more conservative result, which predicts the design bond stresses with the BE tests.

In order to compare these tests the fact that the casting density of a specimen is not exactly the target density, and may vary up to 50 kg/m^3, has to be considered. For example, the PO test on the 1200 kg/m^3 LWFC was done on a specimen of density 1202 kg/m^3, while the BE test for the same density specification was done on a 1233 kg/m^3 specimen. Therefore, the direct correlation between results is not advised. For this reason the design bond stresses (σ_d) were normalized with the actual casting density, yielding a ratio indicating the bond stress per kg/m^3. These ratios are then multiplied by the intended target density to obtain a relative framework with which the two tests can be compared. The stresses found from this normalizing is then evaluated as a ration between the BE and PO stress, given by μ. Figure 6.3 shows the μ ratios of the LWFC with various target densities.

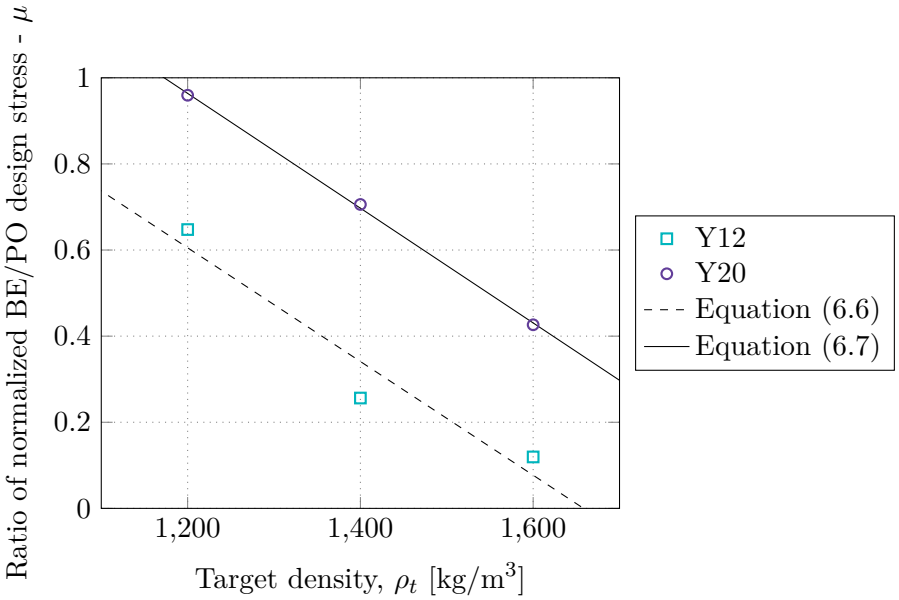

Figure 6.3: Ratio of the PO and BE normalized design bond stresses for Y12 and Y20 bars, versus the target densities of the normalized unit.

Least square regression fits through the data for each of Y12 and Y20 bars in Figure 6.3, yield equations (6.6) and (6.7), which generate the factors μ_{12} and μ_{20}. These factors simulate the changes in the μ ratio (as a function of the target density, ρ_t) for the Y12 and Y20 bars respectively.

$$\mu_{12} = -0.00132\rho_t + 2.1894 \tag{6.6}$$

$$\mu_{20} = -0.00133\rho_t + 2.5629 \tag{6.7}$$

These factors can then be implemented with the mathematical model described by equation (6.4). The beam-end model is found by multiplying the factors μ_{12} and μ_{20} with the pull-out model (equation (6.4)), for Y12 and Y20 bars, respectively. These altered models for BE tests are given by equations (6.8) and (6.9) for Y12 and Y20 bars, respectively.

$$T_d = \mu_{12}.\Psi \tag{6.8}$$

$$T_d = \mu_{20}.\Psi \tag{6.9}$$

This modification to the pull-out model does not include the variation in embedded lengths since the beam-end tests were all conducted on one embedded length.

It does confirm accurate factors (equations (6.6) and (6.7)) to use when considering the change in design bond for LWFC in the PO and BE tests. A verification of the effective implementation of these factors are depicted in Figure 6.4 and an accurate and conservative correlation is seen between the measured bond from the BE tests (see Section 4.7) and the predicted values is observed.

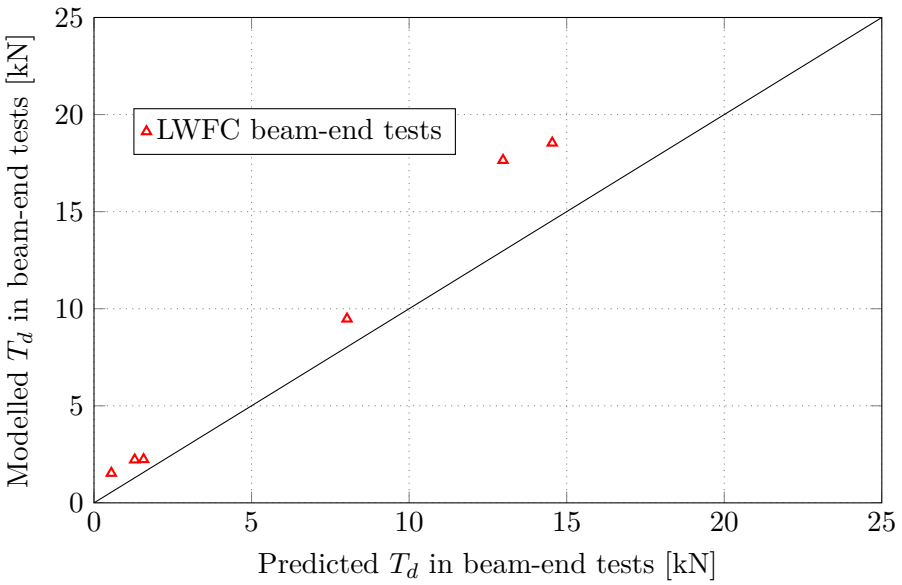

Figure 6.4: A verification of the modified model (equations (6.8) *and* (6.9)*) for determination of the resulting design bond force in the BE tests, derived from the model initially developed for the design bond stress of the PO test data (equation* (6.4)*).*

6.3 Conclusion

A prediction model of the design bond stress for typical steel reinforcement embedded in LWFC is introduced. The model was developed from a global equilibrium of the forces present within the embedded region of the steel rebar during bond deterioration, taking into account the relative changes of forces during the process. The variables within the model include the compressive strength, rib height, inner bar diameter, embedded length, rib spacing, rib width, and casting density. For the purpose of the model presented here, the shear resistance was provided as a function of the compressive strength derived from published relations in BS EN 1992-1-1 (2004). The model indicates significant errors with the 1200 kg/m^3 LWFC, which confirms that the magnitude of the design bond stress is about the same values as typical errors seen for these specimens.

The model is modified with normalized factors to predict the design bond strength for an equivalent test conducted with the BE test for Y12 and Y20 bars respectively.

-o-O-o-

Chapter 7

Conclusions and Recommendations

This study followed from the desire to apply LWFC for more comprehensive structural applications, but also to understand the concern that LWFC lacks structural strength for use as a structural member. It led to the development of important characteristic bonding properties and also opened new avenues of questions and ideas for future studies. The thesis as a whole is an earnest contribution to the process of redressing the shortage of literature and design guidance on LWFC.

7.1 Conclusions

It is possible to mix LWFC accurately to within the proposed casting density margin of 50 kg/m^3, but a significant effect is observed for allowed deviations from the intended target density on engineering properties and the bond performance. It is therefore suggested that this margin be reduced.

The general engineering properties of LWFC was tested and compared to that of NWC:

- The range of LWFC's obtained mean compressive strengths in the order of 10 MPa, 18 MPa and 31 MPa for casting densities of 1200 kg/m^3, 1400 kg/m^3 and 1600 kg/m^3, respectively. This concluded that it is possible to obtain structural compressive strengths for certain casting densities of LWFC.
- The measured Young's modulus results for LWFC are less than that obtained for NWC. It does however correlate well with the Young's modulus values used for design of LWAC structures. This confirms the possibility of implementing a reduced Young's modulus material in structural application.
- Only the tensile splitting strength of the 1600 kg/m^3 LWFC achieved strengths comparable to what is found for NWC.
- A specific fracture energy of 5.72 N/m was obtained for 1400 kg/m^3 LWFC, which is low compared to NWC with fracture energies in the order of 152 N/m. The wedge splitting tests confirmed the direct proportionality of both the brittleness and casting density, and specific fracture energy and casting density.

Two bonding tests, the conventional pull-out (PO) and the beam-end (BE) tests, were successfully applied on LWFC with typical deformed steel reinforcement, which resulted in the following conclusions:

- The identification of a design point was defined and effectively used, which is correlated to a bar slip measurement. Although this design point appears to result in a non-conservative approach when comparing it to bond stresses specified in design documents, it still provides a quantitative method, which incorporates physical phenomena during bond deterioration.
- Tests standards do not suggest the testing of various embedded lengths, but from the measured data it was found that the embedded length has a large influence on the failure regime and consequent bond-slip envelope. This effect was more evident in the LWFC tests than with NWC. Therefore it is recommended that multiple embedded lengths are used in bond-slip tests for LWFC or any reduced strength material.
- For all LWFC PO tests the bond-slip envelopes are below those obtained for the NWC specimens. The 1600 kg/m^3 LWFC yielded splitting failure of specimens for all embedded lengths and nominal bar sizes tested. Compared to the NWC, this dense LWFC exhibited bond-slip envelopes with good bond stress magnitude, but lacked ductile failure. At the lighter end of the LWFC spectrum, the 1200 kg/m^3 LWFC resulted in pull-out failure for all specimens tested, but at such a low magnitude that in some instances the adhesion stress surpassed the mechanical bonding. These tests showed that the 1200 kg/m^3 LWFC has the desired ductile bond failure, but at insignificant magnitude. The NWC tests resulted in bond-slip envelopes of larger magnitude and more ductile failure, compared to the performance of all LWFC's.
- The BE test was successfully conducted with accurate slip displacement control of 0.001 mm/s at the loaded-end of the specimen. The specified specimen was altered by changing the positioning of the bonded length to ensure that the lateral supports do not influence the stress at the bonded region and to include the embedded length within the bending moment region.
- All BE tests resulted in more conservative design bond stress values than the PO test.
- For all bond tests the 1400 kg/m^3 was observed to perform the best. In higher densities, the brittleness leads to internal cracks and subsequent early bond deterioration. On the contrary, a lower density leads to a weak material not capable of providing sufficient mechanical structural bond resistance.

The bond deterioration in LWFC's was quantified by using a comparison of deviations in the rates of the applied and measured forces during the BE test. The implementation of bond integrity (BI) showed promising signs of detecting the onset of internal cracking and could form the basis for a new technique of assessing bond behaviour. The downfall of such a implementation is the complex test procedure with specific actuator control configurations. These configurations were successfully implemented in the BE test using the *Instron* software.

Even though the methods used by design standards to obtain design bond stresses are not known, a comparison was made between these stresses and the design stresses measured during this study. The following concluded from the comparison:

- The relative design bond stresses of the NWC tested suggests the design standard developers made use of another technique and/or additional safety factors to obtain the design bond stress as provided in BS EN 1992-1-1 (2004). The technique used in this study provided design bond stresses larger (less conservative) than what is provided in design documents.
- The BE test yielded results that follow the same tendencies as for design bond stresses specified in design documents (BS EN 1992-1-1, 2004; SABS 0100-1, 2000) with increase in concrete compressive strength. This suggests that the BE test yields bond behaviour that simulates the bonding action in structural systems better than seen for the PO test. It is consequently proposed that the BE test be used rather than the PO test when assessing the structural bond performance of reinforcement in a structural member.
- Although following a non-conservative method, the 1200 kg/m^3 LWFC yielded design bond stresses of similar magnitude to what is provided in design standards. This suggests the use of this LWFC not suitable for structural use.

The PO test data was successfully used to formulate a prediction model from a force equilibrium relation at the bond interface by taking into account the two failure mechanisms with associated bearing and shear forces at the design slip point. The model includes the LWFC casting density, the inner and outer bar diameter, the embedded length, the rib spacing, height and width, and the compressive strength as variables. The PO design bond model was further enhanced by factors to also predict BE design points.

A problem with the LWFC and its bond capacity is the margin in densities suitable for structural use. At the lower end the 1200 kg/m^3 lacks sufficient compressive strength and at the other end the 1600 kg/m^3 is too brittle. If by some measure this margin could be increased, allowing for less brittle materials at higher density (and compressive capacity), it may lead to the effective use of LWFC in structural applications.

It is recommended that, with the hitherto development of LWFC, this material not be used in structural application.

The following recommended studies may result in influences on the bonding of LWFC and subsequently render the material useful for structural use.

7.2 Recommendations for future studies

LWFC bond performance does not compare well with that seen for NWC and further research in material development could improve the bond behaviour. The brittleness of LWFC forms a critical factor in the bond capacity. Fibre reinforced LWFC could result in a less brittle material

leading to improved bond capacities, although it is believed that fibre reinforcing alone will not result in bond properties that compare to NWC and additional studies, such as increased compressive strengths at lower densities, would have to be launched to collectively further the development of LWFC.

Lightweight aggregates, or even normal density aggregate, in combination with entrained foam might lead to better compressive strengths and bond properties.

Secondary reinforcement provides additional bond capacity due to the confinement of the concrete adjacent to the bond interface. The effective design of secondary stirrups in a LWFC structural member could reduce the susceptibility of splitting failure and provide sufficient bond capacity, comparable to that seen for NWC.

Shear resistance of LWFC proved to be a problem with preliminary large BE tests. Limited literature exists on this topic. In a structural member the shear flow is part of the force transmission to the bonded regions. The specimens were made to be small enough so bond failure occurs prior to any form of shear failure. This occurrence showed that the shear capacity of LWFC is lower than that of NWC and should be investigated.

Minor defects caused by the rolling out and cutting of Y10 and Y12 rebar could influence bonding behaviour and provide answers to erratic data seen with the conventional pull-out test.

-o-O-o-

References

ACI 318-11 (2011). *Building Code Requirements for Structural Concrete*. American Concrete Institute. Michigan.

ACI Committee 408 (1992). "Abstract of: State-of-the-Art-Report: Bond under Cyclic Loads". In: *ACI Materials Journal* 88.6.

Addis, Brian Jeffrey and Owens, Gill (2009). *Fulton's concrete technology*. Cement & Concrete Institute.

AshResources (2011). *AshResources - Fly ash products - DuraPozz*. 35 Westfield Rd, Longmeadow Business Estate Ext 11, 1609 P.O. Box 3017, Randburg, 2125.

ASTM A944-10 (2002). *Comparing Bond Strength of Steel Reinforcing Bars to Concrete Using Beam-End Specimens*. ASTM International. Pennsylvania, USA.

ASTM C230 (2001). *Standard Specification for Flow Table for Use in Tests of Hydraulic Cement*. ASTM International. Pennsylvania, USA.

ASTM C469 (2002). *Static Modulud of Elasticity and Poisson's Ratio of Concrete in Compression*. ASTM International. Pennsylvania, USA.

Autocad (2014). 1-18-0-0 edn. Autodesk.

Brühwiler, E and Wittmann, FH (1990). "The wedge splitting test, a new method of performing stable fracture mechanics tests". In: *Engineering Fracture Mechanics* 35.1, pp. 117–125.

BS 8110-1 (1997). *Structural use of concretet. Part 1: Code of practice for design and construction*. British Standards Institution. London.

BS 8110-2 (1985). *Structural use of concretet. Part 2: Code of practice for special cicumstances*. British Standards Institution. London.

BS EN 1992-1-1 (2004). *Eurocode 2: Design of concrete structuresPart 1-1: General rules and rules for buildings*. British Standards Institution. London.

Byun, K.J., Song, H.W., Park, S.S., and Song, Y.C. (n.d.). *Development of structural lightweight Foamed concrete using Polymere foam agent*. Department of Civil Engineering, Yonsei University. Korea.

Dae-Jin, K., Min Sook, K., Geun Young, Y., and Young Hak, L. (2014). "Bond strength of steel deformed rebars embedded in artificial lightweight aggregate concrete". In: *Journal of Adhesion Science and Technology* 27.5-6, pp. 490–507.

Desnerck, P. and De Schutter, G. (2010). "Bond behaviour of reinforcing bars in self-compacting concrete: experimental determination by using beam tests". In: *Materials and Structures* 43, pp. 53–62.

El Zareef, M. and Schlaich, M. (2008). "Bond behaviour between GFR bars and infra-lightweight concrete". In: *Tailor Made Concrete Structures*, pp. 721–727.

EN 10080 (2005). *Steel for the reinforcement of concrete - Weldable reinforcing steel - General*. European Standard.

Farghal Maree, A. and Hilal Riad, K. (2014). "Analytical and experimental investigation for bond behaviour of newly developed polystyrene foam particles' lightweight concrete". In: *Engineering Structures* 58.1, pp. 1–11.

Federation Internationale de la Precontraine (1983). *FIP manual of Lightweight Aggregate Concrete*. Surrey University Press. Glasgow.

Hulse, J. (2015). Steel distributors - sponsored steel for study. Range Rd, Blackheath, Cape Town, South Africa: Hulse reinforcing.

Ian Ramsay (2015). IainR@advancedlab.co.za. Instron.

Johnson Alengaram, U., Mahmud, H., and Jumaat, M.Z. (2010). "Comparison of mechanical and bond properties of oil pal kernel shell concrete with normal weight concrete". In: *International journal of the physical sciences* 5.8, pp. 1231–1239.

Jones, M. (2015). mark.jones@ppc.co.za. PPC - Pretoria Portland Cement. South Africa. URL: {www.ppc.co.za}.

Jones, M.R. and McCarthy, A. (2005). "Preliminary views on the potential of foamed concrete as a structural material". In: *Magazine of Concrete Research* 57.1, pp. 21–31.

Jumaat, M.Z., Alengaram, U.J., and Mahmud, H. (2009). "Shear strength of oil palm shell foamed concrete beams". In: *Materials and Design* 30, pp. 2227–2236.

Kearsley, EP and Mostert, HF (2005). "Designing mix composition of foamed concrete with high fly ash contents". In: *Proc., Int. Conf. on the Use of Foamed Concrete in Construction*. Thomas Telford, London, pp. 29–36.

Kearsley, E.P. and Wainwright, P.J. (2002). "Ash content for optimum strength of foamed concrete". In: *Cement and Concrete Research* 32, pp. 241–246.

Kearsley, EP and Mostert, HF (2003). "The effect of fibre reinforcing on foamed concrete behaviour". In: *Proceeding of the International Symposium Dedicated to Professor Surendra Shah, Northwestern University, USA*.

Kearsley, E.P. and Wainwright, P.J. (2001a). "Porosity and permeability of foamed concrete". In: *Cement and Concrete Research* 31, pp. 805–812.

Kearsley, EP and Wainwright, PJ (2001b). "The effect of high fly ash content on the compressive strength of foamed concrete". In: *Cement and concrete research* 31.1, pp. 105–112.

Leonhardt, F. (1977). *Vorlesungen über Massivbau: Teil 3: Grundlagen zum Bewehren im Stahlbetonbau*. Vorlesungen über Massivbau. Springer-Verlag GmbH. ISBN: 9783540081210. URL: http://books.google.co.za/books?id=ZEf87H0i9MsC.

Model Code (2010). *FIB. Special Activity Group 5*. CEB and FIB.

Oluokun, F. A. (1991). "Prediction of concrete tensile strength from compressive strength: evaluation of existing relations for normal weight concrete". In: *ACI Materials Journal* 88.3, pp. 302–309.

Orangun, CO, Jirsa, JO, and Breen, JE (1977). "A reevaulation of test data on development length and splices". In: *ACI Journal Proceedings*. Vol. 74. 3. ACI.

Park, R. and Paulay, T. (1975). *Reinforced Concrete Structures*. New Zealand: Wiley-Interscience Publication. ISBN: 0471659177.

Pedziwiatr, J. (2008). "Influence of internal cracks on bond in cracked concrete structures". In: *Archives of civil and mechanical engineering* VIII.3.

Penelis, George G. and Penelis, Gregory G. (2014). *Concrete Buildings in Seismic Regions*. CRC Press - Taylor & Francis Group.

Products, Inca Concrete (2015). sales@incaconcrete.co.za. Inca.

Robberts, John M. and Marshall, Vernon (2010). *Analysis and Design of Concrete Structures*. Cement, Concrete Institute, and Nuclear Structural Engineering.

SABS 0100-1 (2000). *The structural use of concrete, Part 1: Design*. The South African Bereau of Standards. South Africa.

SABS 5863 (2000). *Concrete tests - Compressive strength of hardened concrete*. The South African Bereau of Standards. South Africa.

SABS 6253 (2000). *Concrete tests - Tensile splitting strength of concrete*. The South African Bereau of Standards. South Africa.

SABS 920 (2011). *Steel bars for concrete reinforcement*. The South African Bereau of Standards. South Africa.

Sancak, E., Simsek, O., and Apay, A.C. (2011). "A comparative study on the bond performance between rebar and structural lightweight pumice concretewith/without admixture". In: *International Journal of the Physical Sciences* 6.14, pp. 3437–3454.

SANS 50450-1 (2011). *Fly ash for concrete Part 1: Definition, specificatins and conformity criteria*. The South African Bereau of Standards. South Africa.

Scott Orthey (2015). sorthey@astm.org. ASTM International.

Sistonen, E., Tulkiainen, P., and Huovinen, S. (2001). *Bonding of hot dip galvanised reinforcement in concrete*. URL: https://www.tekna.no/ikbViewer/Content/225411/F40%20-%20Sistonen%20-%202005-09-02%20FINAL.pdf (visited on 06/18/2014).

Soltani, Masoud, An, Xuehui, and Maekawa, Koichi (2003). "Computational model for post cracking analysis of RC membrane elements based on local stress–strain characteristics". In: *Engineering structures* 25.8, pp. 993–1007.

Sung-Nam, H., Jun Myoung, P., Tae-Wan, K., Kyoung-Bong, H., Sun-Kyu, P., and Won-Jun, K. (2008). "Bond stress-slip relationship in reinforced concrete: New relationship and comparative study". In: *33rd Conference on Our World in Concrete and Structures* 33.

Thomas, Jeffery J. (2015). sarcea@iafrica.com. SARCE - South African Reinforced Concrete Engineers' Association. 12 Skeen Boulevard, Bedfordview, Johannesburg, South Africa. URL: {www.sarcea.co.za}.

Van Rooyen, A.S. (2013). "Structural lightweight aerated concrete". Stellenbosch, South Africa: Structural Engineering, University of Stellenbosch.

Wittmann, FH (2002). "Crack formation and fracture energy of normal and high strength concrete". In: *Sadhana* 27.4, pp. 413–423.

Zuo, Jun and Darwin, David (2000). "Splice strength of conventional and high relative rib area bars in normal and high-strength concrete". In: *ACI structural Journal* 97.4.

Appendices

A Beam-end loop tuning

During the loop tuning of the Instron machine for the BE test setup, the control can be tuned with various factors that all have a unique function of operation. It is known as the PID control; proportional, integral and derivative.

These factors have different operator functions and work together to ensure the input and output is closely matched. Within a closed loop system, such as the Instron testing machine, the system has a demand and feedback during a certain period of time. The demand being what is prescribed by the operator and the feedback the actual events taking place during tests and the difference between the demand and feedback is known as the error. When the machine is correctly configured, the process will minimize the error over a time period. With the control loop correctly configured, any changes in the error are eliminated by combining these three factors. In order to obtain the desired demand a certain gain is needed, which can be varied by changing the proportional factor. This factor can be seen as the constant multiple of the error. Equation (A1) provides a mathematical explanation to the proportional factor, with P the proportional factor and ϵ the error. Their product is the response value that is sent to the actuator.

$$response = P \times \epsilon \tag{A1}$$

This shows that a large proportional factor is required for very small errors and vice versa. However when the error is too small during control, the response becomes negligible. Therefore the other operators (integral and derivative) are also needed to fit the required demand. When the loop reaches a steady state, i.e. no change in error, there could still exists an error which the proportional operator cannot eliminate. This is then dealt with by the integral operator.

Through testing it was found that a proportional factor that is too large tends to overshoot the required demand and go into oscillation. The proportional factor can be negative or positive depending on whether the demand or feedback is the greater value. It is however nearly impossible to accurately determine the error values especially with a complicated test specimen stiffness. Therefore this proportional factor was fine tuned through trial and error.

The integral term refers to the summation of the error function over a certain time period. Equation (A2) shows this operator in mathematical form, with I being the integrator factor, $f(\epsilon)$ the error function and t time.

$$I = \int f(\epsilon)dt \tag{A2}$$

The integrator function is used to eliminate any steady state offset or error. Even with very small errors, when the proportional operator is inactive, the integral operator is collecting error information over a time period and adjusting the input accordingly. A shorter integral time (I/s) ensures that the integral works more aggressively at correcting the steady state offset.

The derivative operator is constantly looking for a rate of change in the error ($\delta\epsilon$). The more error changes or the longer the derivative time, the larger the derivative factor becomes. The derivative operator is used to counteract any overshoot caused by both or a combination of the proportional and integral operators. When the error values are large the proportional and integral operators are aggressively minimizing this error and therefore makes numerous changes in the input, which in turn ensures changes in the error values. These changes in the error ($\delta\epsilon$) are then dealt with by the derivative operator and uses it to counteract the overshoots.

On the advice by Ian Ramsay (2015) these factors were altered to find a good fit with more overshoots than undershoots. On his advice the default values for the integral and derivative terms were always used. Figure A1 is a screen dump from the Instron software (REF) during loop tuning for the beam-end test. The red line is the desired waveform (demand or input) and the green is the LVDT measurement (feedback or output). The proportional factor was set at 35 dB which shows that, at this rate, the machine over corrects at a certain increment leading to excessive displacement corrections which will ultimately render test data inaccurate and could even damage the machine due to oscillations. In this instance the proportional factor is too high and does not accurately simulate the ratio of demand to error.

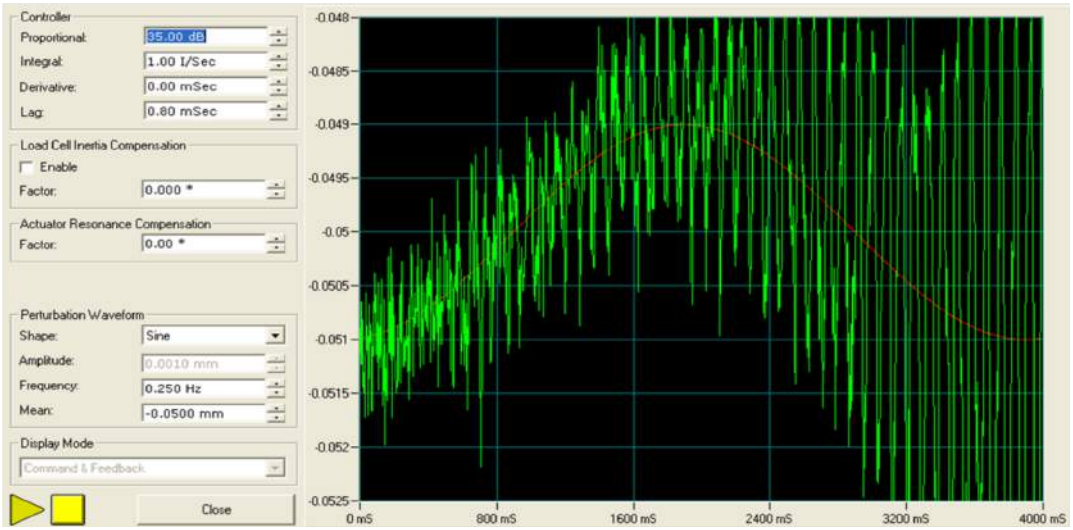

Figure A1: A screendump from the software that controls the loop tuning of the Instron, shows the condition where the proportional factor was selected too high, indicated by the increasing oscillations (in green) about the ideal path (in red).

Figure A2 shows the loop tuning state with the proportional factor at 10 dB. This setting appeared to accurately obtain the desired waveform but lags in time.

The best fit to the desired waveform was obtained with a proportional factor setting at 19.9 dB and the result is depicted with the screendump in Figure A3.

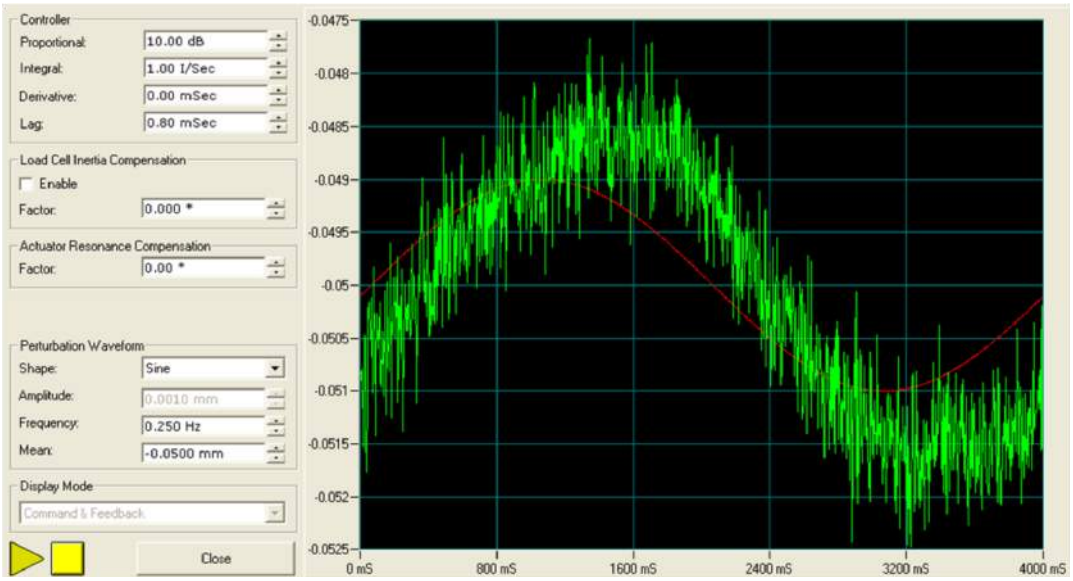

Figure A2: A screendump from the software that controls the loop tuning of the Instron, shows the condition where the proportional factor was selected too low and indicated by the out of phase signals (red and green).

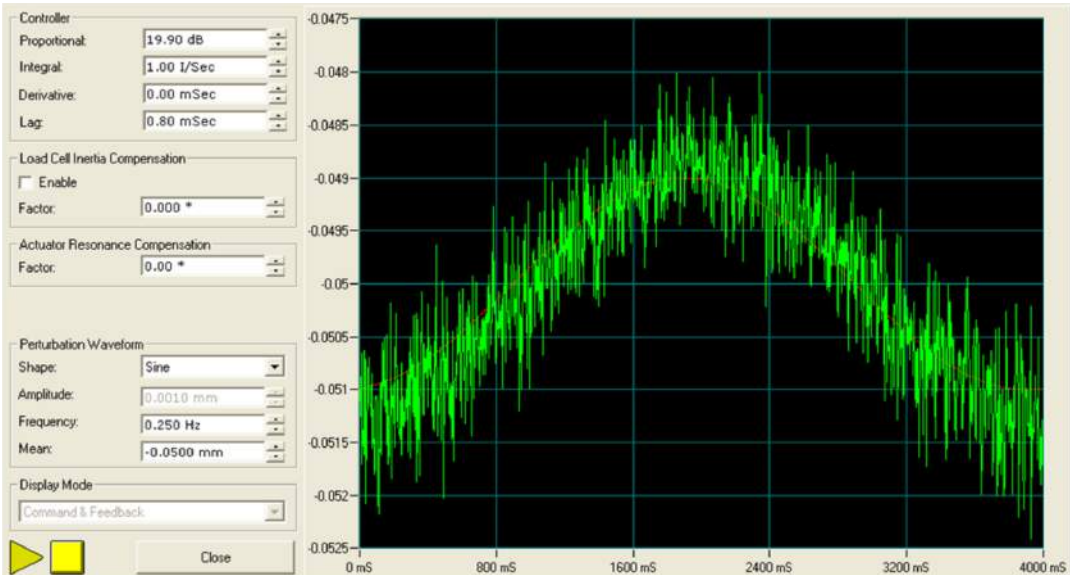

Figure A3: A screendump from the software that controls the loop tuning of the Instron, shows the condition where the proportional factor was selected correctly at a 19.9 dB *and indicated by the matched in phase signals (red and green).*

B Mixing accuracy

Table A1: Measured deviations from the target density of the final and base mixes of LWFC. Refer to Section 4.1.

	Final mix density, ρ [kg/m^3]			Base mix density, ρ_b [kg/m^3]		
Specimen	Target	Casting	Error	Target	Casting	Error
12F-T	1200	1156	44	1881	1899	18
12F-E	1200	1156	44	1881	1899	18
12F-W	1200	1221	21	1881	1880	1
12F-PO	1200	1202	2	1881	1883	2
12F-BE-12	1200	1233	33	1881	1893	12
12F-BE-20	1200	1160	40	1881	1883	2
Average 12F error:			30.7			8.8
14F-T	1400	1415	15	1881	1893	12
14F-E	1400	1361	39	1881	1886	5
14F-W	1400	1389	11	1881	1883	2
14F-PO	1400	1415	15	1881	1893	12
14F-BE-12	1400	1353	47	1881	1894	13
14F-BE-20	1400	1422	22	1881	1896	15
Average 14F error:			24.8			9.8
16F-T	1600	1621	21	1881	1901	20
16F-E	1600	1577	23	1881	1888	7
16F-W	1600	1575	25	1881	1885	4
16F-PO	1600	1621	21	1881	1901	20
16F-BE-12	1600	1633	33	1881	1890	9
16F-BE-20	1600	1610	10	1881	1885	4
Average 16F error:			22.2			10.7
Average total error:			25.9			9.8
Refer to Section 3.2 for specimen notation.						

C Beam-end design drawing

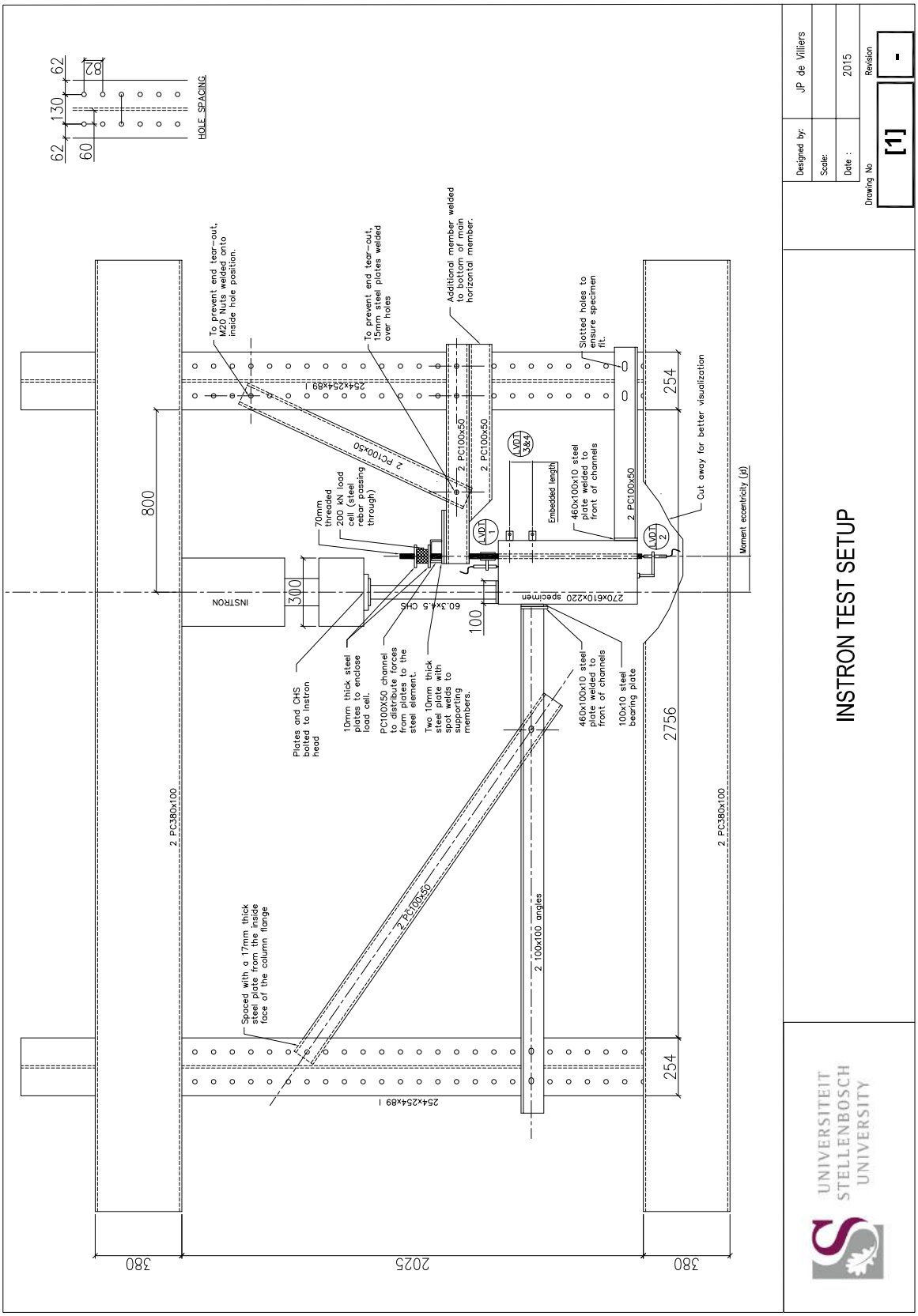

D Pull-out results

Table A2: Listed results obtained from the PO tests on LWFC and NWC. Refer to Section 4.6.

Specimen	Failure mode	Peak Stress [MPa]	Peak free slip [mm]	σ_d [MPa]	σ_a [MPa]	σ_{ad} [MPa]	l_d [mm]	l_d [ϕ]
N-P-10-3	p	20.06	1.26	12.20	6.67			
N-P-10-4	p	18.55	1.24	9.86	1.36	10.66	106	11
N-P-10-5	p	16.38	1.00	9.93	6.39			
N-P-12-3	p	21.92	1.75	10.80	7.73			
N-P-12-4	p	19.64	1.70	7.70	2.69	9.21	147	13
N-P-12-5	p	19.09	1.84	9.13	4.90			
N-P-20-3	s	23.66	0.64	17.22	6.01			
N-P-20-4	s	16.00	0.00	16.00	7.99	15.18	149	8
N-P-20-5	s	12.32	0.00	12.32	12.32			
12F-P-10-3	p	1.19	0.52	1.04	0.96			
12F-P-10-4	p	2.18	0.00	1.78	2.06	1.89	596	60
12F-P-10-5	p	3.44	0.01	2.84	2.87			
12F-P-12-3	p	2.78	1.34	2.00	1.00			
12F-P-12-4	p	1.63	1.77	1.28	1.42	1.59	848	71
12F-P-12-5	p	1.77	1.48	1.50	1.39			
12F-P-20-3	p	2.74	1.87	2.24	1.30			
12F-P-20-4	p	2.66	1.64	2.09	1.97	1.95	1157	58
12F-P-20-5	p	1.89	1.28	1.50	1.30			
14F-P-10-3	p	4.44	0.41	4.28	4.05			
14F-P-10-4	p	5.29	0.21	4.84	3.29	4.34	260	26
14F-P-10-5	p	5.03	0.89	3.89	3.16			
14F-P-12-3	p	5.27	1.89	5.60	2.06			
14F-P-12-4	p	6.21	1.49	2.75	5.22	4.28	316	27
14F-P-12-5	p	5.33	0.92	4.48	4.21			
14F-P-20-3	s	6.59	0.54	5.87	4.57			
14F-P-20-4	s	3.86	0.91	3.78	2.98	4.74	475	24
14F-P-20-5	s	4.57	0.00	4.57	4.57			
16F-P-10-3	s	11.64	0.95	7.39	4.01			
16F-P-10-4	s	9.89	1.17	7.71	6.23	7.26	156	16
16F-P-10-5	s	8.76	0.65	6.67	3.41			
16F-P-12-3	s	9.06	0.58	7.21	6.54			
16F-P-12-4	s	8.64	0.86	5.45	1.39	6.01	225	19
16F-P-12-5	s	7.50	0.55	5.35	3.75			
16F-P-20-3	s	9.33	0.04	9.33	2.99			
16F-P-20-4	s	8.65	0.02	8.65	6.72	8.34	270	14
16F-P-20-5	s	7.04	0.00	7.04	7.04			

For specimen notation refer to Section 3.2.

p - Pull-out failure; s - Splitting failure.

E Modelling errors

Table A3: Errors in design bond force between the actual measured data and the proposed models indicating non-conservative errors (negative errors). Refer to Chapter 6.

	Model (equation (6.4))		
Specimen	T_d [kN]	error [kN]	% of T_d
12F-P-10-3	0.9	-0.42	-47%
12F-P-10-4	2.1	0.29	14%
12F-P-10-5	4.1	1.90	46%
12F-P-12-3	2.5	0.93	37%
12F-P-12-4	2.2	0.02	1%
12F-P-12-5	3.2	0.49	16%
12F-P-20-3	7.1	1.37	19%
12F-P-20-4	8.8	1.19	14%
12F-P-20-5	7.9	-1.63	-21%
14F-P-10-3	3.7	1.16	31%
14F-P-10-4	5.6	2.20	39%
14F-P-10-5	5.6	1.36	24%
14F-P-12-3	7.1	3.80	53%
14F-P-12-4	4.7	0.25	5%
14F-P-12-5	9.5	3.98	42%
14F-P-20-3	18.5	6.27	34%
14F-P-20-4	15.9	-0.41	-3%
14F-P-20-5	24.0	3.63	15%
16F-P-10-3	6.4	1.97	31%
16F-P-10-4	8.9	2.99	33%
16F-P-10-5	9.6	2.23	23%
16F-P-12-3	9.2	3.01	33%
16F-P-12-4	9.2	1.03	11%
16F-P-12-5	11.3	1.08	10%
16F-P-20-3	29.4	5.77	20%
16F-P-20-4	36.3	4.84	13%
16F-P-20-5	37.0	-2.40	-6%